UC Berkeley
UC Berkeley Electronic Theses and Dissertations

Title
Emergent Mechanics of Endocytic Actin Networks

Permalink
https://escholarship.org/uc/item/0ft324kx

Author
Ferrin, Michael Alexander

Publication Date
2023

Peer reviewed|Thesis/dissertation

Emergent Mechanics of Endocytic Actin Networks

By

Michael Alexander Ferrin

A dissertation submitted in partial satisfaction of the

requirements for the degree of

Doctor of Philosophy

in

Molecular and Cell Biology

in the

Graduate Division

of the

University of California, Berkeley

Committee in charge:

Professor David Drubin, Chair
Professor Daniel Fletcher
Professor Matthew Welch
Professor Roberto Zoncu

Summer 2023

Emergent Mechanics of Endocytic Actin Networks
©2023

By
Michael Alexander Ferrin

Abstract

Emergent Mechanics of Endocytic Actin Networks

By

Michael Alexander Ferrin

Doctor of Philosophy in Molecular and Cell Biology

University of California, Berkeley

Professor David Drubin, Chair

Forces generated by actin assembly assist membrane invagination during clathrin-mediated endocytosis (CME). The sequential recruitment of core endocytic proteins and regulatory proteins, and assembly of the actin network, are well documented in live cells and are highly conserved from yeasts to humans. However, understanding of CME protein self-organization, as well as the biochemical and mechanical principles that underlie actin's role in CME, is lacking. Here, I describe two studies revealing potential mechanistic explanations for how actin and associated proteins robustly organize for productive force generation during CME.

I first helped to construct and analyze an experimentally constrained multiscale model showing that a minimal branched actin network is sufficient to internalize endocytic pits against membrane tension. The model predicts that around 200 activated Arp2/3 complexes are required for robust internalization, which was confirmed by experiments in live cells. Simulations reveal that actin self-organizes into a radial branched array with growing ends oriented toward the base of the pit. Long actin filaments bend between attachment sites in the coat and the base of the pit. Elastic energy stored in bent filaments, whose presence was confirmed experimentally, contributes to endocytic internalization. Elevated membrane tension directs more growing filaments toward the base of the pit, increasing actin nucleation and bending for increased force production. Thus, spatially constrained actin filament assembly utilizes an adaptive mechanism enabling endocytosis under varying physical constraints.

I then developed an experimental system and analysis strategies to show that supported lipid bilayers coated with purified yeast Wiskott Aldrich Syndrome Protein (WASP), an endocytic actin assembly regulator, and incubated in cytoplasmic yeast extracts, recruit downstream endocytic proteins and assemble actin networks.

Time-lapse imaging of WASP-coated bilayers reveal sequential recruitment of proteins from different endocytic modules, faithfully replicating in vivo behavior. Reconstituted actin networks assemble in a WASP-dependent manner and deform lipid bilayers, as seen by electron microscopy. Time-lapse imaging reveals that vesicles are released from the lipid bilayers with a burst of actin assembly. Actin networks pushing on membranes have previously been reconstituted; here, we have reconstituted a biologically important variation of these actin networks that self-organize on bilayers and produce pulling forces sufficient to bud off membrane vesicles. I propose that actin-driven vesicle generation may represent an ancient evolutionary precursor to diverse vesicle forming processes adapted for a wide array of cellular environments and applications.

These studies align with the mission of the nascent field of emergent mechanics: to understand new mechanical properties that arise from collective interactions among a system's building blocks. With these results I demonstrate pathways by which the building blocks of actin networks can self-organize into mechanically adaptive, higher-order structures to generate the forces necessary to carry out CME.

Table of Contents

List of Figures

Acknowledgements

First and foremost, I want to thank my parents for lighting my path toward a life of science by encouraging my curiosity and eradicating any obstacles to my ability to fully focus on my education throughout my development. Recognizing this rare privilege inspires me to become a force for expanding the social and economic conditions that the freedom to pursue one's interests to as many people as possible.

I want to thank my undergraduate research mentors Seemay Chou and Joseph Mougous for transforming my vague interest in science to a concrete set of skills and principles for effective knowledge generation.

I want to thank my technician research mentor Rasi Subramaniam for revolutionizing my conception of research by introducing me to physical biology. My experience using this approach in his lab has served as my personal gold standard for research ever since.

I want to thank my advisor David Drubin for providing the nurturing environment to freely explore my changing interests throughout my PhD. I deeply appreciate his trust in all his trainees to always push the scope of the lab's research focus and bring in new ideas.

I want to thank my scientific collaborators for the wide range of training I have received during my thesis research. Matt Akamatsu was a brilliant rotation mentor with whom I still collaborate today on integrating theory and experiment to study the cytoskeleton. Ross Pedersen's myosin expertise also continues to serve an essential role in my theoretical model construction. Emily Stoops performed all the tedious work to get our reconstitution system up and running, while Danielle Jorgens stayed involved throughout our project to iterate on electron microscopy conditions for years until we had usable data. Tyler Harmon and Frank Jülicher gave me a chance after our short rotation together at the Woods Hole Physical Biology of the Cell course in 2018 to build a new model of endocytosis from scratch and hire me to complete the project following my PhD.

I have had the delight of mentoring two undergraduate students, Dahlia Deng and Nikhil Kulkarni, as well as three rotations students, Sam Smith, Kahmina Ford, and Vinu Harihar, during my time in the Drubin lab. I want to thank them all for their eagerness to learn my favorite techniques and shape the direction of our projects with their interests as well.

I want to thank the entire Barnes/Drubin lab for cultivating the best lab culture for scientific growth. The atmosphere of collaboration and openness to learning new things gave me the foundation to feel comfortable exchanging questions and asking for help with anything, no matter how seemingly naive.

I want to thank my bandmates in Close Friends and the bay area music community for giving me a creative outlet and sense of pride, especially when science was not going my way.

Chapter One
General Introduction

1.1 Self-organization and emergent mechanics

The initial spark of curiosity that would eventually guide me toward pursuing a doctorate in Molecular and Cell Biology came from the realization that, as concisely stated by Theodosius Dobzhansky half a century ago, "Nothing in Biology Makes Sense Except in the Light of Evolution" (Dobzhansky, 1973). One needs not invoke the conceptual framework of "design" to understand how living things function, but rather these apparent functions can be understood as the consequence of spontaneous interactions between selective forces from the natural environment and genetic heritability. This assertion that all behavior, order, and diversity of life can be explained by natural laws has been my underlying motivation to study the physical basis of biological functions. Upon following this interest down to the cellular and molecular level, I would like to append my own bold statement: Nothing in cell biology makes sense except in the light of self-organization.

Self-organization describes "the emergence of an overall order in time and space of a given system that results from the collective interactions of its individual components" (Wedlich-Söldner and Betz, 2018). One can find numerous well-studied self-organizing model systems at all scales of nature. The social organization of ant colonies, construction of termite mounds, formation of animal pigmentation patterns, and assembly of the mitotic spindle are among the most famous examples in which complex biological architecture emerges in the absence of a centralized architect (Kirschner, Gerhart and Mitchison, 2000; Karsenti, 2008; Wedlich-Söldner and Betz, 2018). Importantly, self-organization differs from self-assembly, a related conceptual framework that is also frequently invoked to explain the spontaneous construction of complex architecture on the molecular level. Whereas a structure is self-assembling if it is the equilibrium state of its components sampling interactions with each other until reaching their global free energy minimum, a self-organizing structure can be a far-from-equilibrium steady state requiring continuous flux of energy and matter, as in living systems (Nicholson, 2019). Of course, the two are not mutually exclusive; a self-organizing system can comprise self-assembling components.

Among the vast array of apparent functions of self-organized living structures, many are mechanical in nature. Again at all scales of biology, physical bodies must exchange mechanical forces with their environment to move through space, or resist movement, in order to carry out the essential mechanisms of life. Because the study of classical mechanics comes from describing static structures in the human-engineered world, this framework is ill-equipped to explain the mechanics of dynamic, self-organizing biological structures. For this reason, there has been a call to develop a new framework, "emergent mechanics," to properly study this mechanical complexity

(Dumont and Prakash, 2014). This new approach calls for building theoretical models that integrate properties of a system's components across many length and time scales in order to map the contributions of each component to the higher-order structure's emergent properties. At the same time, there must be experimental complements to constrain assumptions and test predictions arising from these modeling efforts whenever possible. In my thesis research, I aimed to apply the framework of emergent mechanics toward understanding mechanisms of adaptive anisotropic force production by the actin network in clathrin-mediated endocytosis.

1.2 Actin mechanics

As a system of molecular building blocks that can assemble into complex higher-order mechanically active structures, the eukaryotic actin cytoskeleton is rich for studying emergent mechanics. Actin networks can collectively generate forces to drive a variety of intracellular motion and shape changes. The most striking examples include assembly and disassembly-powered crawling motility of entire cells on a surface (Pollard and Borisy, 2003), as well as ability of some infectious bacteria to enter a host cell's cytoplasm and hijack its actin-regulating proteins to propel themselves into neighboring cells (Stevens, Galyov and Stevens, 2006). And to be further elaborated upon later, actin-based force generation can be critical for clathrin-mediated endocytosis.

Starting from first principles, the minimal force-generating actin network can be a single filament made up of individual actin monomers polymerized head-to-tail in a double helix structure (Pollard and Borisy, 2003). If one end of the filament is positioned orthogonal to a solid object and the other end is physically anchored in place, elongation of the filament by polymerization of additional monomers to the first end can generate a force on that object via a mechanism called an elastic Brownian ratchet (Mogilner and Oster, 1996; Pollard, 2016b). To briefly explain the mechanism: even when pressed against a surface, constant thermal bending fluctuations (Brownian motion) of the filament and/or the object being moved occur on a length scale large enough to allow additional actin monomers to diffuse into the transient space between the filament and the other object. Once the monomer binds and becomes the new end of the filament, the filament converts the energy stored by its bent state into a force against the object in order to relax into a straight state. As this cycle repeats, the actin acts as a polymerization-based motor to move the object over time.

In cells, numerous accessory proteins can interact with actin monomers and filaments to impart emergent mechanical properties to the higher-order network. The activities of these proteins include catalyzing the nucleation of new filaments from monomers, nucleating new "daughter" filaments branching off the side of "mother" filaments, increasing the rate of filament elongation, capping the ends of filaments to prevent further elongation, cross-linking filaments together, and severing filaments (Figure 1.1A) (Pollard, 2016a). All these activities come together in the "dendritic

nucleation model" of actin-based motility (Figure 1.1B) (Pollard, Blanchoin and Mullins, 2001; Pollard and Borisy, 2003). The continuous filament nucleation, elongation, and recycling collectively produce a self-organizing dynamic structure that maintains mechanical force against a membrane. Approaching this system from an emergent mechanics perspective has revealed that it not only self-organizes to generate force, but it also has the capacity to adapt to perturbations in resistive load through self-reorganization (Bieling *et al.*, 2016; Mueller *et al.*, 2017; Garner and Theriot, 2022; Li *et al.*, 2022).
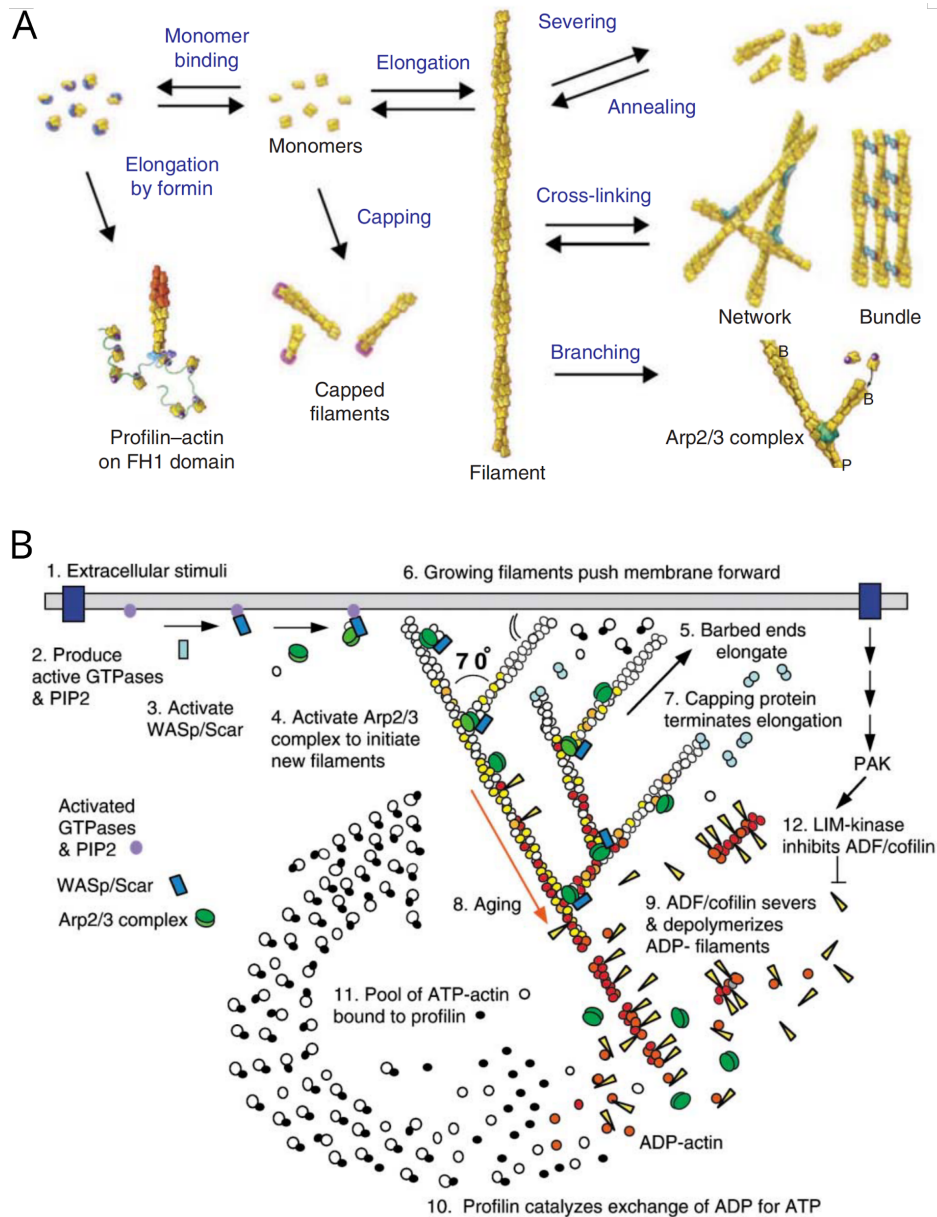
Figure 1.1 Emergent force-generating architecture arises from collective interactions among actin and accessory proteins. (A) Summary of individual actin behaviors mediated by interactions between actin and actin-binding proteins. Figure adapted from (Pollard, 2016a). (B) Schematic diagram of the dendritic actin nucleation model in the context of cell motility. Figure adapted from (Pollard and Borisy, 2003).

1.3 Clathrin-mediated endocytosis mechanics

Clathrin-mediated endocytosis (CME) is an especially attractive process for studies of actin emergent mechanics due to the relatively complete parts list and available quantitative information about the positions, recruitment timing and biochemical function of many of the participating proteins (Kaksonen, Sun and Drubin, 2003; Kaksonen, Toret and Drubin, 2005; Taylor, Perrais and Merrifield, 2011; Idrissi *et al.*, 2012; Picco *et al.*, 2015; Sochacki *et al.*, 2017; Arasada *et al.*, 2018; Mund *et al.*, 2018).

CME is a ubiquitous and essential cellular process by which eukaryotic cells take macromolecules from the extracellular space and the plasma membrane into the cell interior (Kaksonen and Roux, 2018). During CME, the plasma membrane is bent, pinched, and pulled inward in a time frame of ~60 s thereby transitioning from a flat sheet into a spherical vesicle ~100 nm in diameter. Clathrin and its adaptor proteins establish a coat that generates initial membrane curvature (Pearse, 1976; Chen *et al.*, 1998; Stachowiak *et al.*, 2012), and BAR (bin-amphiphysin-rvs)-domain proteins bind curved membranes and support further membrane curvature (David *et al.*, 1996; Kishimoto *et al.*, 2011; Buser and Drubin, 2013). During yeast endocytosis, branched actin filaments provide the force required for membrane tubule formation (Engqvist-Goldstein and Drubin, 2003; Sun, Martin and Drubin, 2006; Idrissi *et al.*, 2012; Kukulski *et al.*, 2012; Wang and Carlsson, 2017; Picco *et al.*, 2018). In metazoan cells, endocytic pits under high tension stall at a 'U'-shaped intermediate in the absence of functional actin (Boulant *et al.*, 2011), implying that actin is required to generate plasma membrane shape changes late in CME (Yarar, Waterman-Storer and Schmid, 2004; Hassinger *et al.*, 2017; Yoshida *et al.*, 2018). The molecular mechanism by which a network of polarized, branched actin filaments assembles at these sites for robust force generation is poorly understood.

In my thesis research I investigated the self-organizing capacity of endocytic actin networks using a combination of theoretical and experimental reconstitution techniques. In chapter two, my collaborators and I constructed a minimal model to demonstrate how a simple template of actin linkers and nucleators can reproducibly give rise to a naturally adaptive actin network for efficient endocytic force generation. In chapter three, my collaborators and I developed a biochemical reconstitution of endocytic actin networks to reinforce experimentally that assembly of actin nucleators on a membrane is sufficient to initiate actin networks that are competent to pull membrane patches into vesicles. I view these results fitting into a larger effort to understand the emergent mechanics of actin networks in CME. As the field maps out the contribution of each individual protein toward the collective higher-order structure and function, I hope that arriving at such a detailed understanding sheds light on how sophisticated cellular behaviors like CME evolved from simpler mechanisms.

Chapter Two

Principles of self-organization and load adaptation by the actin cytoskeleton during clathrin-mediated endocytosis

This chapter contains material published in the reference (Akamatsu *et al.*, 2020) in collaboration with co-authors Matthew Akamatsu, Ritvik Vasan, Daniel Serwas, Padmini Rangamani, and David Drubin.

2.1 Introduction

Cells polymerize actin filaments to produce force and provide mechanical integrity for a variety of cellular processes, from cytokinesis and cell migration, to membrane reshaping and trafficking (Pollard, 2016a). For each cellular process, actin filaments organize into a specific geometry that confers structural integrity and force-generation capacity. Most membrane deformation processes use branched actin networks nucleated by the Arp2/3 complex, a branched actin filament network nucleator (Rotty, Wu and Bear, 2013; Carlsson, 2018). On a large (mm) length scale, branched actin networks drive the plasma membrane forward during cell migration, such that on the scale of individual actin branches, the membrane shape can be thought of as more or less constant (Schaus, Taylor and Borisy, 2007; Keren *et al.*, 2008; Mueller *et al.*, 2017). However, on a smaller (sub-micron) length scale, branched actin networks deform many cellular membranes as part of organelle and vesicle biogenesis and function (Rottner *et al.*, 2017). The relationship between cellular membrane curvature and local actin assembly for each of these 'local' membrane-deformation processes remains relatively unexplored (Daste *et al.*, 2017).

Actin network assembly is known to play a key role in membrane shape change in some contexts. For example, mathematical modeling (Liu *et al.*, 2009; Berro *et al.*, 2010; Carlsson and Bayly, 2014; Dmitrieff and Nédélec, 2015; Wang *et al.*, 2016; Mund *et al.*, 2018) and quantitative fluorescence imaging in yeast (Wu and Pollard, 2005; Berro *et al.*, 2010; Berro and Pollard, 2014; Picco *et al.*, 2015) have established the relationship between actin filament assembly and plasma membrane shape particular to fungi, which have unique mechanical requirements due to very high (~10 atm) hydrostatic turgor pressure. However, less is known about actin organization and function in the lower force regime characteristic of metazoan cells. A multiscale modeling effort that accounts for the mechanics of single actin filaments and that is constrained by experimental measurements of actin dynamics, spatial organization of the filaments, and tension in the plasma membrane is required to gain insight into actin organization and force generation capacity. We hypothesize that in localized membrane-reshaping processes such as endocytosis, branched actin networks assemble under specific spatial 'boundary conditions,' which serve as geometrical constraints dictated both by the shape of the membrane and the spatial segregation of

membrane-associated proteins that interact with actin. These unique spatial boundary conditions on a curved surface, combined with the knowledge of numbers of molecules in cells and known reaction rate constants, provide the necessary information for multiscale modeling and a mechanistic framework to understand the relationship between plasma membrane mechanics and branched actin assembly and mechanics associated with CME.

Using this framework, we sought to answer the following questions: How do branched actin networks assemble, organize, and produce force around an endocytic pit? How does the spatial segregation of Arp2/3 complex activators (Almeida-Souza *et al.*, 2018; Mund *et al.*, 2018) and actin binding proteins associated with endocytic coats (Engqvist-Goldstein *et al.*, 2001; Sochacki *et al.*, 2017; Clarke and Royle, 2018) influence this organization? And finally, how do endocytic actin networks adapt to changing loads due to the stochastic environment and changes in membrane tension? To answer these questions, we employed experimentally-constrained multiscale modeling of plasma membrane mechanics and actin filament dynamics. Our results show that a minimal branched actin network is sufficient to create sustained internalization of an endocytic pit against physiological membrane tension. Actin filament self-organization and bending, which arise from the spatial distribution of actin-coat attachments around the curved endocytic pit, allow the actin network to adapt to changing loads. We anticipate that the mechanistic insights gained for actin in mammalian endocytosis will also apply to a variety of local membrane-bending processes carried out by branched actin throughout the cell.

2.2 Results and discussion

2.2.1 Multiscale modeling shows that a minimal branched actin network is sufficient to internalize endocytic pits against physiological membrane tension

We combined a continuum-mechanics model of the plasma membrane, an agent-based model of actin filament dynamics, and experimental measurements to determine the molecular mechanism by which branched actin networks produce force during mammalian clathrin-mediated endocytosis (Figure 2.1).
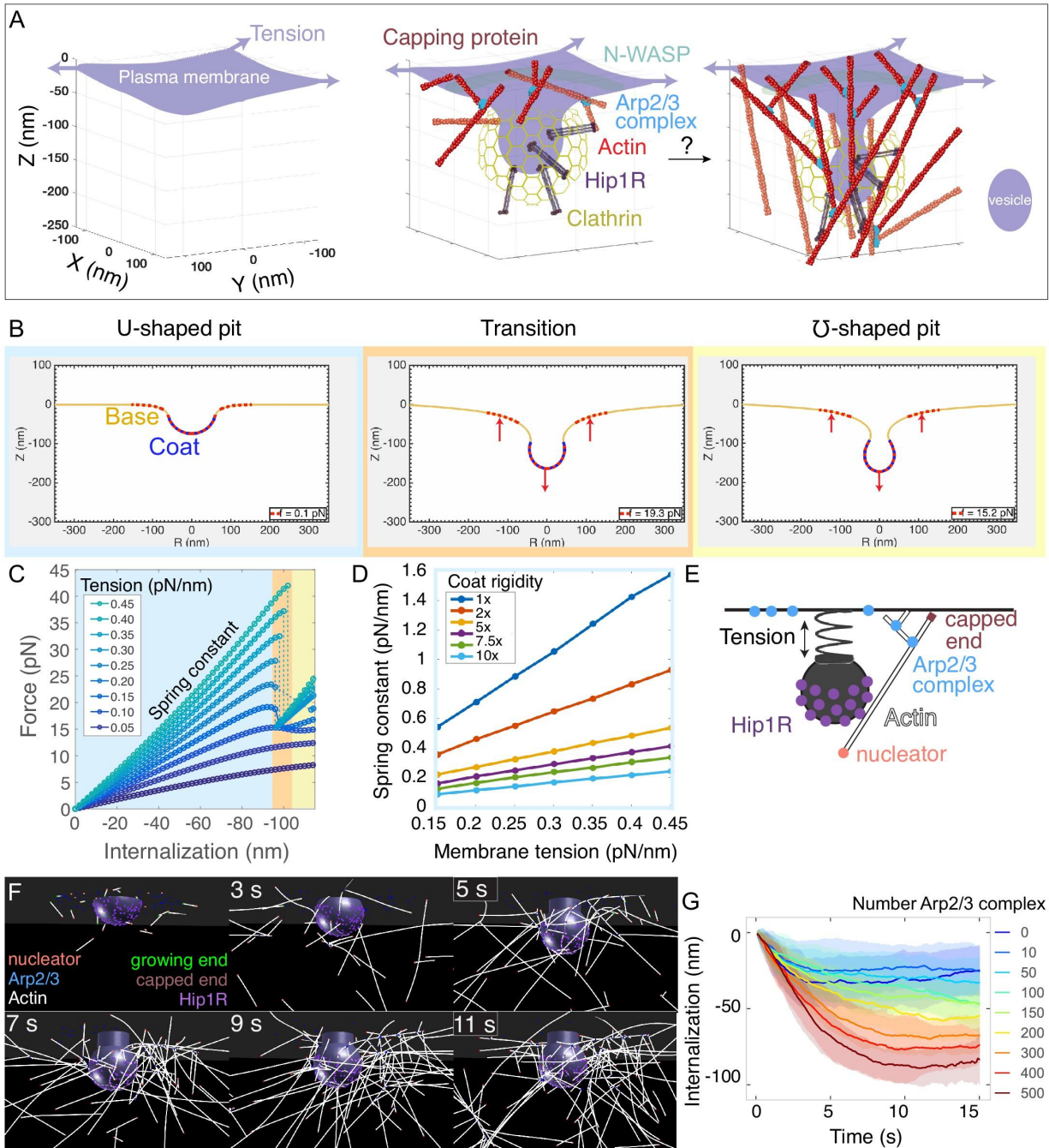
Figure 2.1 Multiscale modeling shows that a minimal branched actin network is sufficient to internalize endocytic pits against physiological membrane tension. (A) Schematic of a section of the cell's plasma membrane being internalized during mammalian endocytosis depicts plasma membrane deformation against membrane tension (purple arrows) countered by the clathrin coat (yellow) and the actin cytoskeleton (red). (B) Shape of the membrane and pit internalization from continuum mechanics simulations of the endocytic pit experiencing axial (Z) forces corresponding to simplified actin forces. To begin with, the plasma membrane (yellow) is deformed by a coat with preferred curvature that expands in area until the pit stalls. A net force (red arrows) is applied downward from the coat and upward into the base of the endocytic pit (red dotted lines). In this simulation, membrane tension was 0.2 pN/nm, and the coated area was rigid (2400 pN·nm). (C) Force versus pit internalization relationships for different values of membrane tension. Internalization is defined as the pit displacement in Z. Shading delineates linear force-internalization regime (blue); 'transition point' from U to omega shape (orange);

'omega-shaped' regime where the neck is narrower than the pit diameter and the force required for internalization is lower than at the transition point (for tensions > 0.1 pN/nm) (yellow). Color matches the three snapshots in B. Parameters are given in Supplementary files 1 and 2. (D) Resistance of pit to internalization versus membrane tension. Resistance (spring constant) is defined as absolute value of slope in C for the 'U-shaped' region. Each curve is calculated for a different value of membrane rigidity (where 1x = 320 pN·nm, the rigidity of the uncoated plasma membrane). (E) Computational model of branched actin filament polymerization coupled to endocytic pit internalization. An internalizing endocytic pit is modeled as a sphere with a neck attached to a flat surface by a spring. Active Arp2/3 complex (blue) is distributed in a ring around the base of the pit. An actin nucleation protein (pink) generates an actin filament (white), which polymerizes, stalls under load, and is stochastically capped (red). Arp2/3 complexes bind to the sides of actin filaments and nucleate new filaments at a 77-degree angle, creating new branches. Linker Hip1R (purple) is embedded in the pit and binds to actin filaments. Model parameters are given in Supplementary file 3. (F) Graphical output of the simulations from Cytosim (Nedelec and Foethke, 2007) at 2 s intervals. Scale bar: 100 nm. (G) Pit internalization over simulated time as a function of the number of available molecules of Arp2/3 complex. Average of 16 simulations per condition. Shaded bars are standard deviations.

First, my collaborators used a continuum-mechanics model of the plasma membrane (Rangamani, Mandadap and Oster, 2014; Hassinger *et al.*, 2017; Alimohamadi *et al.*, 2018) to determine the force-extension relationship for clathrin-coated pits stalled at a U-shaped intermediate under high membrane tension (Figure 2.1B). Here, the extension refers to the extent of pit internalization, which is a displacement in the -Z direction (Figure 2.1A–B). Simulations demonstrated that a clathrin-coated pit experiences a nearly linear force-extension relationship until an internalization of ~100 nm, at which point the pit can also adopt a pinched (or 'omega') shape, which requires a lower force (Figure 2.1C). They found that the resistance to internalization is directly proportional to plasma membrane tension for a wide range of coat rigidities (Figure 2.1D). Importantly, this direct scaling between resistance to internalization and membrane tension allowed us to treat this step of endocytic pit internalization as a linear spring, with the spring constant calibrated using measurements of plasma membrane tension in mammalian cells (Diz-Muñoz *et al.*, 2016; Kaplan *et al.*, 2022).

The simple spring-like relationship uncovered above between force and endocytic pit internalization (Figure 2.1D) allowed us to simplify our mechanical treatment of the plasma membrane while modeling individual actin filaments and actin-binding proteins with realistic kinetics and mechanics (Figure 2.1E-G). We used Cytosim (Nedelec and Foethke, 2007) to construct a filament-based model of the endocytic actin network. This agent-based model allowed us to simulate the emergent architecture and mechanical functions of branched actin for realistic endocytic geometries.

We simplified the endocytic pit as a solid, impermeable structure, initially a hemisphere, attached to a flat plasma membrane corresponding to the 'U-shaped' intermediate (Figure 2.1E) (Yarar, Waterman-Storer and Schmid, 2004; Boulant *et al.*, 2011; Messa *et al.*, 2014; Avinoam *et al.*, 2015). The following rules were prescribed for actin filament dynamics. Initially, actin filament-nucleating proteins seed a small number of actin filaments near the endocytic pit. These randomly-oriented 'mother filaments' serve as templates for binding pre-activated Arp2/3 complexes, which correspond to the coincidence of Arp2/3 complex and its activator N-WASP, arranged

in a ring (Almeida-Souza *et al.*, 2018; Mund *et al.*, 2018) at the base of the endocytic pit (Kaksonen, Sun and Drubin, 2003; Idrissi *et al.*, 2008; Picco *et al.*, 2015; Kaplan *et al.*, 2022). When an active Arp2/3 complex comes in proximity with an actin filament, it can bind to the filament and nucleate the growth of a new branched filament at an ~77 ° angle (Blanchoin *et al.*, 2000). Growing actin filaments can polymerize, diffuse under thermal fluctuations, and bend under force, and their growing ends are capped stochastically. Filament growth decreases with load according to the Brownian ratchet mechanism (Peskin, Odell and Oster, 1993; Mogilner and Oster, 1996). Growth of the actin network is coupled to internalization of the endocytic pit by an actin-linking protein (Hip1/Hip1R/Epsin, simplified here as Hip1R), which is embedded in the coated pit and binds to actin filaments (Engqvist-Goldstein *et al.*, 1999, 2001; Sochacki *et al.*, 2017; Clarke and Royle, 2018). Importantly, most of the parameters in this model have been determined with measurements in vitro or in vivo, including the dimensions of the endocytic pit, its resistance to internalization (modeled as a spring, Figure 2.1D), rates of association and dissociation of different proteins, branching angles, capping rates, filament persistence length, and stall force (Materials and methods).
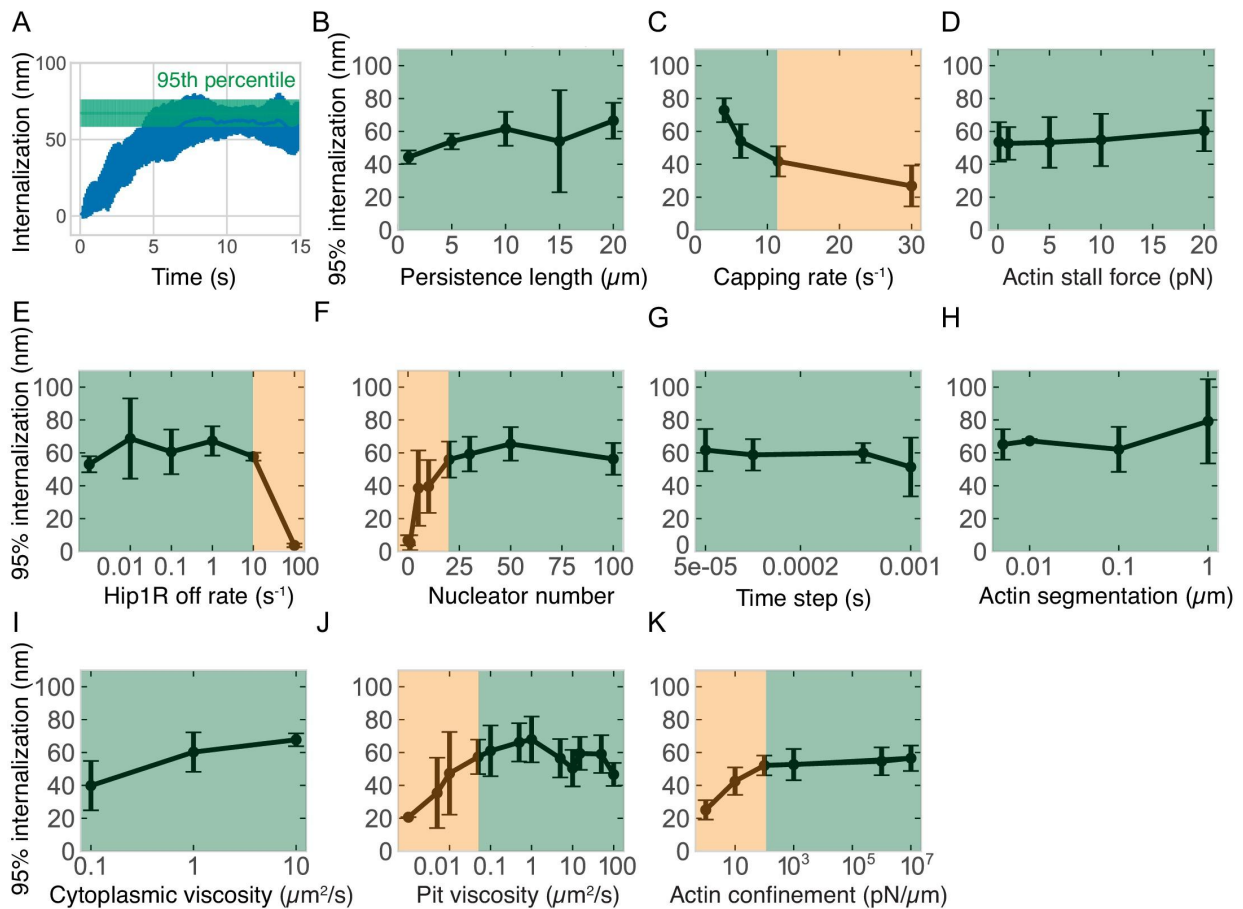
Figure 2.2 Effect of different actin- and simulation-related parameters on pit internalization dynamics. (A) Graph illustrating the definition of the metric of 95% internalization -- the 95th percentile of internalization. This metric is used in the remaining panels and throughout the study to compare the effectiveness of endocytosis under

different parameter combinations. The first 12 s of simulation are used to control for sampling errors near the end of the simulation. (B) Internalization versus actin persistence length (filament stiffness) (n = 60 simulations). (C) Internalization versus capping rate (n = 45). Lower capping rate increases the total amount of actin. (D–F) Internalization versus: (D) actin polymerization stall force (n = 70); (E) Hip1R off rate (n = 24); (F) number of linear actin filament nucleating proteins (n = 84). (G–K) Controls for simulation conditions. Internalization versus: (G) simulation time step (n = 42); (H) actin segmentation (distance between model points in each filament) (n = 8); (I) cytoplasmic viscosity (n = 18); (J) axial (Z) viscosity of pit (n = 111); (K) strength of actin confinement inside the cell (restorative force against actin filaments located outside the cell) (n = 96). Green regions highlight the parameter space for which internalization is relatively insensitive to the parameter value; orange regions highlight parameter space more strongly dependent on parameter value. Bars are standard deviations.

Stochastic simulations of the model showed that this minimal branched actin network internalizes endocytic pits up to ~60 nm against physiological membrane tension (Figure 2.1F). In order to compare different conditions, we used two metrics – internalization of the pit (in nm) over time (Figure 2.1G) and the 95th percentile of internalization (Figure 2.2A). Then, we evaluated the robustness of the model to different parameters by conducting a series of parameter sweeps (Figure 2.2). We found that the extent of internalization is robust to a wide range of parameters, including filament stiffness, stall force, and affinity between Hip1R attachments and actin filaments (Figure 2.2). The extent of internalization was particularly sensitive to the number of available Arp2/3 complexes (Figure 2.1G), indicating a need for precise measurements of this molecule at mammalian endocytic sites. This motivated my collaborators to experimentally count the number of Arp2/3 complexes at CME sites *in vivo* (Akamatsu *et al.*, 2020).

2.2.2 Self-organization of actin filaments into a radial dendritic network drives endocytic internalization

Incorporating the Arp2/3 molecule number my collaborators determined experimentally into our multiscale model, we next conducted simulations of the model to investigate the spatial organization of actin and force generation capacity of the endocytic network (Figure 2.3). Strikingly, the actin network self-organized around the endocytic pit. This self-organized network drove the assembly of 150 ± 30 actin filaments (Figure 2.4A) containing 5700 ± 1100 monomers (Figure 2.4B). Interestingly, only a small number of actin filaments (<5) grew at any given time because the filaments became capped soon after they were nucleated (Figure 2.4C) (Berro *et al.*, 2010; Xiong *et al.*, 2010; Rangamani *et al.*, 2011). Filament lengths were exponentially distributed with a final length of 90 ± 80 nm (Figure 2.4D-E). Actin filaments bound to 120 ± 10 Hip1R molecules in the coat (Figure 2.4F). The endocytic pit internalized ~60 nm in 10–15 s (Figure 2.3A and D). Based on the initial geometry of the endocytic pit and activated Arp2/3 complex, branched actin filaments self-organized into a radial dendritic network: the network attached to the clathrin coat by binding to Hip1R, the pointed (minus) ends localized close to the pit and the barbed (plus) ends near the base of the pit were oriented to grow toward the base of the pit (Figure 2.3A–C).
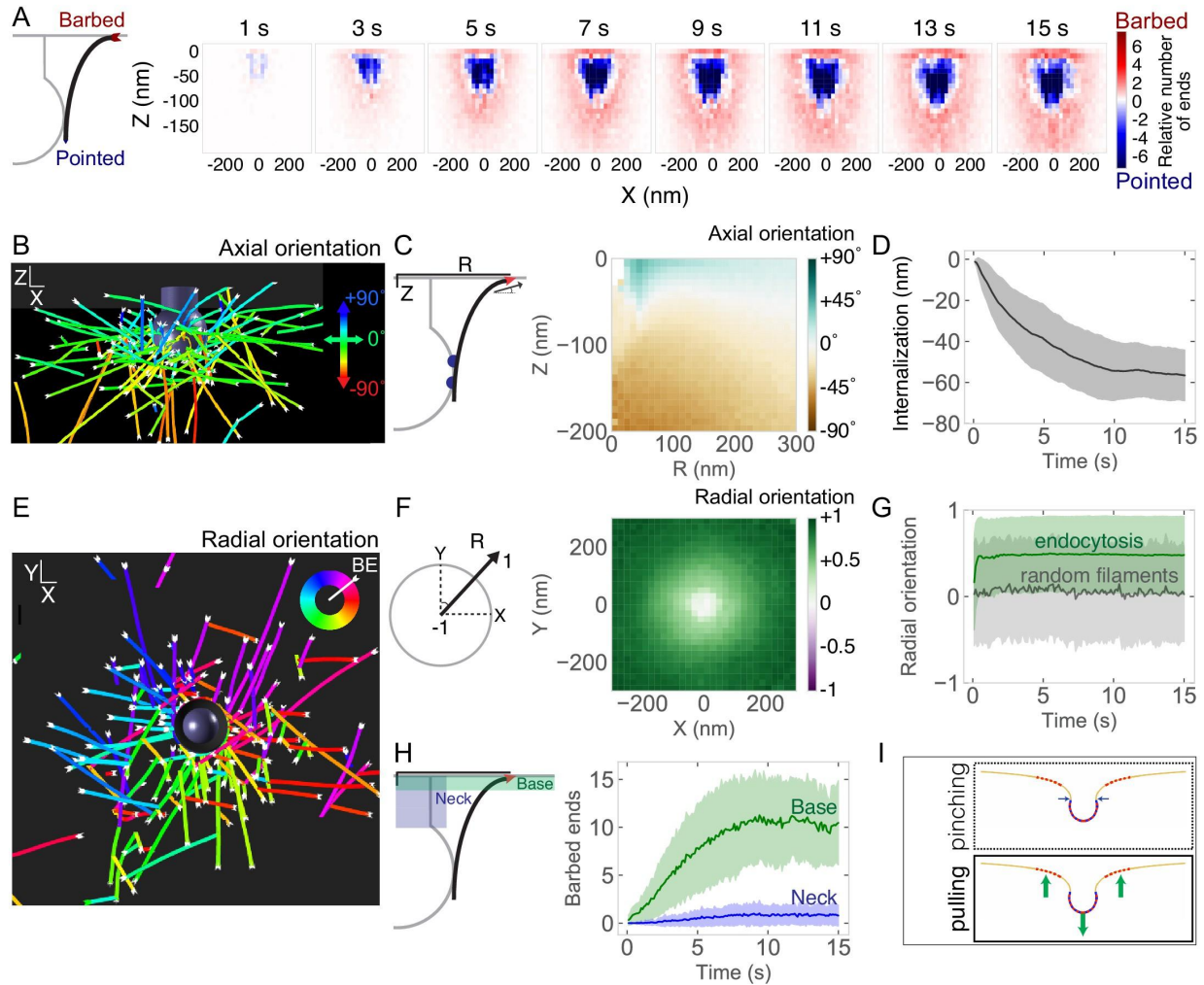
Figure 2.3 Self-organization of actin filaments into a radial dendritic network drives endocytic internalization. (A) (Left) Schematic depicting actin barbed (plus) or pointed (minus) ends. (Right) Heat maps of the positions of barbed ends (red) or pointed ends (blue) relative to the endocytic pit. Color code represents the relative number of ends. Each graph is averaged across 96 simulations and 1 s of simulation time. (B) Simulation output of endocytic actin filaments color-coded for axial (Z) orientation. Blue filaments orient toward the base of the pit (+90°) and green filaments orient parallel to the base of the pit (0°). (C) Axial orientation of barbed ends. (Left) Schematic of axes. R is radial position of barbed end. (Right) Heat map of axial orientation of barbed ends as a function of R and Z position. Average of 96 simulations. (D) Pit internalization over time (n = 96 simulations). (E) Simulation output of endocytic actin filaments color-coded for radial orientation. (F) Radially oriented endocytic actin filaments. (Left) Schematic of axes. Radial orientation is defined such that +1 = barbed end oriented away from the center of the pit, and –1 = barbed end oriented toward the center of the pit. (Right) Heat map of radial orientation of barbed ends as a function of X and Y position (n = 96 simulations). Barbed ends radiate outward. (G) Radial orientation of barbed ends over time for 96 simulations. Gray curve is negative control of randomly oriented filaments (n = 50 filaments in one simulation). (H) Concentration of barbed ends near the base of the endocytic pit. (Left) Schematic of positions of the neck and base of the pit. (Right) Number of barbed ends near base (green) or neck (blue) of pit, defined as within 7.5 nm of each surface. (I) The majority of forces are directed orthogonal to the base of the pit based on positions of barbed ends in simulations. Shaded bars are standard deviations.

The axial self-organization of this branched actin network resembles that at the leading edge of cells (Figure 2.4G–I) (Svitkina and Borisy, 1999; Maly and Borisy, 2001; Schaus, Taylor and Borisy, 2007; Mueller *et al.*, 2017), with an important difference.

Because actin filament attachment sites are located on the coat of the endocytic pit, filaments radiate away from the center of the pit, such that most of the barbed ends orient radially away from the center of the pit rather than toward the coat or neck (Figure 2.3E). The radial orientation of barbed ends gradually increases from the center of the pit, where there is no preferred orientation, to the periphery, where the barbed end radial orientation is highest (Figure 2.3F). The extent of radial distribution of the filaments increases rapidly after time 0 (Figure 2.3G). An important consequence of this self-organization is that, based on the position of Hip1R and the Arp2/3 complex, more barbed filament ends localize near the base (10 ± 4 ends) than near the neck of the endocytic pit (1 ± 1 ends) (Figure 2.3H). These data result in an important prediction from our model: an actin network self-organized as described here will produce an axial force during pit internalization (Figure 2.3I). We predict that the radial dendritic self-organization is a powerful mechanism that makes endocytic actin networks resilient to biochemical and mechanical perturbations.
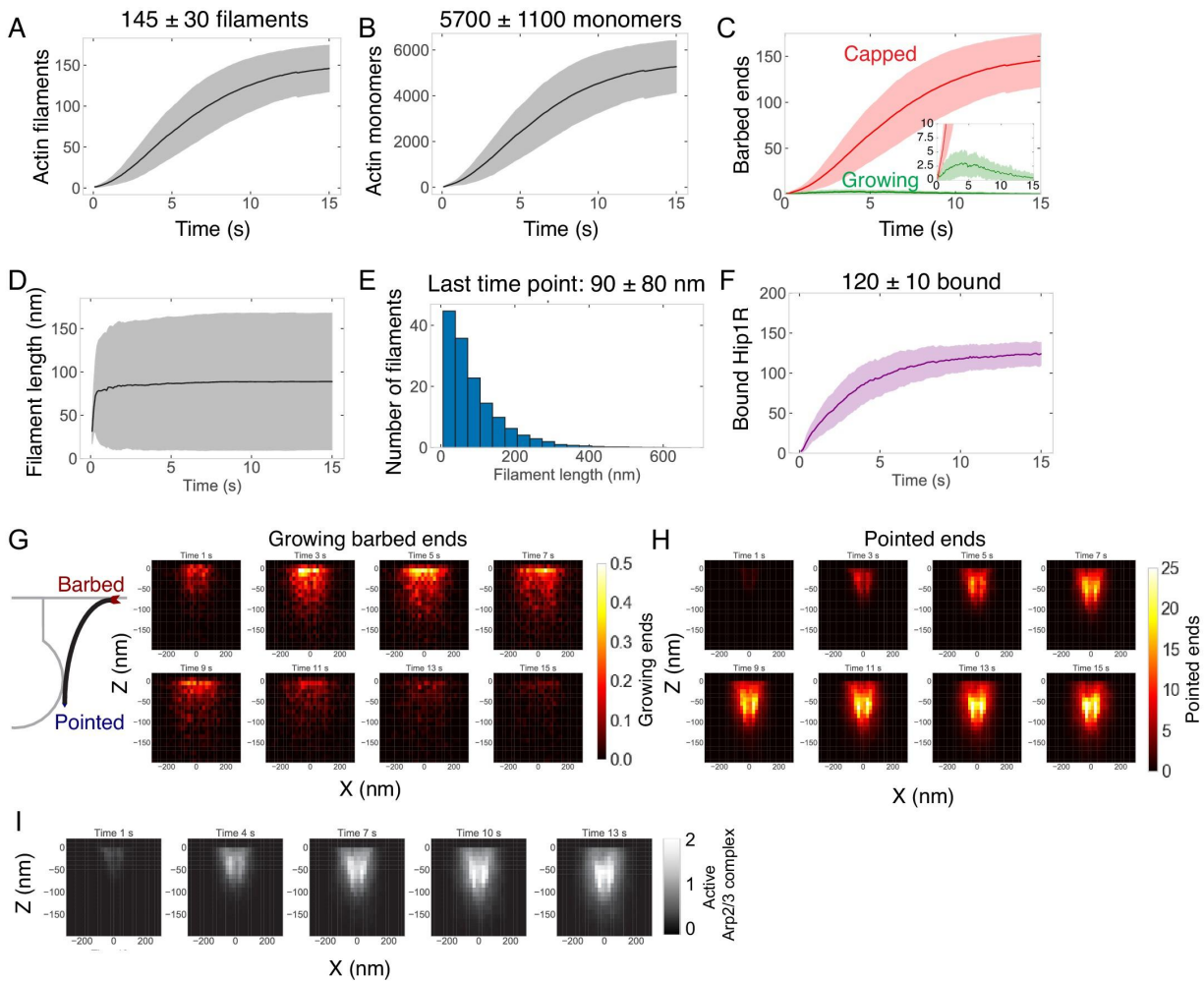
Figure 2.4 Assembly and self-organization of endocytic actin network. (A–F) Quantification of the endocytic actin network over time. n = 96 simulations. Measurements are of filaments bound directly to Hip1R or indirectly to Hip1R through the Arp2/3 complex. Shaded bars are standard deviations. (A) Number of actin filaments. (B) Number

of actin monomers. (C) Numbers of growing (green) or capped (red) barbed ends. (D) Lengths of filaments. (E) Distribution of filament lengths at last time point. n = 14,007 filaments from 96 simulations. (F) Number of bound Hip1R. (G) (Left) Schematic of actin filament barbed and pointed ends. (Right) Heat map of the positions of growing barbed ends in X and Z over time. (H) Heat map of position of pointed (minus) ends in X and Z over time. (I) Heat map of position of active Arp2/3 complex in X and Z over time.

2.2.2 Spatial distribution of actin/coat attachments and Arp2/3 complex, but not Arp2/3 complex density, strongly affects actin self-organization and pit internalization

Our finding that self-organized endocytic actin networks grow toward the base of the pit prompted us to explore the molecular mechanism by which actin filaments self-organize. Actin dynamics in association with the endocytic machinery can be thought of as a polymerization engine constrained by two spatial boundary conditions – active Arp2/3 complex at the base of the pit (Kaksonen, Sun and Drubin, 2003; Idrissi *et al.*, 2008; Picco *et al.*, 2015; Almeida-Souza *et al.*, 2018; Mund *et al.*, 2018; Kaplan *et al.*, 2022) and Hip1R/actin attachments on the curved pit surface (Figure 2.5A) (Engqvist-Goldstein *et al.*, 1999, 2001; Sochacki *et al.*, 2017; Clarke and Royle, 2018). Given that such spatial boundary conditions confer unique mechanical properties and adaptation to loads under flat geometries in vitro (Bieling *et al.*, 2016), we aimed to understand how the boundary conditions corresponding to the curved endocytic pit affect endocytic actin organization and internalization. We tested two different scenarios: varying the surface density of Arp2/3 complex at the base of the pit and varying Hip1R surface coverage around the pit itself.
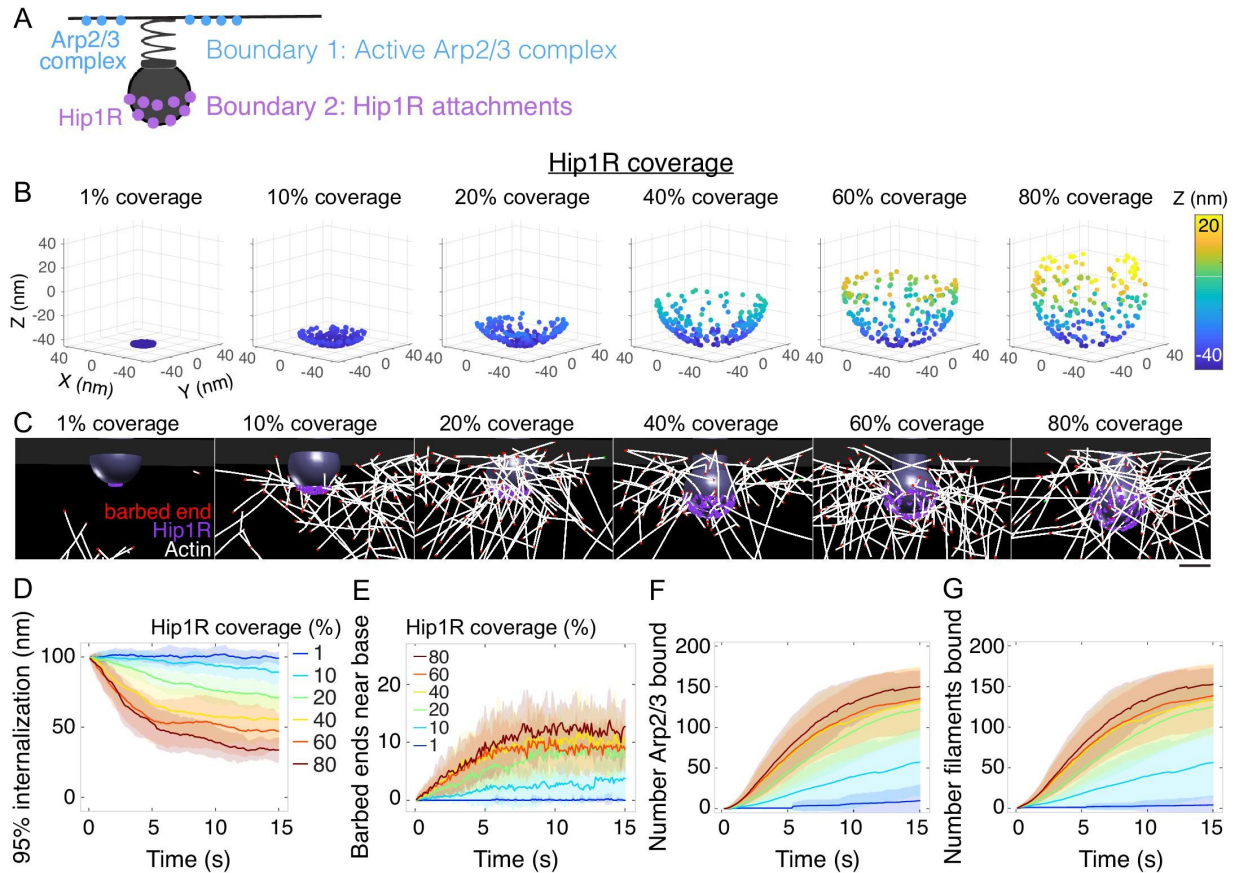
Figure 2.5 Spatial distribution of actin/Hip1R attachments strongly affects actin self-organization and pit internalization. (A) Schematic of spatial boundary conditions from endocytic actin-binding proteins. Positions of active Arp2/3 complex (blue) and actin/pit attachments via linker proteins such as Hip1R (purple). (B) Initial positions of Hip1R around increasingly large pit surface area, from 1% to 80% of a sphere. The top ~20% of the sphere is occluded by the neck. (C) Snapshots of a series of simulations for different values of Hip1R coverage showing actin distribution at t = 13 s. (D–G) Changes in the endocytic actin network over time as a function of Hip1R coverage (colors). n = 96 simulations. (D) Internalization; (E) Number of barbed ends near the base of the pit (within 7.5 nm); (F) Number of Arp2/3 complexes bound in the endocytic network; (G) Number of actin filaments bound in the endocytic network. Scale bar: 50 nm.

First, we tested whether the surface density of the Arp2/3 complex at the base of the pit affects endocytic internalization because recent studies in vitro and in yeast suggest that the local concentration of Arp2/3 complex activators is critical for the timing of Arp2/3 complex activation and endocytic progression (Sun *et al.*, 2017; Case *et al.*, 2019). In a series of simulations, we distributed 200 molecules of active Arp2/3 complex in a ring of increasing outer diameter to vary the surface density. Surprisingly, we found that varying the surface density of Arp2/3 complex along the base of the pit by a factor of 20 had little impact on endocytic outcome (Figure 2.6). We also explored whether localization of a fraction of Arp2/3 complexes at the neck of the pit provided an additional advantage for the endocytic outcome. In this scenario, we distributed 50 of the 200 molecules of the active Arp2/3 complex near the neck of the pit. We found

that localizing some of the active Arp2/3 complex near the neck of the pit did not have an impact on the outcome of simulations (p>0.5) (Figure 2.7).
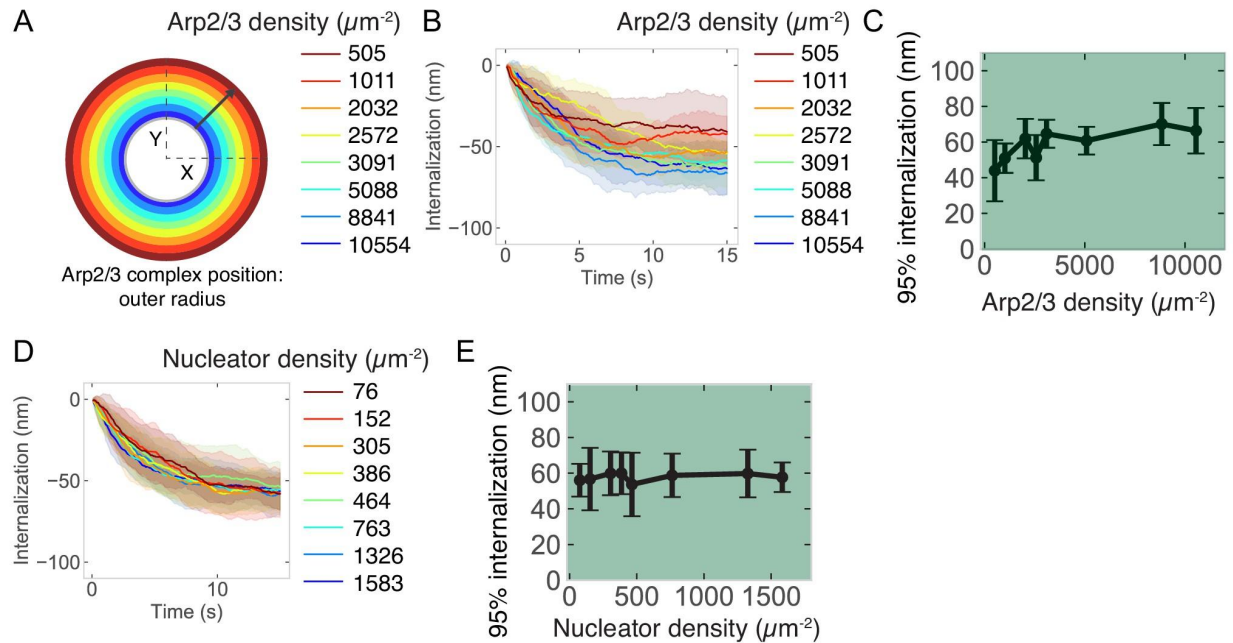
Figure 2.6 Relationship between endocytic outcome and active Arp2/3 complex surface density or mother filament nucleating protein surface density at the base of the pit. (A) Schematic of initial location of active Arp2/3 complex. 200 molecules of Arp2/3 complex were seeded in a ring with an inner diameter of 60 nm (inner gray circle) and an outer diameter of increasing radius (colors) which corresponds to decreasing surface density. (B) Internalization over time for different surface densities of Arp2/3 complex. Color code same as previous panel. (C) Internalization as a function of Arp2/3 complex surface density. n = 72 simulations. (D) Internalization over time for different surface densities of nucleator protein. (E) Internalization as a function of nucleator protein surface density. n = 160 simulations.

We next conducted a series of simulations in which we varied the surface distribution of a constant number of Hip1R molecules to cover between 1% (localized to the tip of the pit) and 80% (up to the neck of the pit) of the pit (Figure 2.5B) and found that the surface distribution of Hip1R around the endocytic pit strongly impacted endocytic outcome (Figure 2.5). Simulations in each of these conditions revealed that endocytic internalization depends on the surface distribution of actin-coat attachments around the endocytic site (Figure 2.5C). Both the rate and extent of internalization increased with increasing surface area of Hip1R around the pit (Figure 2.5D). From a functional standpoint, increased Hip1R surface coverage around the pit drove more barbed ends toward the base of the pit (Figure 2.5E). This increase in Hip1R surface coverage resulted in an increase in Arp2/3 complexes bound in the endocytic actin network (Figure 2.5F), which in turn nucleated more actin filaments (Figure 2.5G). Simulations showed that a threshold of ~100 Hip1R molecules on the pit is necessary for endocytic internalization (Figure 2.8A). The high impact of Hip1R surface distribution on actin filament organization implies that Hip1R molecules distributed broadly around

15

the pit allow for multivalent attachments between the pit and actin filaments, resulting in filaments being captured in an orientation conducive to force production.
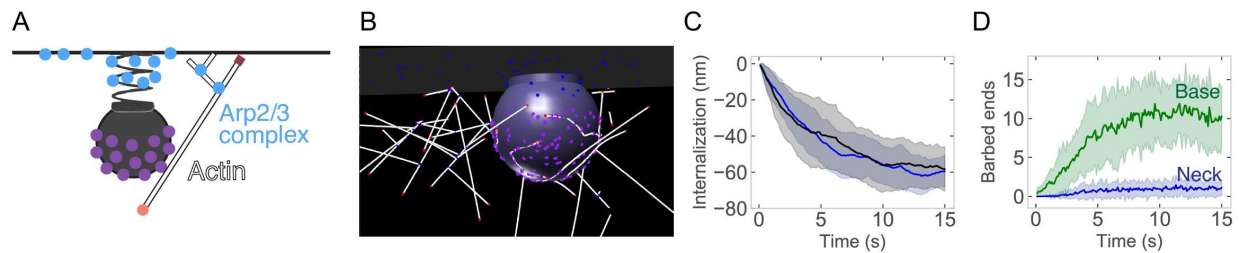
Figure 2.7 A collar of active Arp2/3 complex near the neck of the pit does not affect endocytic outcome. (A) Schematic of active Arp2/3 complex initiated at the base of the pit and a collar near the neck of the pit. (B) Snapshot of simulation with active Arp2/3 complex (blue) near the neck of the pit. Note that the neck can translate in XY slightly (<10 nm) relative to the collar of Arp2/3 complex. (C) Internalization over time with a collar of Arp2/3 complex at the neck (blue) compared to all Arp2/3 complex at the base of the pit (black). No difference in 95% internalization (p>0.5; Welch's t-test). n = 24 simulations per condition. Black curve is 24 of the 96 simulations shown in Figure 2.3D. (D) Number of barbed ends near the neck and base of the pit over time. Compare to Figure 2.3H.

Further examination of the simulations revealed that the Hip1R surface distribution supports a self-organized dendritic actin network via a mechanism of stochastic self-assembly and selection for actin filaments growing toward the base of the pit (Figure 2.8B). Mother filaments initially bind and unbind the coat in random orientations (Figure 2.8B-C). Filaments growing toward the interior of the cell do not template the growth of new branched actin filaments. However, filaments growing toward the base of the pit encounter active Arp2/3 complex, which catalyzes dendritic nucleation of new actin filaments growing in a similar direction (Figure 2.8B and D) (Carlsson, 2001). As a result, near the base of the pit, filaments increasingly orient toward the base of the pit over time (Figure 2.8E-F). Our observations therefore establish an important principle for actin organization in endocytosis: the positions of active Arp2/3 complexes are critical for organizing the actin network and determining the direction of force production, while the Hip1R linker distribution is critical for recruiting mother filaments that activate the Arp2/3 complex to direct filament growth to the area surrounding the base of the pit.
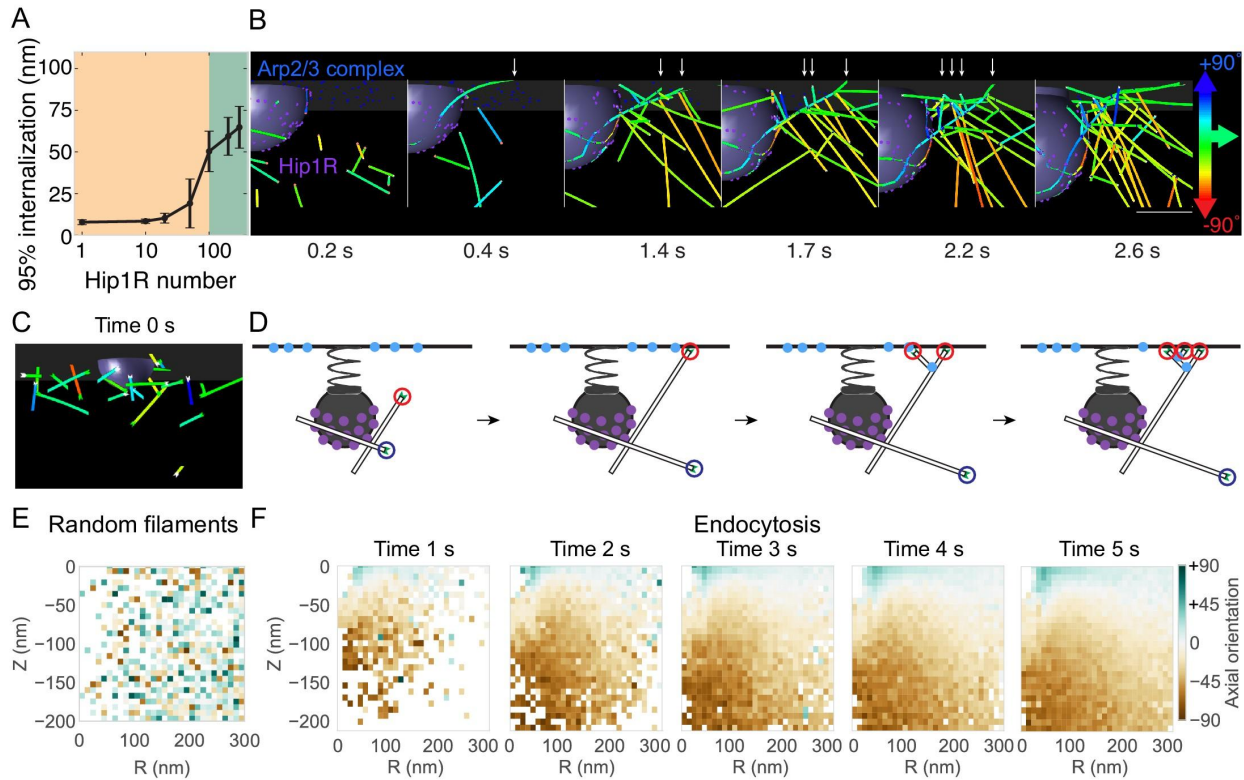
Figure 2.8 Internalization as a function of the number of Hip1R molecules and mechanism of self-organization of endocytic actin filaments. (A) Endocytic internalization as a function of Hip1R number. n = 57 simulations. (B) Time-lapse montage demonstrating endocytic actin self-organization mechanism due to Hip1R spatial distribution around the pit (coverage = 80%). Arrows point to new branched actin filaments nucleated by Arp2/3 complex. Filaments color coded by axial orientation. Scale bar: 50 nm. (C) Snapshot of initial time point of simulation with filaments color coded according to axial orientation. Compare to Figure 2.3B. (D) Schematic illustrating mechanism of stochastic assembly and selection. At initial timepoints, filaments have no preferred orientation. Blue circle highlights filament oriented away from base of pit, which does not encounter active Arp2/3 complex. Red circle highlights filament oriented toward base of pit, which encounters active Arp2/3 complex to template dendritic nucleation of additional actin filaments oriented toward base of pit (green color in panels below). (E–F) Heat maps of filament orientation as a function of radial (R) and axial (Z) position. (E) Simulation of randomly oriented filaments; (F) First five time points of endocytic actin simulation showing establishment of asymmetric orientation for filaments near the base of the pit.

2.2.2 Arp2/3 complex activity and Hip1R/actin attachments are critical for allowing actin filaments to drive endocytic pit internalization and adapt to changing tension

Having established that endocytic internalization depends on two spatially confined boundary conditions – Hip1R/actin attachments at the curved pit and active Arp2/3 complex activity at the base of the pit – we next investigated how these boundary conditions alter the endocytic response to membrane tension (Figure 2.9A).

We systematically varied membrane tension and Arp2/3 complex activity in our model to generate a phase diagram of endocytic internalization as a function of membrane tension and Arp2/3 complex activity (Figure 2.9B). This phase diagram shows that cells with high membrane tension are especially sensitive to changes in Arp2/3 complex nucleation rate (Kaplan *et al.*, 2022), whereas cells with low membrane

17

tension carry out endocytosis even with low Arp2/3 complex activity, consistent with experimental observations (Boulant *et al.*, 2011).

We hypothesized that actin network self-organization arising from the broad Hip1R distribution around the pit and filament bending might allow for the endocytic actin network to change its organization and force-producing capacity under elevated loads. To test this hypothesis, we conducted simulations in which Hip1R coverage was varied for different values of plasma membrane tension (Figure 2.9A). We found that the endocytic actin network's ability to adapt to load depends on Hip1R coverage around the pit (Figure 2.9D–F). As the coverage of Hip1R around the pit increased, actin's ability to adapt to changes in membrane tension also increased, as measured by the number of barbed ends near the base of the pit (Figure 2.9D), the binding of active Arp2/3 complex at the base of the pit (Figure 2.9E), subsequent nucleation of additional actin filaments (Figure 2.9F), and bending of actin filaments near the base of the pit (Figure 2.9G). We conclude that sufficient Hip1R coverage around the pit (Sochacki *et al.*, 2017; Clarke and Royle, 2018) allows endocytic actin filaments to orient in such a way that they can encounter more Arp2/3 complexes at the base of the pit to nucleate more actin filaments. This spatial organization allows the actin network to adapt to sustain force production under a range of opposing loads (Figure 2.9H).
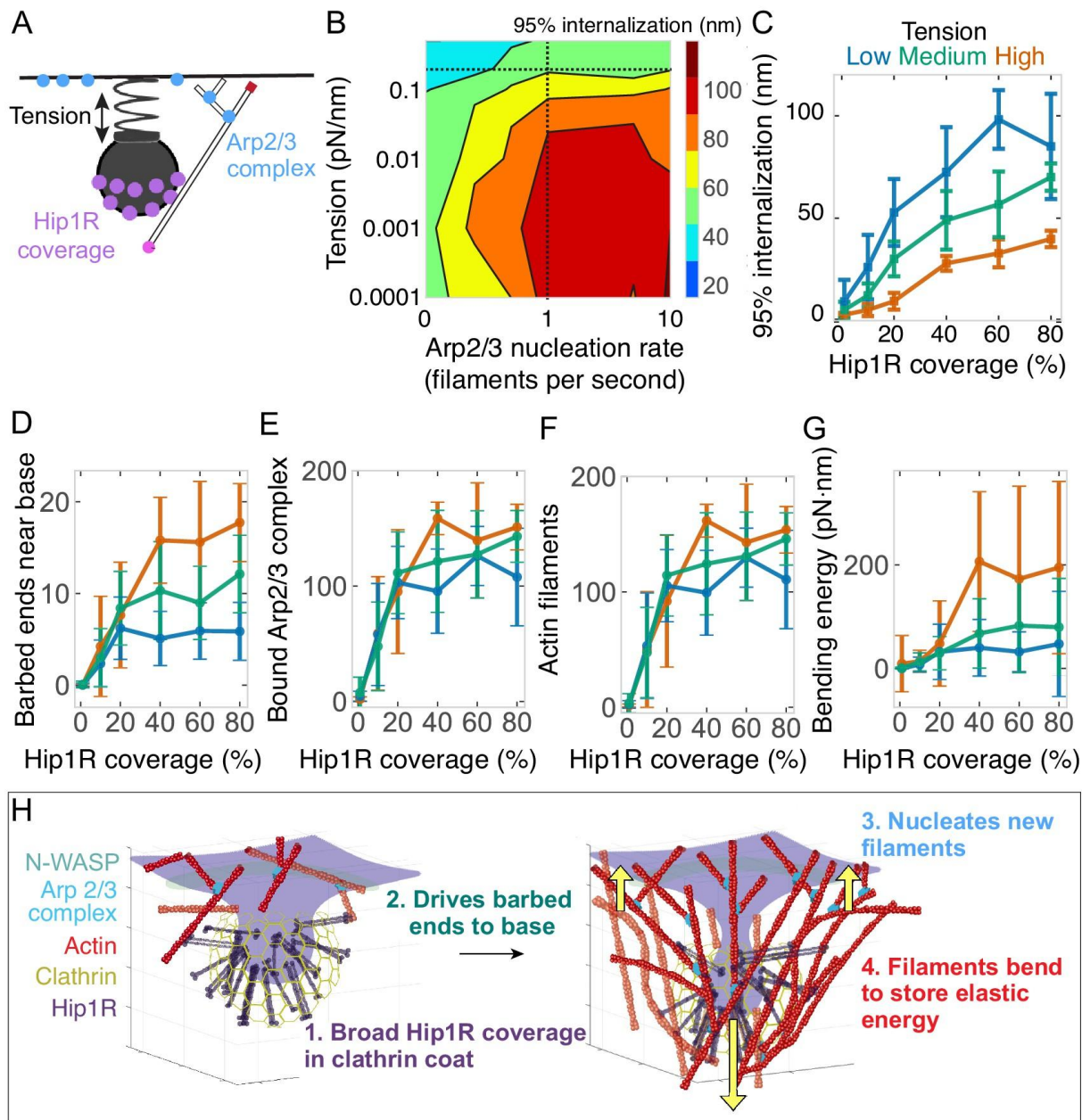
Figure 2.9 Arp2/3 complex activity and Hip1R/actin attachments are critical for allowing actin filaments to drive endocytic pit internalization and adapt to changing tension. (A) Schematic of Arp2/3 complex activity and Hip1R coverage along with membrane tension. (B) Phase diagram of endocytic internalization as a function of membrane tension and Arp2/3 complex nucleation rate shown on a log-log plot. Dotted lines are values taken from the literature (Beltzner and Pollard, 2008; Diz-Muñoz et al., 2016). (C–G) Changes in the endocytic actin network as a function of Hip1R coverage for different values of membrane tension. Low tension = 0.015 pN/nm; medium tension = 0.15 pN/nm; high tension = 1 pN/nm. n = 288 simulations. (C) Internalization; (D) Number of barbed ends near base of pit; (E) Number of Arp2/3 complexes bound in network; (F) Number of actin filaments bound in network; (G) Bending energy of filaments with barbed ends near the base of the pit. Mean ± standard deviation of time points in the last 5 s of simulations. (H) Summary of load-dependent adaptation of self-organizing endocytic actin network due to spatial segregation of active Arp2/3 complex at the base and Hip1R in a broad distribution within the clathrin coat.

2.3 Conclusion

Understanding the relationship between actin filament assembly, actin network organization, and force generation on the plasma membrane requires iterative feedback between experimental measurements and computational modeling. An ultimate goal of this study was to relate single actin filament mechanics to force generation by the collective actin filament network in CME (Lacayo *et al.*, 2007). We integrated modeling and quantitative cellular measurements to show that a minimal actin network composed of actin, the Arp2/3 complex and capping protein, with linker attachments in the clathrin coat and rates constrained by cellular and biochemical measurements, is able to generate sufficient force to internalize endocytic pits against mammalian plasma membrane tension. Approximately 200 Arp2/3 complexes constitutively assemble at sites of endocytosis in human induced pluripotent stem cells. Endocytic actin filaments self-organize into a radial dendritic array, in which filaments grow toward the base of the pit. These filaments bend and store elastic energy, which supports internalization. The endocytic actin network adapts to changes in membrane tension by driving more filaments to the base of the pit and increasing filament bending, which supports a higher load and nucleates more actin filaments.

Four lines of experimental evidence support our model. Two pieces of evidence serve as model validation based on published data and two more are based on experiments conducted by my collaborators for this study (Akamatsu *et al.*, 2020). Previous experiments from our lab showed that knocking down Hip1R in HeLa cells inhibited endocytosis (Engqvist-Goldstein *et al.*, 2004). Consistent with these observations, our simulations showed that a threshold number of actin linkers such as Hip1R is necessary for endocytic internalization (Figure 2.8A). This threshold appears necessary to allow efficient filament capture by the coat and force transmission from the actin network to the coat. Second, experiments showed that capping actin filament elongation with the small molecule compound Cytochalasin inhibits CME, reflected by an increase in stalled endocytic sites marked by clathrin-RFP (Brady *et al.*, 2010) or slower accumulation of dynamin2-GFP at endocytic sites (Grassart *et al.*, 2014). We also showed in our model that capping rate is an important parameter for progression of CME; our simulations show that increasing the capping rate of actin filaments inhibits CME, presumably because increasing capping decreases the total amount of actin (Figure 2.2C). In this study, our simulations predicted that actin filaments bend around endocytic pits. These bent filaments store elastic energy for subsequent force production much as a pole vaulter's pole bends and stores energy for delayed force production. Using cryo-electron tomography of intact cells, my collaborators observed bent actin filaments at sites of endocytosis in mammalian cells (Akamatsu *et al.*, 2020). Finally, we also predicted that inhibiting Arp2/3 complex activity below its basal

nucleation rate of 1 filament per second inhibits endocytosis in silico and this prediction was validated in cells using pharmacological agents (Akamatsu *et al.*, 2020). Without sufficient Arp2/3 complex, CME fails due to insufficient force production.

Three main conclusions resulted from our study. First, we found that the spatial segregation of Arp2/3 complex activation and Hip1R linker proteins on the clathrin coat are important factors for effective force generation. Unlike actin organization at the leading edge of a migrating cell wherein only one boundary condition at the plasma membrane is sufficient to enable force-generation capacity to be inferred (Abercrombie, 1980; Mogilner and Edelstein-Keshet, 2002; Bieling *et al.*, 2016), in CME two boundary conditions are required – one at the base of the pit for actin polymerization against the plasma membrane and the second on the coat of the pit for attachment of the growing actin filaments so forces are transmitted to the pit to drive internalization. In our model, we used Hip1R as a surrogate for Hip1, Hip1R, and Epsin1/2/3, which cooperatively link actin filaments to the coat (Chen *et al.*, 1998; Senetar, Foster and McCann, 2004; Brett *et al.*, 2006; Skruzny *et al.*, 2012; Messa *et al.*, 2014). We conclude that based on the relative positions of Arp2/3 complex activators and actin filament linkers, the resultant self-organized actin network orients to produce force orthogonal to the base of the pit rather than producing a pinching force on the neck (Collins *et al.*, 2011; Hassinger *et al.*, 2017). Pinching forces are achieved by the spontaneous curvature of the rigid coat (Foret, 2014; Hassinger *et al.*, 2017; Alimohamadi *et al.*, 2018). Any constriction forces generated by actin polymerization at the neck would likely occur at a later stage of endocytosis than is the focus of our model, and the filaments would need to be nucleated by a spatially distinct set of Arp2/3 activating proteins around the neck, or by an interaction between other actin filaments and dynamin, but the mechanism for arranging and anchoring such a network has not been elucidated (Ma and Berro, 2018).

Second, the effective anchoring of actin filaments to the surface of the pit depends on the distribution of linker proteins on the pit surface. Since these linker proteins are embedded within the clathrin coat (Engqvist-Goldstein *et al.*, 2001; Sochacki *et al.*, 2017; Clarke and Royle, 2018), their surface coverage is directly proportional to the coat coverage on the endocytic pit. This observation suggests that one possible function of a large coat is for the actin-linking proteins Hip1, Hip1R and Epsin to cover enough surface area to provide leverage for internalization. The role of linker protein coverage in force generation also has implications for the flat-to-curved transition earlier in endocytosis, when the membrane either begins to bend from a flat pre-assembled coat or continually deforms while the coat assembles (Avinoam *et al.*, 2015; Bucher *et al.*, 2018; Scott *et al.*, 2018; Sochacki and Taraska, 2018). In cases when the clathrin coat gradually increases in area during membrane deformation, our findings imply that actin polymerization may be ineffective until the coat reaches a threshold size (Avinoam *et al.*, 2015; Sun *et al.*, 2017), with membrane tension controlling a switch for the flat-to-curved transition (Bucher *et al.*, 2018; Scott *et al.*,

2018). Future work will investigate the relationship between coat topology and actin forces during the initiation of endocytosis.

Third, we showed a significant fraction of endocytic actin filaments bend under force. We predict that the bent filaments, whose existence we confirmed by cryo-electron tomography of intact cells, contribute to successful endocytic internalization in at least two ways. First, they might contribute to the resilience of endocytosis by preventing backsliding of the pit. Second, we expect that they contribute to internalization by releasing stored elastic energy when they straighten out under thermal fluctuations, consistent with the elastic Brownian ratchet mechanism for actin-mediated force production (Mogilner and Oster, 1996; De La Cruz and Gardel, 2015). Here, filament bending occurs to a greater extent and for a longer time than previously described for coherent flat surfaces like the leading edge, possibly due to the curved geometry of endocytic pits. Fixing the filament orientation at one end increases bending energy (Fernández, Pullarkat and Ott, 2006; De La Cruz, Martiel and Blanchoin, 2015), which is accomplished here by multivalent attachments from Hip1R. Previous studies overlooked the role of actin filament bending at endocytic sites because of the predicted short length of filaments based on population averages (Berro *et al.*, 2010) and the possible loss of less densely branched filaments during the preparation process for platinum-replica electron microscopy (detergent extraction or sonication-based unroofing) (Collins *et al.*, 2011). The load response of branched actin networks in vitro can be reversible due to filament bending (Chaudhuri, Parekh and Fletcher, 2007), or permanent from a change in filament architecture (Parekh *et al.*, 2005; Bieling *et al.*, 2016). In further simulations performed by my collaborators, some of the elastic energy from bent filaments is released as internalization increases, suggesting a reversible compression of the network to store elastic energy (Akamatsu *et al.*, 2020). However, a significant fraction of filament bending is retained after the spring is released, which suggests that load also changes the intrinsic structure of the network (Bieling *et al.*, 2016).

Importantly, the results presented here demonstrate a mechanism of active adaptation by the endocytic actin network to changes in load (Figure 2.9). Different cell types, different locations in the same cell, and different stages of endocytosis at the same location can have different membrane tension values at different times (Shi *et al.*, 2018). Under flat geometries, branched actin networks adapt to load (Bieling *et al.*, 2016; Mueller *et al.*, 2017). Here, the distribution of Hip1R linkers around the pit directs more filaments to grow toward the base of the pit, which nucleates more filaments autocatalytically and increases filament bending, thereby supporting greater internalization.

It is now important to determine whether the principles of actin filament self-organization and load adaptation identified here also apply to endocytic actin in the higher force regime characteristic of fungi. An agent-based model of endocytic actin networks in yeast predicted that barbed filament ends radiate away from the center of pit in the XY plane (Mund *et al.*, 2018). However, the >200x larger force

requirements in this organism lead to a different axial organization of the filaments, less filament bending, and a distinct mechanism of force production sufficient to counteract high turgor pressure. Understanding the mechanical function and load adaptation in the 'soft' regime studied here is likely to apply to a variety of cellular membrane bending processes employing branched actin networks, including the assembly and maturation of endosomes, lysosomes, and autophagosomes (Rottner *et al.*, 2017).

Finally, we acknowledge that our model represents a minimal core actin machinery necessary for endocytic internalization in mammalian cells. This feature of our study was necessary so the number of free parameters could be limited. Future models will add complexity to test roles for filament crosslinking, filament severing, and myosin-I motor activity, among other factors. It is anticipated that these additional features will increase our understanding of the force-generation capability and overall efficiency of the endocytic actin network.

2.4 Materials and Methods

2.4.1 Membrane mechanics module

As this portion of the research was carried out by collaborators, refer to (Akamatsu *et al.*, 2020) for an explanation of the continuum mechanics methods.

2.4.2 Actin module

We used Cytosim (Nedelec and Foethke, 2007) to model the polymerization of a branched actin network coupled to the internalization of a clathrin-coated pit. This approach simplified the pit as a bead attached to a flat boundary (the plasma membrane) by a spring. This assumption of a linear force-extension relationship was validated in Figure 2.1. Actin filaments and actin-binding proteins (Arp2/3 complex, Hip1R) were explicitly simulated as individual objects (agents). Cytosim calculates the forces on each segment of actin from rules such as diffusion, confinement, growth, and binding based on Brownian dynamics.

2.4.2.1 Assumptions in Cytosim

Cytosim simulates the movement of actin model points within a boundary according to constrained Langevin dynamics (Nedelec and Foethke, 2007), which accounts for the diffusion, bending, and forces of actin filaments, as well as the diffusion and binding of actin-binding proteins detailed below.

1. Force balance equations (Nedelec and Foethke, 2007) section 7.1:
    1. All points in the simulation follow constrained Langevin dynamics:
    2. $dx = \mu F(x, t)dt + dB(t)$
        1. where μ is defined as an effective mobility, which takes on a different value for each type of object.
2. Mobilities of diffusing objects:

1. The simulated Brownian motion $dB(t)$ of objects of radius r is governed by a uniformly distributed random $[0, 1]*\sqrt{kBT/3\pi\eta}$ number at each time point, where η is the viscosity of the cytoplasm.
2. Their movement is governed by a mobility μ
    1. For model points of an actin filament, $\mu = log(L/\delta)/(3\pi\eta L)$ for a rod of diameter δ, length L and cytoplasmic viscosity η. This mobility term ignores the bending of the filaments.
3. The endocytic pit is modeled as a solid, with bulk fluid viscosity associated with pit translational movement and a viscoelastic confinement to the cell surface: $dx = \mu F(x, t)dt + dB(t)$, where $\mu = 6\pi\eta r$.
3. Confinement of objects:
    1. Objects are confined within a boundary (cell surface) according to a harmonic spring potential $F = kx$.
        1. The endocytic pit a distance z from the cell surface experiences a force $F = kz$.
        2. Actin filaments are confined inside the cell wherein each model point at distance z outside the cell experiences a force $F = kz$.
4. Bending elasticity of filament model points:
    1. Filament model points are connected via linear elasticity according to a flexural rigidity κ, which is the persistence length Lp multiplied by kBT.
    2. The bending elasticity is treated as linear (see Limitations) such that for three connected actin model points $m0, m1, m2$ the force for those points is $F = \kappa(p/L)3(m0 - 2m1 + m2)$, where κ is the flexural rigidity, p is the number of model points, and L is the length of the filament.
5. Actin-binding proteins
    1. Hip1R binds actin filaments according to a binding rate and binding radius (probability of binding when a filament is within the binding radius). This general actin-binding protein is a simplification of the multiple interacting proteins that link actin to the coat, including Hip1 and Epsin1/2/3 (Chen *et al.*, 1998; Senetar, Foster and McCann, 2004; Brett *et al.*, 2006; Skruzny *et al.*, 2012; Messa *et al.*, 2014).
    2. Arp2/3 complex was developed as a special-case 'fork' class with two coupled ends. One end binds actin filaments, and the other nucleates a new actin filament, provided the first end bound an actin filament (this is defined as trans-activation in Cytosim). In the 'fork' class, the two ends are constrained geometrically at a resting angle with a given resistance to torque (angular stiffness) similar to 4b above (Mund *et al.*, 2018).

2.4.2.2 Assumptions for modeling mammalian clathrin-mediated endocytosis in cytosim

2.4.2.2.1 Geometry

Endocytic pit: We used our membrane mechanics simulations (Figure 2.1) (Hassinger et al., 2017) to estimate the dimensions of the endocytic pit for physiological values of membrane tension and rigidity of the membrane and clathrin coat. Under these conditions the clathrin coat bends the plasma membrane into a U-shaped hemisphere (Figure 2.1) (Yarar, Waterman-Storer and Schmid, 2004; Boulant et al., 2011; Messa et al., 2014). We initialized the pit as a hemisphere 90 nm in diameter (Collins et al., 2011, p. 20; Avinoam et al., 2015). As the pit internalizes, a smaller neck is exposed (Figure 2.1), which is modeled as a sphere with a cylindrical neck of diameter 60 nm. Internalization is defined as a displacement in the -Z direction (Figure 2.1A).

Active Arp2/3 complex: We collapsed the activation steps of Arp2/3 complex into a single species, active Arp2/3 complex, that resides on the plasma membrane from the beginning of the simulation. This models the cellular process, in which soluble Arp2/3 complex is inactive until it encounters its activator N-WASP at the plasma membrane.

N-WASP binds the plasma membrane via a PI(4,5)P2-binding site (which relieves its own autoinhibition) (Rohatgi, Ho and Kirschner, 2000). Additional proteins can bind different regions of N-WASP to increase its level of activation, including the GTPase Cdc42, actin nucleator cortactin, and BAR protein SNX9. Because the activation rate and concentrations of these proteins are not yet known, we considered fully active N-WASP (similar to the VCA region alone) rather than modeling the individual activation steps. Furthermore, rather than explicitly modeling N-WASP, we used pre-activated Arp2/3 complex, which models the coincidence of active N-WASP with soluble Arp2/3 complex on the plasma membrane. This active Arp2/3 complex can template new branched actin filaments when in proximity of an existing 'mother' actin filament. Thus, this model aims to functionally capture Arp2/3 complex activation and the geometry of branched actin filament nucleation, rather than explicitly modeling each molecule involved in the process of Arp2/3 complex activation.

N-WASP (or its homologues Las17/WASP in yeast) accumulates earlier in endocytosis (Taylor, Perrais and Merrifield, 2011) until a 'threshold' concentration triggers actin assembly (Sun et al., 2017); here we initialize all the active Arp2/3 complex on the plasma membrane at the beginning of the simulation, and it is used over the course of the simulation. Therefore we model the phase in which a threshold value of Arp2/3 complex activators has accumulated at the endocytic site and is ready to trigger actin polymerization.

We assumed that activated Arp2/3 complex resides in a ring around the base of the endocytic pit. This feature has been shown for the budding yeast homologue of N-WASP, Las17 (Picco et al., 2015). Endocytic actin polymerizes from the base of the

pit in budding yeast (Kaksonen, Sun and Drubin, 2003; Idrissi et al., 2008; Picco et al., 2015; Mund et al., 2018) and in mammalian cells (Almeida-Souza et al., 2018; Kaplan et al., 2022), consistent with active Arp2/3 complex residing in a ring at the base of the pit. In our fluorescence micrographs, Arp2/3 complex is diffraction-limited, so the outer diameter of this ring is ≤250 nm. The inner diameter of the ring of Arp2/3 complex corresponds to the width of the neck of the pit, 60 nm. In budding yeast the Las17 ring outer diameter is ~140 nm (Mund et al., 2018), which corresponds to a surface density of ~3000 molecules/μm^2. We conservatively set the outer radius of the ring to be 240 nm, which also corresponds to a surface density of ~3000 molecules/μm^2. Estimates of the surface density of in vitro and in vivo patterned activators of Arp2/3 complex (also called nucleation-promoting factors) range from ~3000–19000 molecules/μm^2 (Ditlev et al., 2012; Bieling et al., 2018; Case et al., 2019).

2.4.2.2.1 Filament attachments to endocytic pit

In mammalian cells, Hip1R and Epsin connect actin filaments to the endocytic pit (Chen *et al.*, 1998; Engqvist-Goldstein *et al.*, 2001; Senetar, Foster and McCann, 2004; Brett *et al.*, 2006; Skruzny *et al.*, 2012; Messa *et al.*, 2014). Both are present throughout the clathrin coat (Sochacki *et al.*, 2017; Clarke and Royle, 2018). We wrote a script in Matlab to uniformly distribute Hip1R molecules around a desired coverage of a sphere, from 1% to 80% of a sphere (Figure 2.5). In most simulations Hip1R was distributed in 60% of a sphere.

2.4.2.2.1 Modeling actin filament dynamics

Stall force: Filament polymerization slows under applied load according to the Brownian Ratchet theory (Peskin, Odell and Oster, 1993). This is treated in Cytosim as growth velocity that slows exponentially under applied load, which is reasonable within the time scales of endocytosis.

2.4.2.2.1 Modeling filament capping

Previous filament-based models of actin in endocytosis modeled actin filaments with uniform lengths or that grow until a maximum length (Mund *et al.*, 2018), while others took into account stochastic capping without diffusion or bending (Wang *et al.*, 2016). We adapted an existing property in Cytosim to model stochastic filament capping, such that the capping events were exponentially distributed. We modeled actin filaments using Cytosim's 'classic' fiber class, which treats the filament as growing from its plus end, with a stochastic probability of depolymerizing (corresponding to catastrophe for microtubules). We set the depolymerization rate of shrinking filaments to be 0 with no recovery rate. Thus these filaments become irreversibly capped after an exponential wait time characterized by the parameter catastrophe_rate (which we define as the capping rate). Because the probability that capping protein binds to the barbed end of the filament is exponentially distributed,

filament lengths are exponentially distributed (Figure 2.4F). We set the rate of capping to achieve a desired mean filament length based on the expected distributions of actin filament lengths for a given capping rate. In Cytosim, the catastrophe rate can be set to depend on a combination of applied load and growth velocity, which we did not include in our model of actin filament capping.

2.4.2.2.1 Source of actin mother filaments

Active Arp2/3 complex requires a mother filament from which to nucleate a new actin filament at a defined angle (Mullins, Stafford and Pollard, 1997; Amann and Pollard, 2001). Therefore, the polarity of the mother filament defines the polarity of the resultant branched actin network. Our study uses diffusing linear actin filament nucleating proteins (Basu and Chang, 2011; Wagner *et al.*, 2013; Balzer *et al.*, 2018) to seed a defined number of randomly oriented mother filaments near the endocytic site. Alternatively, simulations using a pool of cytoplasmic linear actin filaments (Raz-Ben Aroush *et al.*, 2017) allowed for similar internalization, but with less reliable timing of initiation. More detailed studies of the mechanism of actin nucleation and mother filament generation are necessary.

2.4.2.2.1 Limitations

Endocytic pit internalization is simplified as an elastic spring, with a linear relationship between force and extension. We show in Figure 2.1 that this linear relationship is characteristic of coated plasma membranes under force up until a threshold internalization of ~100 nm. Future studies will treat the coated membrane as a 3D, force-dependent curving surface; such an approach is outside the scope of the present work.

We focus our model on the minimal actin machinery required to produce force. We have not included crosslinkers (Ma and Berro, 2018) or myosin I, both of which are expected to increase the network's ability to produce force. The effects of these two proteins on mammalian endocytosis will be treated in a future study.

The treatment of filament bending elasticity as linear is valid for small deflections of individual actin model points. Importantly, the outcomes of our simulations did not depend on the frequency of segmentation of actin model points (which change the magnitude of deflection between individual actin model points). Filament twist or twist-bend coupling, which increases the total energy stored in bent actin filaments (De La Cruz, Martiel and Blanchoin, 2015), is not considered in Cytosim, and requires a more detailed modeling approach considering each subunit. Cytosim does not implement hydrodynamics for curved filaments, so the diffusion of these filaments is approximated as the motion for a linear filament.

Arp2/3 complex preferentially binds to the curved sides of actin filaments (Risca et al., 2012). We do not include this assumption in our model. We expect that the self-organization and robustness exhibited by our minimal actin network would be

enhanced by this assumption, given that Arp2/3 complex at the base of the pit encounters many curved sides of actin filaments.

2.4.2.3 Parameter values

We derived most parameters from experimental data in the literature, and made measurements for some measurements not available. We varied the remaining parameters to show their effect on the outcome of the simulations. Discussion of each parameter follows below.

2.4.2.3.1 Membrane tension

We used the relationship between internalization resistance and membrane tension (Figure 2.1) to calibrate the spring stiffness in our agent-based simulations. We relied on values of membrane tension measured in human skin melanoma SK-MEL-2 cells, based on atomic force microscope membrane tether rupture forces and the assumption that the rigidity of the plasma membrane is 320 pN·nm (Dimova, 2014; Diz-Muñoz *et al.*, 2016; Kaplan *et al.*, 2022).

2.4.2.3.1 Association rate constants

The biochemical association rate constant, k_{on}, is given in units of $\mu M^{-1}\ s^{-1}$. In Cytosim, we input the association probability between actin and a binding protein as a binding_rate, in units of s^{-1}. These two rates can be related by the following relationship: $kon = binding\_rate * capture\_volume$, which is defined as $\pi * capture\_radius2 * filament\_length$ (Francois Nedelec, personal communication). This gives an order-of-magnitude scaling relationship to convert between k_{on} and binding rate, considering that cytosim does not treat explicit binding sites on the filament (Francois Nedelec, personal communication).

2.4.2.3.1 Arp2/3 complex

Branching angle: Based on (Blanchoin *et al.*, 2000) we set the branching angle of Arp2/3 complex to be 77 ± 13°, as measured for bovine Arp2/3 complex. Acanthomeba Arp2/3 complex adopts closer to a 70° branching angle. In NIH3T3 cells preserved by cryo-fixation, branch angles in the lamellipodium are 77 ± 8° (Vinzenz *et al.*, 2012). Importantly, (Blanchoin *et al.*, 2000) was the only in vitro study we are aware of that measured the variance of branching angles, which was converted to an angular stiffness (0.076 pN/rad^2). Therefore we set the resting angle of Arp2/3 branches as 1.344 rad with an angular stiffness of 0.076 pN/rad^2.

2.4.2.3.1 Unbinding rate

We used the $koff$ measured by (Beltzner and Pollard, 2008): 0.003s^{-1}.

2.4.2.3.1 Nucleation rate

Based on the association rate constant between activated Arp2/3 complex and actin filaments of 0.00015 µM^{-1} s^{-1} (Beltzner and Pollard, 2008), we set the binding_rate of Arp2/3 to actin to be 7 s^{-1}, given a capture radius of 10 nm and filament length of 100 nm (see relationship between these parameters above). We note that this calculation of $_{binding\_rate}$ depends inversely with the filament length (and number of filaments) which are not directly comparable in our simulations given that the filaments and Arp2/3 are generally not freely diffusing. Still, it was remarkable that our best estimate for $_{binding\_rate}$ gave reasonable nucleation kinetics, and served as a threshold for timely internalization of the endocytic pit, whereas previous deterministic models needed to increase the association rate constant by 300-600x for efficient nucleation (Beltzner and Pollard, 2008; Berro *et al.*, 2010). These ODE models did not have spatial considerations, so this suggests that the spatial and temporal confinement of actin filaments and the high local concentration of active Arp2/3 complex in our simulations accounted for most of this difference. Thus the local geometry has a significant (>2 orders of magnitude) effect on the effective nucleation rate.

2.4.2.3.1 Actin

Growth rate: In cells the cytoplasmic concentration of actin is 60–100 µM (Haugwitz et al., 1994; Wu and Pollard, 2005). In mammalian cells, a subset of this actin is available as polymerizable actin, both due to monomer-sequestering proteins (thymosin B4) and due to only a subset of monomers being ATP-bound. We conservatively set the concentration of available polymerizable actin to be 20 µM, which given the association rate constant of ATP-actin of 11.6 subunits/µM/s (Pollard, 1986) corresponds to a polymerization rate of 500 nm (182 subunits) per second.

Capping rate: The mean length of filaments in mammalian endocytosis has not been measured. We relied on the estimates from (Berro et al., 2010; Sirotkin et al., 2010)which showed that for fission yeast filaments were an average of 150 nm in length. We set the capping rate to be 6.3/s, which set the mean filament length at 150 nm. We varied the rate of capping in our simulations. Less actin capping resulted in greater internalization, due to more actin (Figure 2.2). However, the resultant amount of actin is larger than the amount of actin measured in CME in other organisms (Sirotkin et al., 2010; Picco et al., 2015).

Stall force: The stall force scales with the load applied and the concentration of actin monomers available (Peskin, Odell and Oster, 1993). At 4 µM actin the filaments' stall force was measured to be 1–2 pN (Footer et al., 2007). With 40 µM actin the filaments could theoretically stall at up to 9 pN force per filament (Dmitrieff and Nédélec, 2016). For the ~20 µM actin that we assumed was available for polymerization, the stall force was ~5 pN. Surprisingly, the extent of internalization varied weakly with stall force (Figure 2.2), suggesting that actin used another mode of force generation than elongation directly against the membrane.

Persistence length: We set the persistence length of actin filaments to be 10 µm, which corresponds to a flexural rigidity of 0.041 pN·µm^2 (McCullough et al., 2008). Previous modeling studies used a value of 20 µm, based on measurements of actin filaments labeled with phalloidin (Gittes et al., 1993), which stiffens actin filaments (Isambert et al., 1995; Pfaendtner et al., 2010). Changing the persistence length of actin between 1 and 20 µm had a minor effect on pit internalization (Figure 2.2).

2.4.2.3.1 Hip1R

In mammalian endocytosis, several proteins link actin filaments to the clathrin coat via phosphoinositide- and clathrin-binding domains and actin-binding domains, including Hip1, Hip1R, and Epsin (Chen et al., 1998; Senetar, Foster and McCann, 2004; Brett et al., 2006; Skruzny et al., 2012; Messa et al., 2014). Our general linker protein, named in the text as Hip1R, is a surrogate for all proteins that link actin to the coat.

Endocytic actin-binding proteins Hip1 and Hip1R use a conserved domain to bind actin with surprisingly weak affinity. This domain, which is alternately named the THATCH (Talin- Hip1/R/Sla2p Actin-Tethering C-terminal Homology), Talin-family, or I/LWEQ domain, has been isolated and studied by several groups. We fit the binding results of previous Hip1R binding experiments in our lab (Engqvist-Goldstein et al., 1999) to estimate a binding affinity between Hip1R and actin as ~400 nM, and the affinity between clathrin cages and Hip1R to be ~1 nM. Both sets of data were fit well by the quadratic binding curve (Pollard, 2010),

$$[LR]/[L] = (([R] + [L] + Kd) - (([R] + [L] + Kd)2 - 4*[R]*[L])1/2/(2*[L])$$

where $[L]$ is the concentration of actin or clathrin and $[R]$ is the concentration of Hip1R, with r^2 = 0.94 and 0.99, respectively (data not shown). Other studies measured a weaker affinity between Hip1R and actin: K_d = 3.4 µM, or 2.5 µM for Hip1 (Senetar, Foster and McCann, 2004). In the presence of the first helix of the five-helix bundle comprising the THATCH domain, actin affinity further decreases (Senetar, Foster and McCann, 2004). Epsin has two actin-binding domains with very weak (K_d >10 µM) or unknown affinity to actin (Skruzny et al., 2012; Messa et al., 2014). For our linker protein we used a combination of rate constants such that k_{off}/k_{on} ~ K_d of 400 nM. Compared with dilute reactions, in an endocytic geometry actin filaments grow near the coat, so the actin filaments bind Hip1R more frequently. As a result we found that a relatively low binding rate was sufficient for binding between actin and Hip1R in our simulations. We varied the off rate of Hip1R and found that, surprisingly, the internalization was robust to Hip1R off rate between 0.001 and 10 s^{-1} (Figure 2.2).

With such weak affinity, ≥100 linking molecules are required for robust endocytosis (Figure 2.5). The following considerations support the likelihood that a sufficient number of actin-linking proteins reside in the clathrin-coated pit. In yeast, endocytic sites accumulate ~100–150 molecules of the Hip1R homologue End4p and

230 molecules of the actin-binding protein Pan1 (with K_d to actin = 2.9 µM). Estimation from platinum replica images of clathrin-coated pits in SK-MEL-2 cells (Sochacki et al., 2017) suggest that clathrin cages have approximately 55 ± 12 'faces' (pentagons and hexagons), or up to 90 faces in HeLa cells. If the cage accumulates one Hip1R dimer per face, this would lead to 110–180 molecules of Hip1R, plus molecules of Hip1, Epsin1, Epsin2, and Epsin3. From a similar analysis, SK-MEL-2 cells have ~66 ± 12 vertices (triskelia), which corresponds to ~200 ± 40 clathrin heavy chains and ~200 ± 40 light chains. Since Hip1R binds clathrin light chain, a 1:1 ratio of these proteins would again suggest ~200 Hip1R molecules in the clathrin coat. Additionally, actin binding by these linker proteins is likely highly multivalent. Mammalian Epsin proteins hexamerize in vitro via their membrane-binding ENTH domains, and Hip1 and Hip1R can dimerize with each Epsin through its ANTH domain by sharing a Pi(4,5)P2 molecule (Skruzny et al., 2015; Garcia-Alai et al., 2018). Adding an additional layer of multivalency, Hip1R and Hip1 hetero- and homodimerize via coiled-coil domains and a C-terminal dimerization motif (Engqvist-Goldstein et al., 2001; Senetar, Foster and McCann, 2004; Chen and Brodsky, 2005; Brett et al., 2006; Niu and Ybe, 2008). Therefore, it is quite likely that a sufficient number of actin-linking proteins cover the coat.

2.4.2.3 Simulation environment parameters

The internalization of endocytic pits was not sensitive to other simulation parameters including the segmentation of actin (1 and 100 nm per model point; 1 µm model points introduced additional variability), confinement force for actin within the cell, and time step of the simulation (Figure 2.2). The viscosity of the cytoplasm and the endocytic pit weakly affected extent of internalization (Figure 2.2).

2.4.2.3 Modifications to source code

We added a method 'confine_first_surface' in which only the first segment of the multi-point bead is under confinement, and that the bead does not undergo angular displacements.

We added data reporting methods, including (1) reporting the Arp2/3 complex branch angle (Francois Nedelec); (2) reporting the Hip1R-attached filament ID numbers; (3) visualizing the axial orientation of actin segments with respect to the plasma membrane (implemented as 75% of the hsv colormap).

2.4.2.3 Comparison to theory

Our calculation of the elastic energy stored in bent actin filaments is derived from the theory of deforming elastic beams (Boal). Specifically, the bending energy E is determined by $(kBTLp\theta2)/(2l)$, where kB is the Boltzmann constant, T is temperature, Lp is the filament persistence length (10 µm for actin), θ is the bending angle, and l the

free filament length (contour length of the filament between the attachment site and barbed end of the filament).

2.4.2.3 Running simulations

We wrote custom scripts in bash to run parallel simulations on a high-performance computing server.

2.4.2.3 Analysis of simulations

We wrote custom code in Python (3.7) with Jupyter Notebook (Project Jupyter) to read, analyze, and plot the simulations obtained from Cytosim. X,Y = 0 is defined as the center of the pit. Energy associated with polymerization was defined as 5 pN * 2.75 nm = 13.5 pN·nm per binding event. This code is available at the following website: https://github.com/DrubinBarnes/Akamatsu_CME_manuscript (Akamatsu, 2019; copy archived at https://github.com/elifesciences-publications/Akamatsu_CME_manuscript).

2.4.2.3 Internalization energy

We used the relationship $E = 1/2kx^2$ to estimate the expected internalization for a non-adapting machine. From the internalization for k = 0.01 pN/nm (low tension), we calculated the expected internalization using the same energy for different values of k. Specifically, for a single value of load, we calculated the work output based on energy (work output) $E = 1/2kx^2$, where k is the load (in pN/nm) and x is the internalization (in nm). For an adapting network, the work output changes with load. For a non-adapting network, it does not, so as load k increases, internalization x decreases. Energy efficiency is defined as the energy (of internalization or stored in bent filaments) divided by the total polymerization energy.

Radial orientation metric: We defined the radial orientation as the sum of the dot products of the direction of the barbed end with the unit vector in X and Y, such that −1 = barbed ends oriented toward the origin (the center of the pit), 0 = oriented tangent to the pit, and +1 = oriented away from the center of the pit.

95% internalization is defined as the 95th percentile of internalization. We use the first 12 s of simulations to allow for comparison with simulations that terminated after t = 12 s. For Figure 2.7, we compared 95% internalization in two conditions using the Welch's t-test in Python (3.7) with scipy.stats.ttest_ind(equal_var = False).

Barbed ends near base/neck: We chose a distance of 7.5 nm as a metric for proximity to the membrane (base or neck) as this was the width of 1–2 actin monomers and less than the radial distance between the neck surface and the pit diameter. The absolute value of this metric did not change the results appreciably.

Chapter Three

Self-organizing actin networks drive sequential endocytic protein recruitment and vesicle release on synthetic lipid bilayers

This chapter contains material published in the reference (Stoops *et al.*, 2023) in collaboration with co-authors Emily Stoops, Danielle Jorgens, and David Drubin.

3.1 Introduction

Endocytic protein recruitment follows a precise order and timing (Kaksonen, Sun and Drubin, 2003; Merrifield and Kaksonen, 2014), and can be roughly subdivided into a variable early phase during which clathrin and adapter components arrive at the membrane, and a highly regular late phase during which Wiskott Aldrich Syndrome Protein (WASP) and actin-associated proteins act at the endocytic site (Pedersen *et al.*, 2020). Recruitment of Saccharomyces cerevisiae WASP (Las17, referred to hereafter as scWASP) to a threshold level promotes a burst of actin assembly through activation of the Arp2/3 complex, which nucleates actin polymerization (Sun *et al.*, 2017). scWASP-mediated actin assembly is required to overcome the high turgor pressure of the yeast cell and drive membrane invagination (Soheil Aghamohammadzadeh and Ayscough, 2009).

With over 60 proteins involved in yeast endocytosis, many with nonessential roles or additional non-endocytic cellular functions, determining the functions of each protein in vivo has been challenging (Lewellyn *et al.*, 2015; Bhave *et al.*, 2020). CME robustness often thwarts attempts at function elucidation; simultaneous deletion of seven genes encoding early endocytic proteins was shown to only minimally impact endocytosis (Brach *et al.*, 2014). In vivo studies are well suited to identify necessary components of the CME machinery, but to identify components that are sufficient for CME and to gain insights into their biochemical mechanisms, we sought to reconstitute endocytic events in vitro. Biochemical reconstitution of cellular processes provides otherwise unattainable insight into fundamental molecular mechanisms (Liu and Fletcher, 2009). Reconstitution assays have been irreplaceable to test models and reveal mechanistic details for processes from pathogen motility in infected host cells (Loisel *et al.*, 1999; Brieher, Coughlin and Mitchison, 2004; Akin and Mullins, 2008) to mitotic spindle formation (Heald *et al.*, 1996; Gaetz *et al.*, 2006). Of relevance to the work reported here, many important advances in our understanding of vesicle fusion and fission have come through in vitro reconstitutions (Spang and Schekman, 1998; Weber *et al.*, 1998; Pucadyil and Schmid, 2008; Wu *et al.*, 2010). A reconstituted system for actin-mediated CME promises to reveal principles for properly ordered recruitment of CME proteins and the mechanics of membrane vesicle formation.

Here, we developed an in vitro assay that faithfully replicates the cooperative assembly of endocytic proteins onto synthetic membranes and deformation of the membrane into a nascent vesicle, resulting in actin-driven vesicle formation and release. As a conceptual complement to the modeling predictions from the previous chapter, we demonstrate that scWASP-templated actin and endocytic protein network assembly alone are sufficient to direct membrane deformation and vesiculation from lipid bilayers. We suggest that WASP-mediated actin network assembly represents a minimal system to drive membrane invagination and vesicle scission and may represent an early evolutionary precursor for a wide variety of membrane trafficking modalities.

3.2 Results and discussion

An in vitro actin assembly assay using polystyrene microbeads functionalized with scWASP was developed previously (Michelot *et al.*, 2010). When incubated in yeast cell extract, scWASP-coated beads assembled actin and selectively recruited endocytic actin network proteins. A fraction of the beads became motile. While this earlier reconstitution study represented an important advance for understanding the cooperative assembly of actin and actin-binding proteins involved in endocytosis, it did not allow conclusions to be drawn about the effect of the membrane on assembly of the actin network, or of actin network assembly on the membrane. To examine the effects of endocytic protein assembly on membranes we modified this system to include lipid bilayers (Figure 3.1A). To that end, supported lipid bilayers were made on solid microspheres using established protocols that retain bilayer fluidity (Figure 3.2A).

Cytoplasmic extracts were prepared from yeast strains expressing at endogenous levels endocytic proteins tagged with fluorescent proteins (Table 3.1). Since actin network nucleation on supported lipid bilayers was not observed in the absence of purified scWASP, this protein was purified and applied to the bilayers (Figure 3.1B–D). scWASP is one of the first actin regulators recruited to the endocytic site. Relative to proteins recruited to endocytic sites early in CME, scWASP arrival represents a more temporally regular progression from actin assembly to vesicle scission and internalization, thus making it a logical choice for this assay. Purified scWASP, previously shown to activate the Arp2/3 complex in vitro (Rodal *et al.*, 2003; Sun, Martin and Drubin, 2006), was efficiently recruited to supported lipid bilayers (Figure 3.1C). Although we engineered in a His-tag to bind scWASP to the Ni NTA supported lipid bilayers, we subsequently found that this tag was not necessary for binding. Presumably, in the absence of purified scWASP on the supported lipid bilayers the critical scWASP concentration required for actin network nucleation is not attained (Sun *et al.*, 2017).
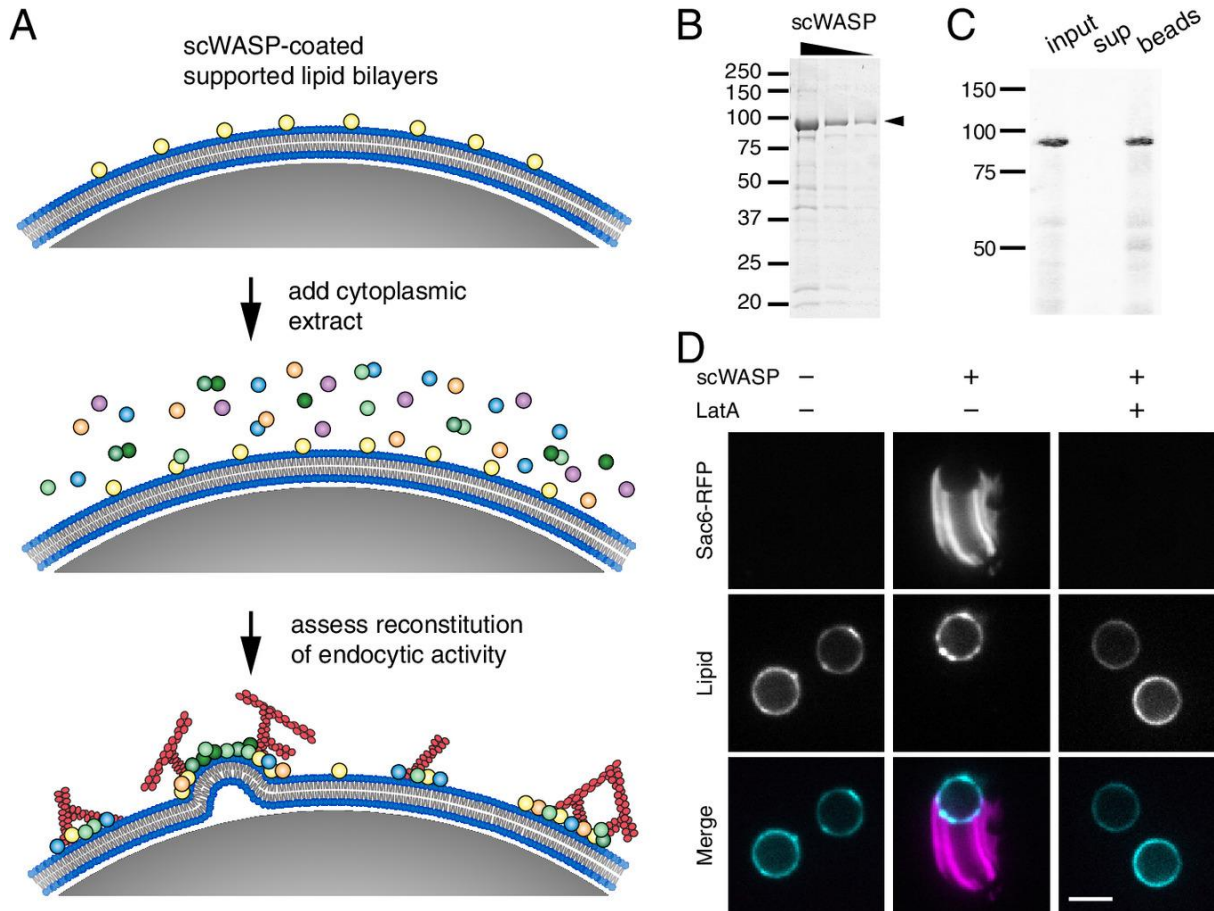
Figure 3.1 Reconstitution of endocytic actin networks on supported lipid bilayers. (A) Schematic representation of the in vitro reconstitution assay. Purified scWASP (Las17) is attached to supported lipid bilayers, which are then incubated in yeast cytoplasmic extract, resulting in the assembly of endocytic actin networks. (B) GelCode-stained SDS-PAGE gel of purified scWASP (arrowhead). (C) Purified scWASP binds to supported lipid bilayers, as shown by western blot probed with an anti-Las17 antibody. (D) Sac6-RFP from yeast cytoplasmic extract labels actin networks assembled on scWASP-coated supported lipid bilayers (Atto647-DOPE, lipid). 180 µM latrunculin A (LatA) inhibits actin assembly on bilayers (Scale bar, 5 µm.).

3.2.1 Reconstitution of Endocytic Actin Networks on Lipid Bilayers in Yeast Extract

scWASP-coated bilayers were incubated in freshly generated cytoplasmic extract and were then imaged. As previously observed with microbeads lacking a membrane bilayer, scWASP-coated supported lipid bilayers accumulated dense actin networks and associated actin-binding proteins (Figure 3.1D). Membrane-associated filamentous actin was detected using GFP-tagged Sac6 (yeast fimbrin, an actin-binding protein, Figure 3.1D) and fluorescent phalloidin, a small molecule that binds to filamentous actin (Figure 3.2B). Approximately 30% of beads broke symmetry and became motile, forming an actin tail behind the lipid-coated bead. Tail length was variable from bead to bead and between replicates and is likely related to the timing of stochastic symmetry breaking events. Actin assembly on bilayers was dependent on

the presence of scWASP (Figure 3.1D). Addition of the actin monomer sequestering drug latrunculin A (LatA) to reactions prohibited actin tail assembly and bead motility.

Previous work demonstrated roles for anionic lipid species in CME site initiation and invagination, including phosphatidylserine (PS) and phosphatidylinositol 4,5 bisphosphate (PI(4,5)P2) (Sun and Drubin, 2012). Varying the lipid composition to include PS and/or PI(4,5)P2 at concentrations used in previous bilayer reconstitution systems (Pucadyil and Schmid, 2008; Zhao *et al.*, 2013; Schroer *et al.*, 2020; Day *et al.*, 2021) did not result in a pronounced effect on actin assembly on the beads, as measured by quantifying the percentage of beads that accumulated a Sac6 signal (Figure 3.2C and D).

A pre-bleach · 0 s · 7.8 s · 15.6 s

B phalloidin-488 · Sac6-RFP · composite

(+) scWASP

(−) scWASP

C
- Sac6 accumulation
- No accumulation

Percent beads

PS   − + − +
PI(4,5)P$_2$ − − + +

D
PS   − + − +
PI(4,5)P$_2$ − − + +

(+) scWASP

(−) scWASP

37
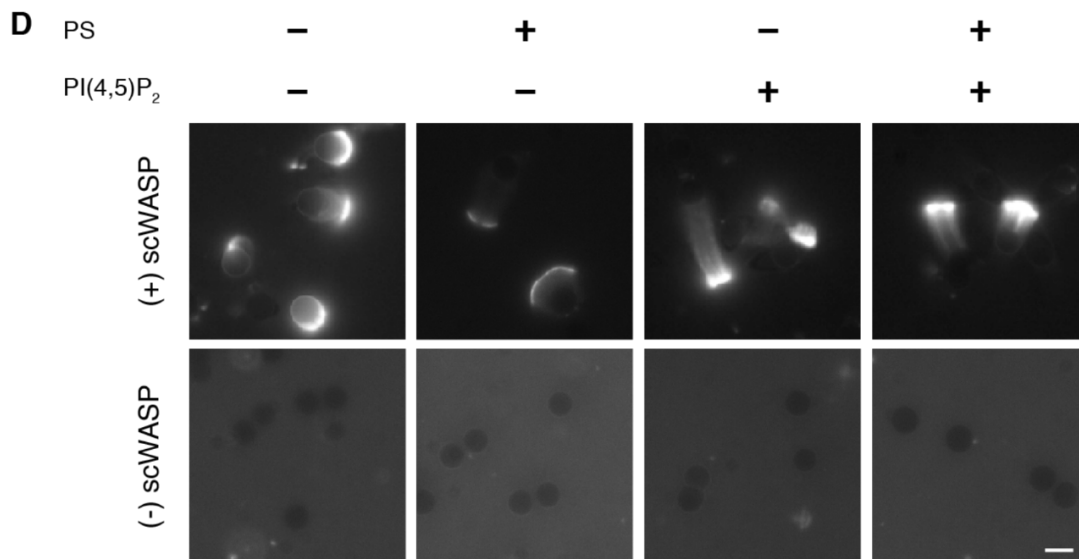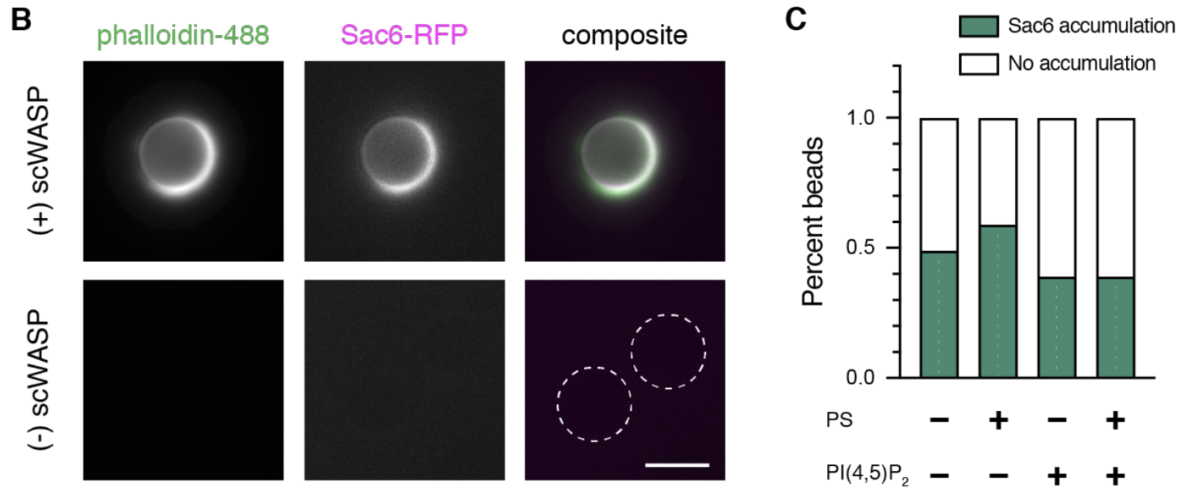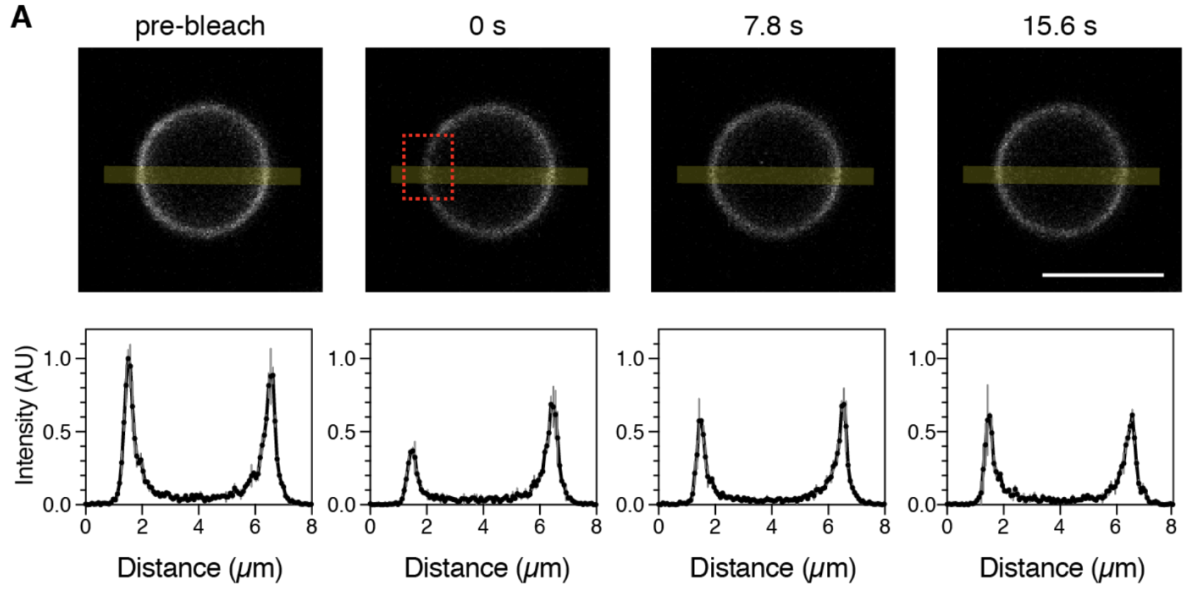
Figure 3.2 Characterization of lipids in reconstitution assay. (A) Fluorescence recovery after photobleaching experiment of supported lipid bilayers containing 0.05% TexasRed-DHPE. Time-lapse confocal images and the corresponding fluorescence intensity of a line (yellow line) drawn through the bleaching region (red box) demonstrate rapid lipid turnover. (B) Phalloidin-488 (26.4µM) was added to scWASP-coated or uncoated bilayers during incubation with cytoplasmic extract containing Sac6-RFP. Dotted lines outline the location of the beads lacking scWASP. (C and D) Sac6-GFP from yeast cytoplasmic extract labels actin networks assembled on scWASP-coated supported bilayers. Bilayer composition included 20% PS and/or 5% PI(4,5)P2 as indicated. (C) Quantification of the percentage of beads with associated Sac6 fluorescence. At least 160 beads per sample were quantified. (D) Representative images of Sac6-GFP accumulation on bilayers. Scale bars, 5 µm.

3.2.2 scWASP-Coated Bilayers Assemble the Machinery That Carries Out CME Internalization

To assess how faithfully the reconstitution system recapitulated in vivo CME events, we determined whether proteins downstream of scWASP in the endocytic pathway were recruited to the bilayers (Figure 3.3A). We used extracts from yeast strains expressing a GFP-tagged protein of interest and Sac6-RFP to allow endocytic proteins to be located relative to the actin network.

A

Initiation Coat formation WASP recruitment Invagination Scission Release

Module **Example Proteins**

- early proteins — Ede1, Syp1
- coat module — clathrin, Sla2
- WASP/myosin module — scWASP, Myo3/5, Bzz1, Vrp1, Bbc1
- actin module — actin, Sac6, Abp140, Ark1
- scission module — Rvs161/167

B

GFP Sac6-RFP Merge

Bzz1-GFP

Vrp1-GFP

Myo5-GFP

GFP Sac6-RFP Merge

Bbc1-GFP

Ark1-GFP

Rvs167-GFP

C

Rvs167

Myo5 Bzz1

Abp140

Ark1

Sac6

D

Incubation time (minutes:seconds)

81:19 90:32 99:45 108:57 118:10 127:23 136:36 145:49

Merge

Sac6-RFP

Bzz1-GFP

39

Figure 3.3 scWASP-coated bilayers sequentially recruit downstream endocytic proteins. (A) Schematic representation of CME in S. cerevisiae. The schematic depiction is not drawn to scale. (B) Protein localization on scWASP-coated supported bilayers. Extracts were prepared from strains expressing Sac6-RFP and the indicated endocytic proteins tagged with GFP. Representative fluorescence images from three independent experiments are shown. (Scale bar, 10 μm.) (C) Localization of endocytic proteins on su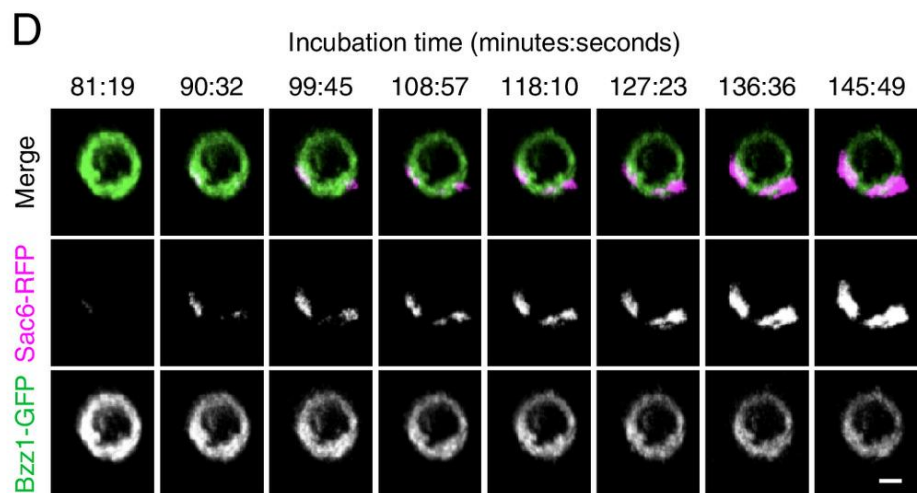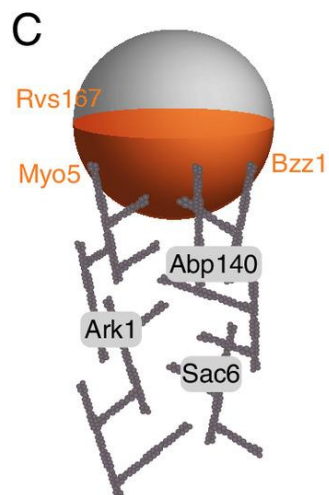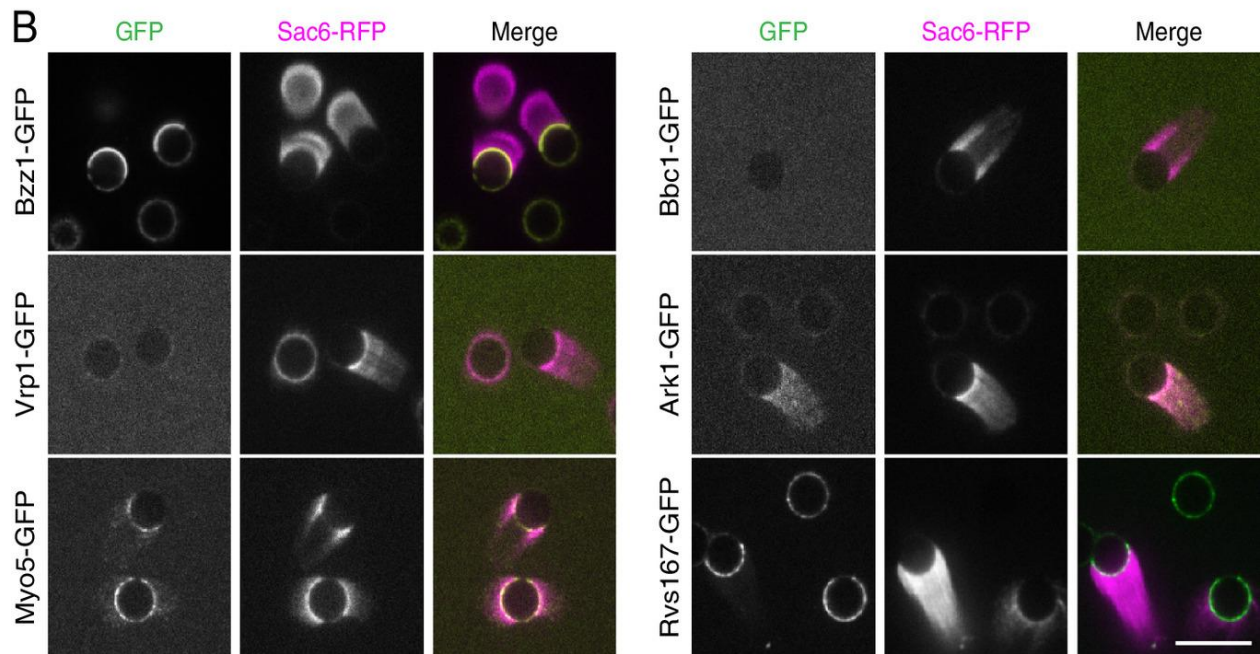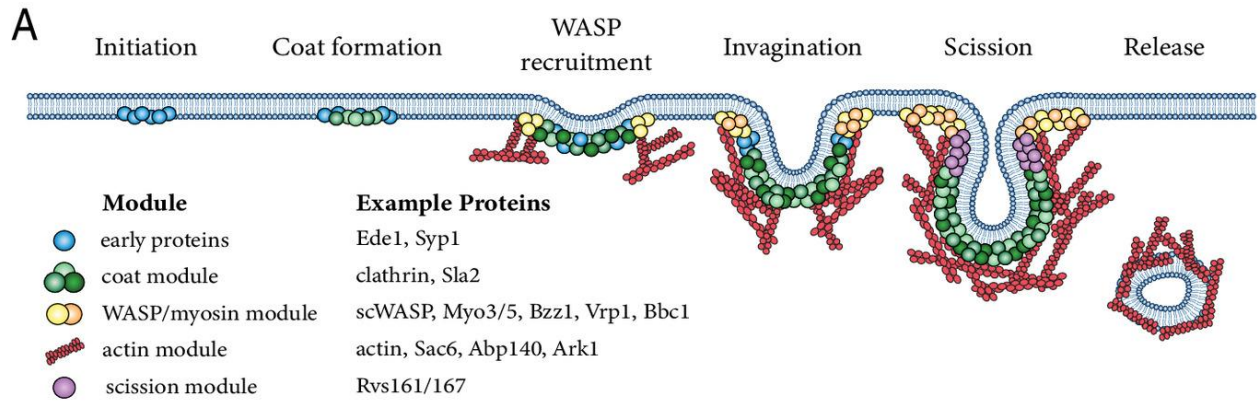pported lipid bilayers and associated actin networks is represented in cartoon view. Bzz1, Rvs167, and Myo5 were observed primarily on lipid bilayers in the region of actin assembly. Ark1, Sac6, and Abp140 were associated with the actin network. (D) scWASP-coated beads were incubated in cytoplasmic extract from strains expressing Bzz1-GFP and Sac6-RFP. Representative montage of 3D rendered images from time-lapse confocal microscopy. Indicated time points (minutes:seconds) are relative to the moment cytoplasmic extract was added to beads (Scale bar, 2 μm.).

Myo3 and Myo5 are type I myosins that facilitate endocytic actin assembly through their motor and NPF (nucleation-promoting factor) activities (Geli and Riezman, 1996; Manenschijn *et al.*, 2019; Pedersen and Drubin, 2019). They are required for endocytic vesicle internalization (Geli and Riezman, 1996; Sun, Martin and Drubin, 2006; Goodson *et al.*, 1996; Kaksonen, Toret and Drubin, 2005). Myo5-GFP was localized primarily to the bilayers in areas of actin assembly, with trace amounts of Myo5-GFP also localizing to actin tails (Figure 3.3B). These data are consistent with previous results on scWASP-coated microbeads (Michelot *et al.*, 2010) and with previous data showing that type I myosin does not leave the cell surface during vesicle internalization (Jonsdottir and Li, 2004). Bzz1 was also recruited to bilayers in an scWASP-dependent manner (Figure 3.3B and Figure 3.4A). Bzz1 is an scWASP-binding protein that relieves scWASP inhibition to promote actin assembly initiation (Soulard *et al.*, 2002; Sun, Martin and Drubin, 2006). On lipid bilayers with actin tails, Bzz1-GFP localized to the hemisphere of the lipid bilayer from which the actin tail protrudes. In contrast, Vrp1 [Wasp Interacting Protein (WIP)], which interacts directly with scWASP and Myo3/5 (Sun, Martin and Drubin, 2006), was not observed or was only weakly observed on bilayers or associated with actin tails. Similarly, Bbc1 was not recruited to bilayers or actin tails under these conditions. Bbc1 is known to inhibit scWASP in later stages of endocytosis and to thereby control the speed and extent of inward vesicle movement (Kaksonen, Toret and Drubin, 2005; Sun, Martin and Drubin, 2006). Bbc1 absence from actin tails might reflect incomplete reconstitution of regulatory components. Following scWASP activation, there is a burst of actin assembly and recruitment of actin-associated proteins. As observed for Sac6-GFP, actin-binding protein Abp140-GFP was recruited to actin tails (Figure 3.4B). Additionally, the endocytic regulatory serine/threonine protein kinase Ark1 was observed in actin tails protruding from scWASP-coated lipid bilayers (Figure 3.3B).
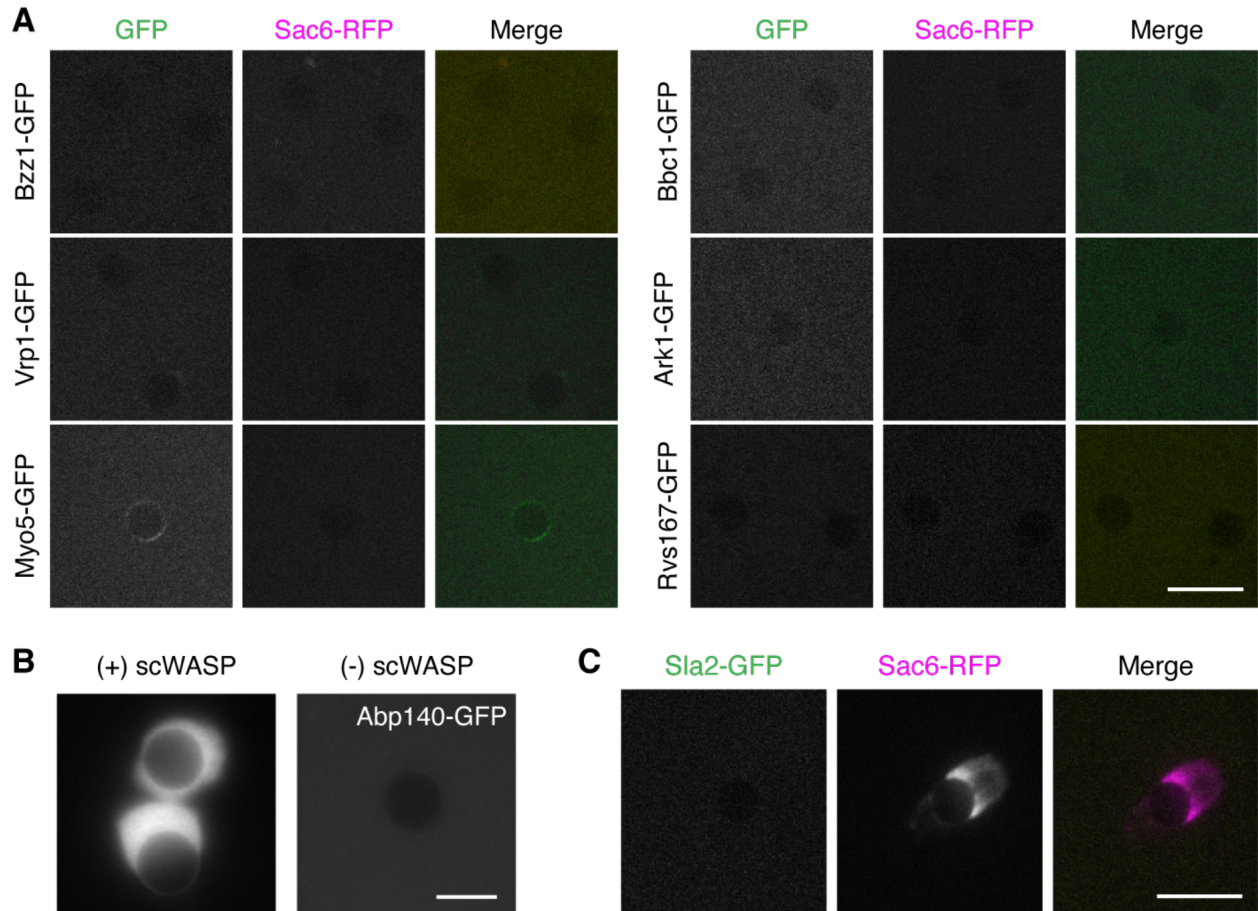
Figure 3.4 Recruitment of additional CME proteins. (A) Endocytic proteins do not localize to bilayers in the absence of scWASP. Extracts were prepared from strains expressing Sac6-RFP and the indicated endocytic proteins tagged with GFP, as in Figure 2B. Scale bar, 10 μm. (B) Abp140-GFP is recruited to actin networks. scWASP-coated and uncoated bilayers were incubated in cytoplasmic extract generated from a strain expressing Abp140-GFP. Scale bar, 5 μm. (C) Coat protein Sla2 does not localize to scWASP-coated bilayers. Bilayers were incubated in cytoplasmic extract generated from a strain expressing Sla2-GFP and Sac6-RFP. Scale bar, 10 μm. Representative fluorescence images from 3 independent experiments are shown.

Further downstream of scWASP, heterodimeric N-BAR proteins Rvs161 and Rvs167 (yeast homologues of amphiphysin) contribute to vesicle scission and have been shown to tubulate membranes in vitro (Kaksonen, Toret and Drubin, 2005; Youn *et al.*, 2010). Observations in electron micrographs show that Rvs161/Rvs167 is concentrated at the bud neck of deeply invaginated clathrin-coated pits (Idrissi *et al.*, 2008; Picco *et al.*, 2015). In our assay, Rvs167-GFP was recruited to scWASP-coated bilayers and was concentrated in the area of actin network formation, where it formed punctae (Figure 3.3B).

We also analyzed whether proteins upstream of scWASP are recruited to the membranes. Sla2 links coat proteins to the actin cytoskeleton in vivo. However, it was not visible on scWASP-coated bilayers (Figure 3.4C).

These data are summarized in a cartoon schematic showing where each endocytic protein localizes on the scWASP-coated lipid bilayers (Figure 3.3C). Our

results are like those obtained previously with nonlipid-coated beads (Michelot *et al.*, 2010). The recruitment of multiple actin-binding proteins, nucleation-promoting factors, and actin regulatory components to the bilayers or actin tails, or both, indicates that our reconstituted system recapitulates self-assembly of the endocytic actin network. Furthermore, Rvs167 presence indicates recruitment of at least some of the machinery required to induce vesicle scission.

3.2.3 Protein Recruitment Order In Vitro Recapitulates CME Temporal Dynamics In Vivo

As a test of whether the correct CME protein recruitment order is encoded in the proteins themselves, we assessed whether this sequence is recapitulated in the reconstituted system. The in vivo recruitment of proteins to endocytic sites follows a regular order that is highly conserved across species (Kaksonen, Sun and Drubin, 2003; Pedersen *et al.*, 2020; Kaksonen, Toret and Drubin, 2006; Lu, Drubin and Sun, 2016) (Figure 3.3A). To determine whether CME proteins accumulate on lipid bilayers in the correct physiological sequence, we observed reconstituted endocytic protein complexes as they formed in a flow chamber overtime. Figure 3.3D shows time-lapse data from scWASP-coated beads after addition of cytoplasmic extract prepared from cells expressing Bzz1-GFP and Sac6-RFP. In cells, Bzz1 is present at the endocytic site immediately prior to the start of actin assembly (Soulard *et al.*, 2002; Sun, Martin and Drubin, 2006). Our in vitro data recapitulate this sequence with Bzz1 appearing on beads before Sac6 (Figure 3.3D). Additionally, Bzz1 recruitment is scWASP-dependent (Figure 3.4A), indicating that the established sequence from scWASP to the regulatory factor (Bzz1) to actin assembly is preserved. Interestingly, Bzz1 localization on the bead is polarized prior to actin assembly, which then initiates from areas of high Bzz1 density.

These data demonstrate successful recapitulation of sequential endocytic protein assembly and establish that spatiotemporal recruitment is an intrinsic property of at least some endocytic proteins. It should be noted that while the recruitment order is preserved in vitro, the kinetics of recruitment do not replicate in vivo kinetics. In live cells, Bzz1 and Sac6 have lifetimes of approximately 15 to 17 and 11 to 15 s at the endocytic site, respectively (Kaksonen, Toret and Drubin, 2005; Sun, Martin and Drubin, 2006; Pedersen *et al.*, 2020). On supported lipid bilayers, Bzz1 is recruited to bilayers within seconds of extract addition, but there is a delay of up to 90 min prior to Sac6 arrival. The variance in length of time between recruitment events in the cytosolic extract versus the native yeast cytosolic environment could reflect differences in the protein concentrations and energy conditions, or differences between length scales for in vivo endocytic events, which are on the nanometer scale, versus in vitro length scales for actin tails on the order of microns.

3.2.4 Vesicles Are Released from Sites of Endocytic Actin Network Assembly

The supported lipid bilayer system described above reconstitutes actin-generated pushing forces on the micron scale, as demonstrated by bead motility.

We next set out to determine whether these components could also drive nano-scale vesicle formation. In experiments similar to those described above to test for sequential CME protein recruitment, we next used a small amount of Atto647-DOPE as a marker of the lipid bilayer. The micrographs revealed tubules and smaller lipid protuberances in regions where endocytic proteins and actin assembled on the bilayers (Figure 3.5A and B). In addition to tubulation, we often observed in static confocal micrographs small (diffraction-limited) lipid structures embedded in, or in the vicinity of, actin tails, which we hypothesized to be vesicles released from the supported-lipid bilayer. To determine whether these putative vesicles form by being pinched off from supported lipid bilayers, real-time imaging was performed. First, we systematically tested the effect of PS and PI(4,5)P2 in lipid bilayers on vesicle accumulation in our assay. Addition of 5% PI(4,5)P2 to our standard lipid mixture produced the highest frequency of actin-associated vesicles (Table 3.2). In 37 time-lapse videos collected from four independent experiments, we observed spherical lipid structures breaking free from the lipid bilayer concurrent with a burst of actin polymerization at the same site (Figure 3.6A and Figure 3.7A). The number of vesicles observed per bead (0.248 ± 0.291) was reduced dramatically by removing either scWASP (0.0476 ± 0.0638) or by treating reactions with LatA (0.0481 ± 0.0638); no vesicles were observed in the absence of cytoplasmic extract (Table 3.3). To quantitatively analyze the dynamics of these vesiculation events and compare them to in vivo CME, we tracked vesicle formation and movement in 3D and measured fluorescence intensities and displacement over time (Figure 3.6B and Figure 3.7B). Each vesicle track was temporally aligned at the displacement inflection point calculated using previously described techniques (Figure 3.8) (Sun *et al.*, 2019). This alignment revealed a highly reproducible burst of actin assembly beginning approximately 15 min before the vesicle buds off from the bead (Figure 3.6C). Bzz1 stays at the plasma membrane and is not observed to associate with the departing vesicle, consistent with previous data showing Bzz1's role in vesicle scission at the invagination base (Sun, Martin and Drubin, 2006; Idrissi *et al.*, 2008; Kishimoto *et al.*, 2011). The actin network continues to grow and propel the vesicle from the bead about 2 μm on average over about 10 min (Figure 3.6C). This time scale is significantly longer than is seen in yeast, where the time from onset of actin assembly to vesicle scission is approximately 10 s. It is possible that ultracentrifugation and dilution of the cytoplasmic extract alter its composition sufficiently to affect reaction kinetics, or that the coupling between the membrane and actin is weak in the absence of Sla2. Alternatively, the assay may be reconstituting friction-mediated scission (Simunovic *et al.*, 2017) in a system with less friction than in the native plasma membrane. Despite the difference in time scale, the sequence from scWASP to Bzz1 recruitment to actin assembly (as visualized by Sac6) to membrane pulling follows the order observed for endocytic events in vivo.
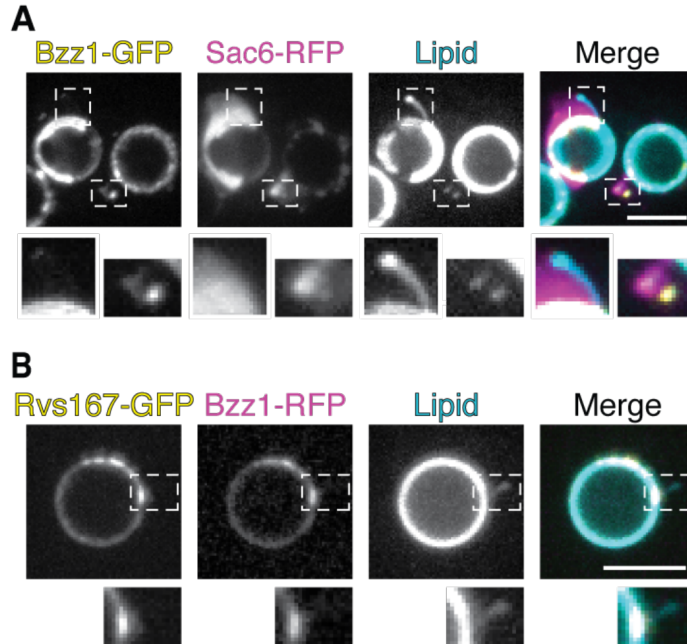
Figure 3.5 Membrane tubulation. (A and B) scWASP-coated bilayers were incubated in cytoplasmic extract from strains expressing the indicated GFP- and RFP-tagged proteins. Maximum intensity projections of confocal stacks through the midsection of scWASP-coated bilayers containing lipid dye (0.5% MarinaBlue- DHPE) are displayed. Scale bars, 5 μm. (A) Insets show regions of an actin tail where membrane tubulation and membrane deformation occurred (lipid channel). (B) Inset shows membrane tubulation (lipid channel) at plaques of Rvs167-GFP and Bzz1-RFP accumulation.
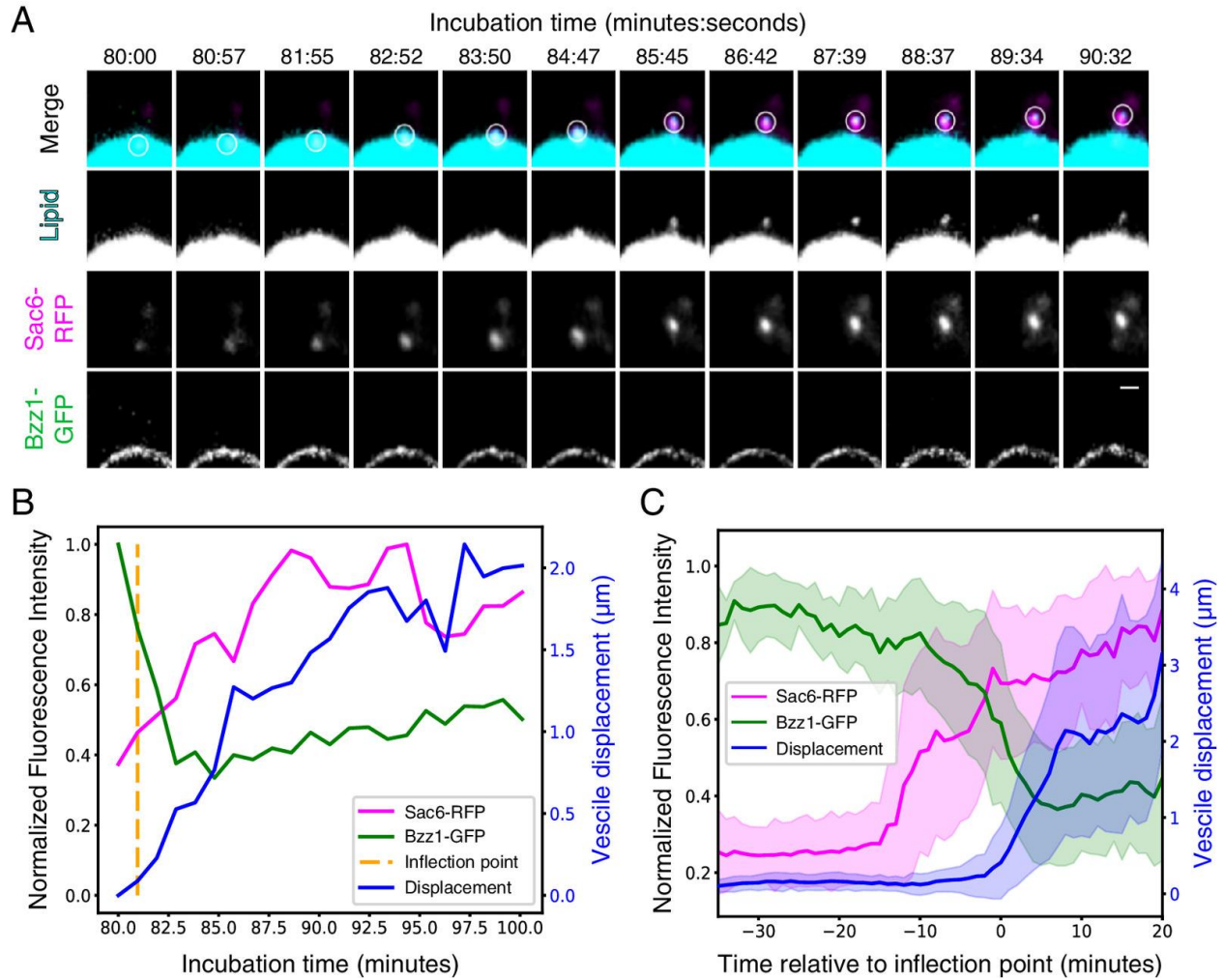
Figure 3.6 Reconstitution of actin-mediated vesicle budding. Supported lipid bilayers were coated with scWASP and incubated in Bzz1-GFP Sac6-RFP cytoplasmic extracts for the indicated times. (A) Montage of a single vesiculation event. A maximum intensity projection 2 µm in depth is displayed for all channels. Bilayers include 2% Atto647-DOPE (cyan) to allow visualization of lipid. The white circle in the merged channel row indicates the region used for quantitative analysis. (Scale bar, 1 µm.) (B) Quantification trace of fluorescence intensities inside the white circle and vesicle displacement from the vesiculation event visualized in (A). The algorithmically determined inflection point is indicated by the vertical dotted line. (C) Mean fluorescence intensities and vesicle displacement with SD from all measured vesiculation events (n = 37). All traces were aligned in time by their respective inflection points prior to taking the mean and SD.
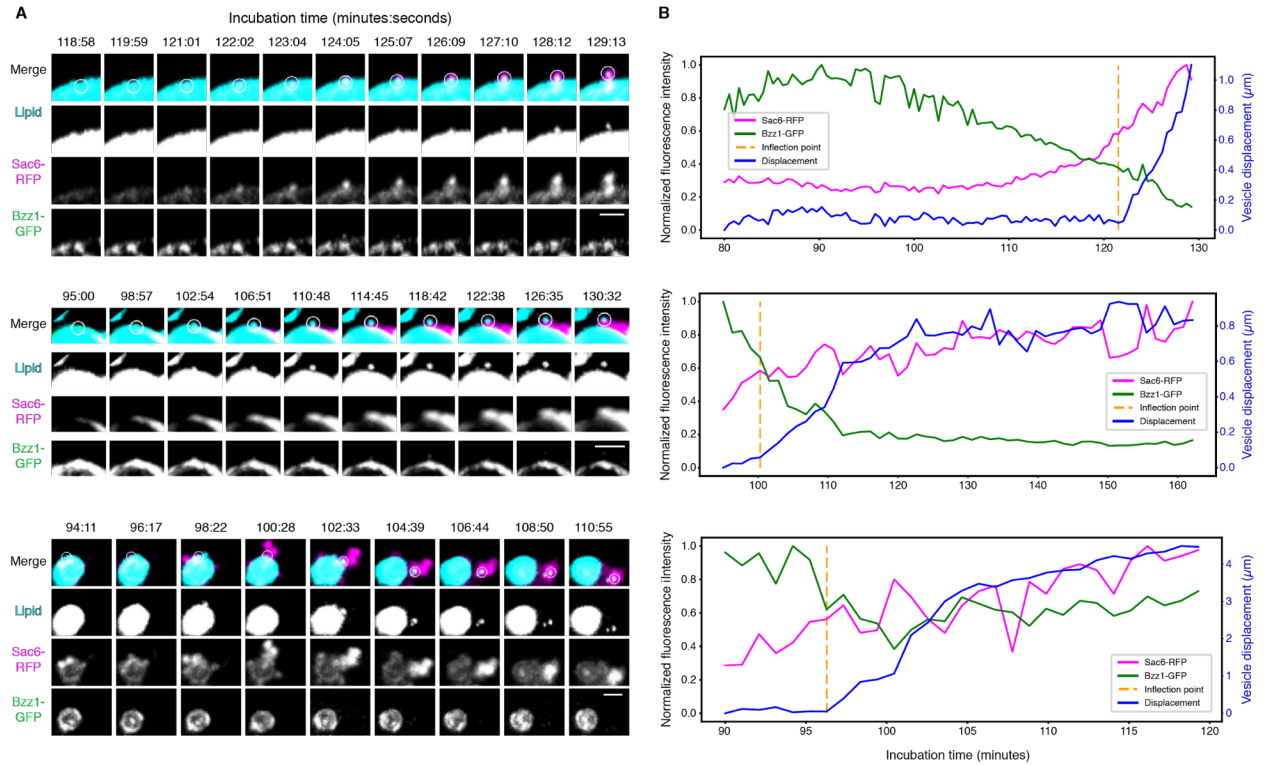
Figure 3.7 Additional examples of reconstituted vesicle budding. scWASP-coated supported lipid bilayers (with 2% Atto647-DOPE) were incubated in Bzz1-GFP Sac6-RFP cytoplasmic extract for the indicated times. (A) Montages of vesiculation events on 5 µm (upper two panels) and 2 µm (lower panel) beads. A maximum intensity projection of a substack through the center of the supported lipid bilayer is displayed for all channels. The white circle in the merged channel indicates the region used for quantitative analysis. Scale bars, 2 µm. (B) Quantification traces of fluorescence intensities and vesicle displacement from the vesiculation events visualized in (A).
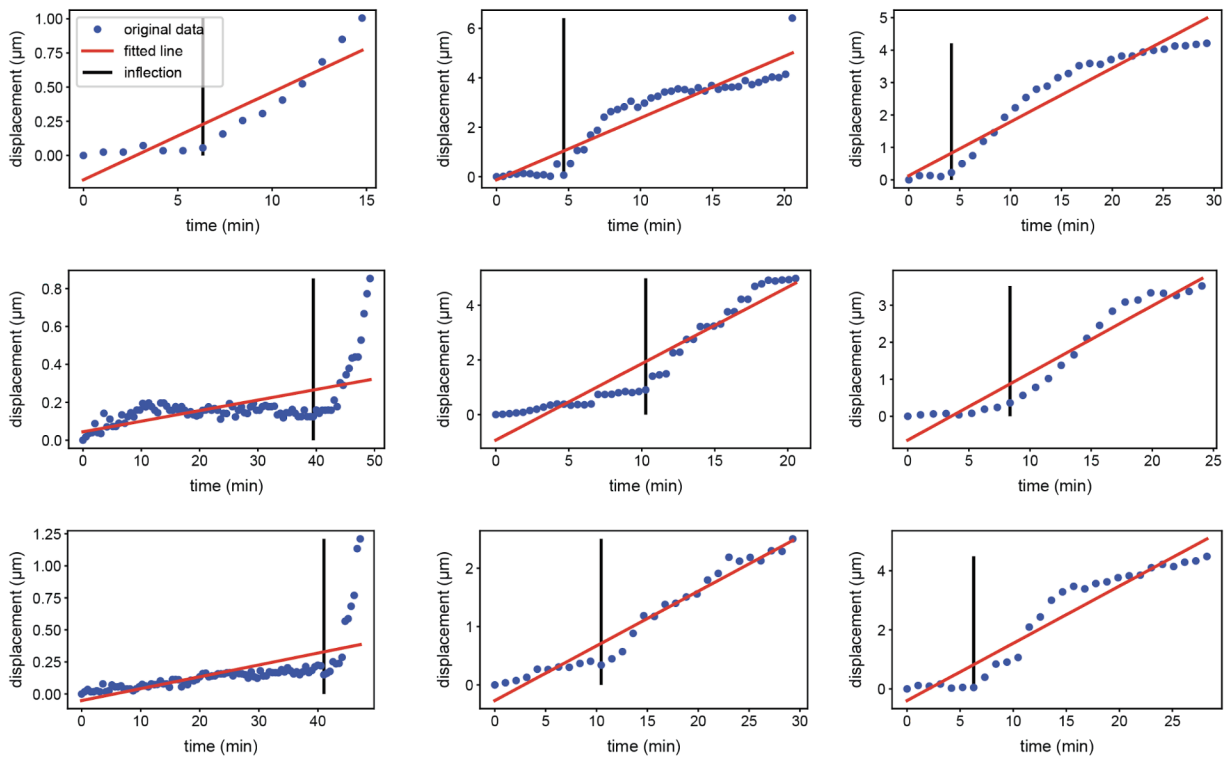
Figure 3.8 Gallery of randomly selected individual vesiculation event traces used for inflection point calculations. Blue dots represent the vesicle displacement in 3D volume from the origin position at the beginning of the event. A linear regression was fit to each vesiculation event trace. The inflection point was then determined as the time point at which the vesicle displacement was the maximum negative difference from the linear regression, out of all the time points before the point at the maximum positive difference from the linear regression. The constraint for points before the maximum positive difference from the linear regression was necessary to filter out points in displacement traces that plateaued at later time points.

Given that endocytic events typically occur on a length scale that is below the diffraction limit of our fluorescence microscopy system, we employed correlative light and electron microscopy (CLEM) to achieve the necessary resolution to directly observe deformed membranes and free vesicles. We used beads 2 μm in diameter (versus 5 μm in previous experiments) to improve the beads' spatial stability during sample processing for CLEM. Vesiculation events occurred on both size beads at similar rates (Figure 3.7). Transmission electron micrographs of lipid bilayers on beads in yeast extract revealed formation of scWASP-dependent membrane structures on the length scale of biological endocytic events (~50 to 100 nm, Figure 3.9A and Figure 3.10A–B). A variety of membrane profiles were observed, including apparent tubules contiguous with the bead surface and vesicles some distance away from the bead (Figure 3.9A and Figure 3.10). Corresponding light micrograph images demonstrated actin assembly around the beads (Figure 3.9A, Sac6-GFP signal). To assess whether membrane deformation requires actin assembly, we sampled bilayers treated with LatA and observed a pronounced reduction in free vesicles, but an increase in small tubules and deformations at the membrane surface (Figure 3.9B). Fewer free vesicles and

membrane deformations were observed in samples lacking scWASP (Figure 3.9C) and these features were entirely absent in samples lacking cytoplasmic extract (Figure 3.9D). We lack 3D information in these TEM micrographs to allow us to determine whether the membrane structures are contiguous with the supported lipid bilayer. However, we have observed that vesicles move away from the beads in time-lapse imaging. Therefore, as a proxy for whether they are contiguous with the membrane or are distinct structures, we classified vesicles observed in EM by their distance from the bead surface (Figure 3.9E and Table 3.4). We observed an approximately 15-fold increase in the frequency of membrane structures between 100 and 1,000 nm from the surface of scWASP-coated beads compared to the surface of beads lacking scWASP. Membranes observed in this region are likely vesicles derived from the supported lipid bilayer on the bead surface. Similar to our quantification of the time-lapse imaging data (Table 3.3), more budding events were observed in reactions containing scWASP and extract in the absence of LatA. Of note, scWASP-containing beads treated with LatA to inhibit actin polymerization showed the highest frequency of membrane structures within 100 nm of the bead surface. These structures are likely invaginations of the bead supported lipid bilayer. Interestingly, the curvature-generating protein Bzz1 is recruited to supported lipid bilayers in a scWASP-dependent manner, independent of LatA treatment (Figure 3.10C). These data are consistent with a role for curvature generating proteins in early stages of membrane invagination and a known role for actin in driving membrane internalization and scission in yeast.
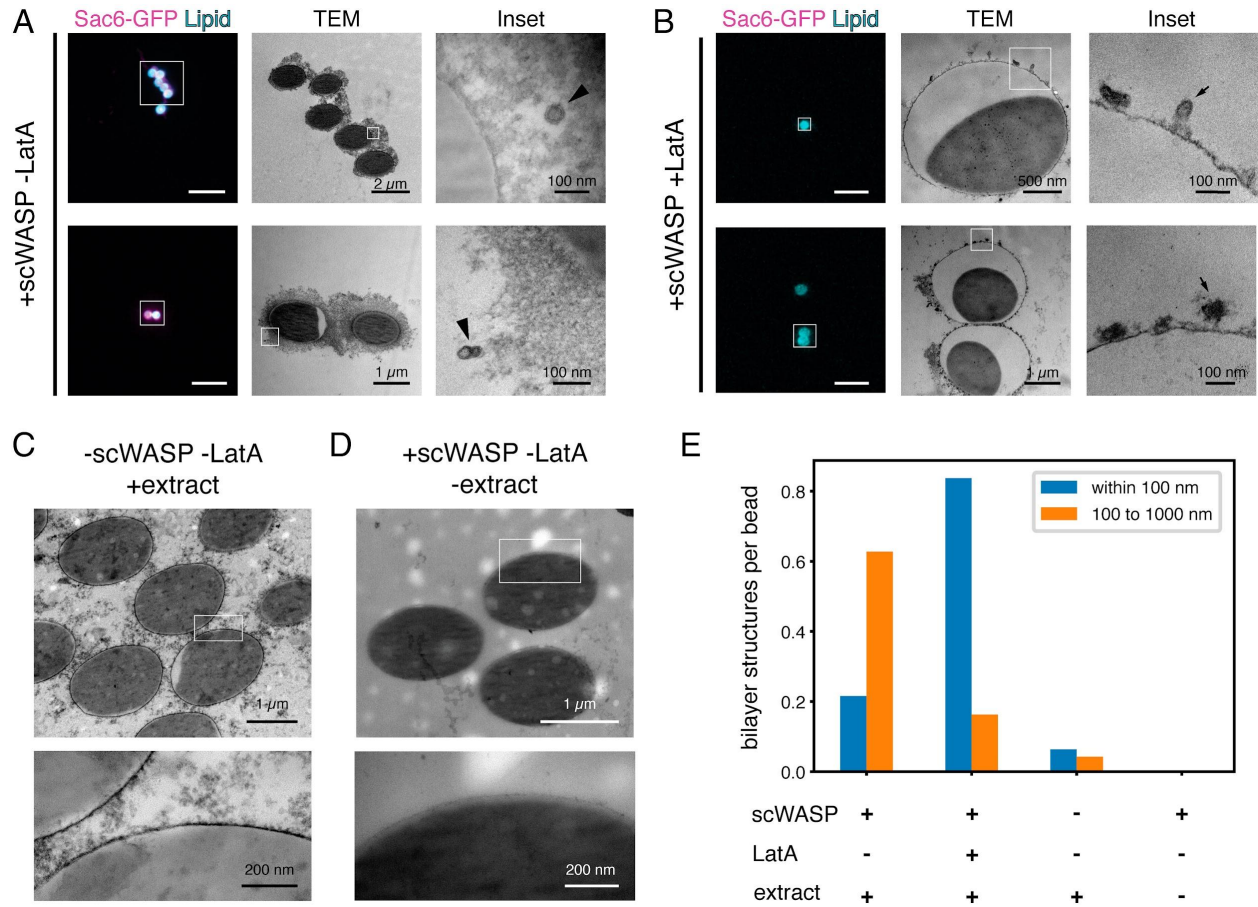
Figure 3.9 Self-assembled endocytic actin networks deform lipid bilayers. (A and B) Representative CLEM images of scWASP-coated supported lipid bilayers incubated in extracts containing Sac6-GFP in the (A) presence or (B) absence of LatA. Bilayers include 2% Atto647-DOPE (cyan) to allow visualization of lipid. Left subpanels show light microscopy (Scale bar, 10 µm.). Middle and Right subpanels show transmission EM images of the regions indicated by white boxes. (C and D) Representative electron micrographs of supported bilayer reactions in the absence of (C) scWASP or (D) cytoplasmic extract. (E) Manual scoring of lipid bilayer tubules and vesicles in EM sections prepared from the indicated reaction conditions.

A

+scWASP +extract

B

-scWASP +extract

+scWASP +extract

+scWASP +extract +LatA

C

	Bzz1-GFP	Sac6-RFP	Lipid	Merge
-scWASP +extract				
+scWASP +extract				
+scWASP +extract +LatA				

Figure 3.10 Actin influences frequency of vesiculation events. (A) High magnification EM images of vesicles (arrowheads) observed around supported lipid bilayers coated with scWASP and incubated in cytoplasmic extract. Scale bar, 100 nm. (B) Supported lipid bilayers on microbeads were either coated with or not coated with scWASP and incubated in cytoplasmic extract with or without latrunculin A, as indicated. Representative EM images of membrane deformations observed for each condition are presented here. (C) scWASP-coated bilayers were incubated in cytoplasmic extract from a strain expressing Bzz1-GFP and Sac6-RFP. Single confocal slices at the midsection of scWASP-coated bilayers containing lipid dye (2% Atto647-DOPE) are displayed. Scale bar, 10 μm.

Table 3.1. Strains used in this study.

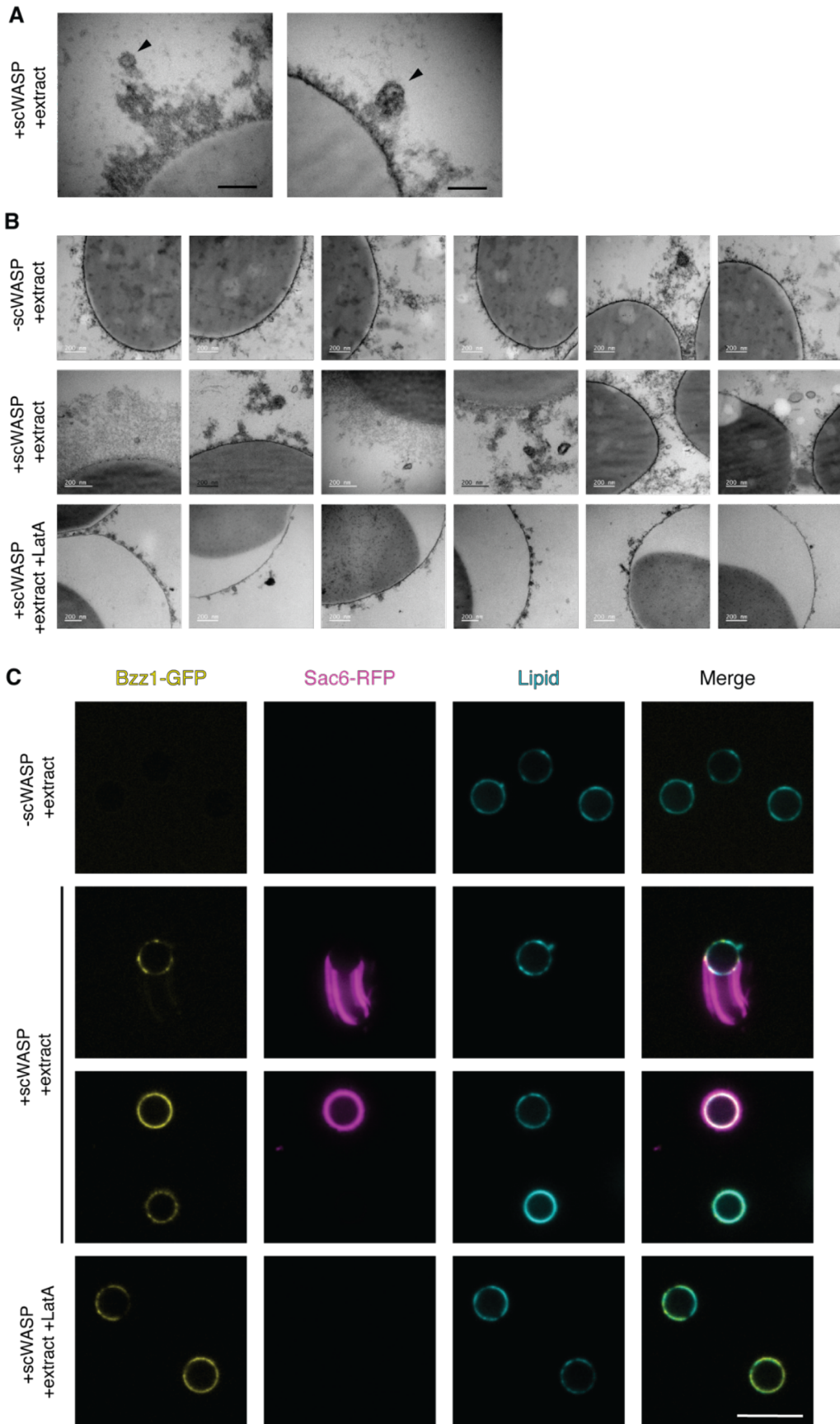| DDY Strain	Genotype	Source
DDY5783	MATa ade2 leu2 his3 trp1 ura3 lys2::Pgal1-GAL4 pep4::HIS3 bar1::hisG	(St-Pierre *et al.*, 2009)
DDY5784	MATa his3-Δ200, leu2-3, 112, ura3-52, SAC6-RFP::KANmx	This study
DDY5785	MATα his3-Δ200, leu2-3, 112, lys2-801 ura3-52, RVS167-GFP::HIS3 SAC6-RFP::KANmx	This study
DDY5786	MATa his3-Δ200, leu2-3, 112, ura3-52, MYO5-GFP::HIS3 SAC6-RFP::KANmx	This study
DDY5787	MATα his3-Δ200, leu2-3, 112, ura3-52, ARK1-GFP::KANmx SAC6-RFP::KANmx	This study
DDY5788	MATα his3-Δ200, leu2-3, 112, ura3-52, lys2-801, VRP1-GFP::HIS3 SAC6-RFP::KANmx	This study
DDY5789	MATα his3-Δ200, leu2-3, 112, ura3-52, BZZ1-GFP::HYGmx SAC6-RFP::KANmx	This study
DDY5790	MATα his3-Δ200, leu2-3, 112, ura3-52, lys2-801, BBC1-GFP::HIS3 SAC6-RFP::KANmx	This study
DDY4350	MATα his3-Δ200, leu2-3, 112, ura3-52, ABP140-3×GFP::HIS3	(Miao *et al.*, 2013)
DDY5791	MATα his3-Δ200, leu2-3, 112, ura3-52, SLA2-GFP::HIS3 SAC6-RFP::KANmx	This study
DDY2960	MATα his3-Δ200, leu2-3, 112 lys2-801, ura3-52, SAC6-GFP::HIS3	(Martin, Welch and Drubin, 2006)
DDY3937	MATα his3-Δ200, leu2-3, 112, ura3-52, BZZ1-GFP::HygMX, RVS167-RFP::HIS3	(Kishimoto *et al.*, 2011)

Table 3.2 Manual quantification of the occurrence of actin-associated lipid protrusions on bilayers of differing lipid compositions. Where indicated, 20% phosphatidylserine (PS) and/or 5% phosphatidylinositol 4,5 bisphosphate (PI(4,5)P2) were added to bilayers containing 5% DGS- NTA, 2% ATTO 647-DOPE, and phosphatidylcholine (PC) up to 100%.

Lipid composition	n beads	Beads with actin-associated vesiculation	Percent
PC	103	3	0.029
PC + PS	154	11	0.071
PC + PI(4,5)P2	100	20	0.200
PC + PS + PI(4,5)P2	115	22	0.191

Table 3.3 Quantification of vesicle budding events observed in time lapse imaging. For each condition listed, the number of fluorescent vesicles formed from the surface of supported lipid bilayers on beads (budding events) was manually counted over the course of 30- to 60-minute 3D time-lapse experiments. The number of budding events per experiment was divided by the number of beads and averaged among replicate experiments to calculate the mean and standard deviation budding events per bead.

Condition	n beads	Mean budding events per bead	Standard deviation
-scWASP -LatA +extract	49	0.0476	0.0825
+scWASP -LatA +extract	97	0.248	0.291
+scWASP +LatA +extract	188	0.0481	0.0638
+scWASP -LatA -extract	16	0	0

Table 3.4 Quantification of vesicles observed by EM. For each condition listed, the number of vesicles and membrane structures at given distances away from the bead surface was manually counted using 2D electron micrographs. Events were categorized as 'adjacent' if within 100 nm of the bead surface or 'nonadjacent' if between 100 nm and 1000 nm from the bead surface. Vesicles found greater than 1000 nm from a particular bead were not counted.

Condition	n beads	Adjacent events (lipid bilayers 10 - 100 nm from bead surface)	Adjacent events per bead	Nonadjacent events (lipid bilayers 100 - 1000 nm from bead surface)	Nonadjacent events per bead
-scWASP -LatA +extract	47	3	0.0638	2	0.0426
+scWASP -LatA +extract	51	11	0.216	32	0.627
+scWASP +LatA +extract	43	36	0.837	7	0.163
+scWASP -LatA -extract	16	0	0	0	0

3.3 Conclusion

This work demonstrates that endocytic proteins and the actin network intrinsically embody the information sufficient to self-organize into a force-producing system capable of deforming a lipid bilayer and producing a vesicle. This work builds off other in vitro models for actin force generation, including those for Listeria motility (Loisel *et al.*, 1999), filopodia formation (Liu *et al.*, 2008; Lee *et al.*, 2010) and actin-induced membrane phase separation (Liu and Fletcher, 2006). However, unlike previously reported systems, here actin is generating a pulling, not pushing, force. Moreover, time-lapse imaging revealed that the order of molecular events was faithfully reconstituted, and electron microscopy showed that these membrane remodeling events are on the size scale observed in yeast endocytosis.

Interestingly, vesicle generation in our reconstituted system occurs in the absence of certain upstream structural and regulatory factors including Sla2 and Bbc1. It is possible that other coat proteins that we did not attempt to localize in this study are recruited to the in vitro system. Our data are consistent with previous findings, which showed that many coat proteins and initiation factors are not necessary for endocytic vesicle formation. Endocytosis still occurs in clathrin null mutants, although the number of endocytic sites is reduced (Kaksonen, Toret and Drubin, 2005; Payne and Schekman, 1985; Chu, Pishvaee and Payne, 1996; Newpher and Lemmon, 2006). A previous study examined CME in yeast with null alleles of genes encoding seven initiation factors and coat proteins and determined that membrane bending and vesicle budding were largely unperturbed (Brach *et al.*, 2014). These observations are consistent with the existence of multiple endocytic pathways in various cell types that require actin but do not require clathrin or its associated coat proteins (Mayor and Pagano, 2007; Sandvig, Kavaliauskiene and Skotland, 2018). In light of these observations, we propose that a network of actin and associated proteins might constitute a primitive endocytic machinery that diversified through evolution to give rise to multiple vesicle-forming processes, with coat proteins and other accessory factors added later as evolutionary embellishments.

In the future, addition of cargo and proteins upstream of scWASP in the CME pathway to this in vitro reconstitution assay promises to provide valuable mechanistic insights into the roles of cargo, coat proteins, and other regulatory factors. We anticipate that coat proteins would be required to reconstitute selective cargo recruitment, as shown previously in yeast (Brach *et al.*, 2014). Additionally, the in vitro assay provides a system in which effects of differing lipid composition on CME can be analyzed without off-target effects that confound such studies in live cells.

This work establishes that vesicle pulling, and scission, are intrinsic to the ensemble activities of the endocytic actin network. Future work using this assay will allow us to elucidate the roles of individual proteins and lipid species in vesicle generation.

3.4 Materials and Methods

3.4.1 Strains

Cells were maintained at 25 or 30 °C on rich YPD media (Yeast extract/ Peptone/Dextrose). Yeast strains used in this study are listed in SI Appendix, Table S1. Genomic C-terminal tagging was performed as described previously (Longtine *et al.*, 1998).

3.4.2 Protein Purification

Yeast WASP (Las17) was cloned into the p363 overexpression plasmid using PacI and XmaI restriction sites to be in frame with a C-terminal TEV site, 3× StreptagII, and 9× His tag. The recombinant protein was overexpressed in yeast using a GAL

induction system in the D1074 strain and purified as described previously (St-Pierre *et al.*, 2009). Briefly, protein expression was induced with 2% galactose for 6 to 8 h at 30 °C. Following induction, cells were flash frozen. Frozen cells were lysed by mechanical shearing in a cryogenic grinder (SPEX SamplePrep). The resulting powder was reconstituted in buffer containing protease inhibitors (Roche) and centrifuged at 80k rpm for 20 min at 4 °C. The supernatant was passed through a 0.45-µm syringe filter and then applied to a HisTrap column. Samples containing Las17 were pooled and dialyzed in a Slide-a-Lyzer cassette (Thermo Fisher) after addition of TEV protease. After a brief incubation with Ni-agarose to remove the protease and cleaved His tag, Las17 was concentrated in an Ultra-4 centrifugal filter device (Amicon). Aliquots of purified Las17 were flash frozen in liquid nitrogen.

3.4.3 Supported Lipid Bilayer Production

Supported lipid bilayers were prepared using a previously published protocol with minor modifications (Wu et al., 2010). Briefly, chloroform stocks of lipids (Avanti Polar Lipids) were combined in a glass vial etched with Piranha solution (3:1 H_2SO_4/H_2O_2) according to the molar ratios listed for each experiment. Unless otherwise listed, the lipid composition used for each experiment was 75% phosphatidylcholine (PC), 5% DGS-NTA, 20% phosphatidylserine (PS). In instances where a membrane dye was added to visualize membranes, PC concentration was lowered accordingly. The lipid mixture was dried at 42 °C under vacuum using a rotary evaporator. After brief exposure to nitrogen, the dried lipid film was rehydrated in deionized water to 1 mg/mL. The mixture was passed through a microextruder (Avanti Polar Lipids) fitted with a 0.1-µm filter 11 times to generate small unilamellar vesicles (SUVs). SUVs were used immediately or stored for up to 5 d at 4 °C.

Polystyrene or silica microspheres (Bangs Laboratories) were cleaned for 15 min in 1% Helmenex, followed by three wash steps in ddH2O. SUVs diluted 1:5 in 10× TBS (to a final concentration of 2× TBS) were incubated with the microbeads, generating supported lipid bilayers through self-assembly. Unruptured vesicles were removed via multiple wash steps in TBS.

3.4.4 Generation of Whole-Cell Lysates

Cells were grown in YPD at 25 °C to an OD600 of 0.6 to 0.8, as measured on an Ultrospec 10 Cell Density Meter (Amersham). Cells from 4 L of culture were harvested by centrifugation, washed in cold water, and centrifuged again. Standing moisture was removed from pellets, and cells were flash frozen in liquid N2 and then stored at −80 °C. Frozen cultures were lysed by mechanical shearing in a prechilled cryogenic grinder (SPEX SamplePrep) using a medium-sized SPEX vial that had been prechilled in liquid nitrogen. Milling consisted of a 5 min prechill followed by 6 to 10 cycles comprising 3 min of grinding and 1 min of rest. The sample vial remained submerged in liquid N2 throughout the milling process. Powdered lysate was collected in a 50-mL conical vial

that had been prechilled in liquid nitrogen. Lysate preparations stored at −80 °C were stable for >6 mo but were highly sensitive to temperature excursions.

3.4.5 Yeast Extract Preparation

HK buffer (40 mM HEPES, pH 7.5, 200 mM KCl, and 1 mM PMSF) was supplemented with cOmplete mini EDTA-free protease inhibitor cocktail (Roche), according to manufacturer specifications. Powdered lysate was weighed out into a prechilled 5-mL glass beaker using a prechilled spatula. Then, 875 µL of supplemented HK buffer at 4 °C was added to each gram of yeast powder. After thawing on ice, samples were centrifuged in a prechilled polycarbonate ultracentrifuge tube for 25 min at 345,000 × g at 4 °C. The cleared supernatant was collected immediately following the centrifuge run using a syringe to transfer it to a prechilled 1.5-mL tube and was then used in an assay within 10 min of the final ultracentrifugation step. Care was taken to avoid disturbing either the pellet or the white lipid layer. Reconstitution of actin assembly was impaired by gaps exceeding 10 min between the end of centrifugation and addition to bilayers, as well as by any warming of the powdered lysate above−80 °C prior to thawing in the supplemented HK buffer.

3.4.5 Membrane Functionalization and Bead Assay

For 1 h, 180 nM yeast WASP (Las17) was incubated on the membranes. Beads were washed and then incubated in 1% casein for 15 min to block nonspecific binding. After washing to remove excess casein, beads were stored in 1× TBS for up to 1 h. Then, 1 to 2 µL functionalized bilayers were added to the cytosolic extract to a total reaction volume of 20 µL. In addition, 1 mM ATP and, where noted, 180 µM LatA (Sigma Aldrich) were added immediately to the bilayer and extract mixture. Microbeads were spotted on slides and imaged within 1 h.

3.4.6 Microscopy and Image Analysis

3.4.6.1 Fluorescence microscopy

Except where noted otherwise, all images were acquired on a Nikon Eclipse Ti inverted Yokogawa spinning disk confocal microscope fitted with Andor CSU-X spinning disc confocal equipment and controlled by Nikon Elements software. Imaging was performed using a 100× 1.45 NA Plan Apo λ oil immersion objective and an Andor IXon X3 EM-CCD camera. GFP, RFP, and Atto647 fluorescence were excited using 488-, 561- and 638-nm lasers, respectively. Images for figure panel S1C were collected using a Nikon Eclipse Ti microscope equipped with a 100× 1.4 NA Plan Apo VC oil objective and an Andor Neo sCMOS camera. The system was controlled using Metamorph software (Molecular Devices). Images for figure panels 4A (lower subpanel) and 4B (both subpanels) were acquired on a AxioObserver Zeiss LSM 710 Laser Scanning Confocal with 40× 1.4 NA Plan Apo oil immersion objective and PMT detector. GFP and Atto647 fluorescence was excited using 488- and 633-nm lasers,

respectively. The system was controlled with Zen 2010 software. All imaging devices were kept in rooms maintained at 23 to 25 °C.

3.4.6.2 Fluorescence recovery after photobleaching

Membrane fluidity was assessed using fluorescence recovery after photobleaching (FRAP) performed on a Zeiss LSM 710 confocal microscope fitted with a Plan-Apochromat 63× 1.40 NA oil immersion DIC M27 and Zen software. An ROI drawn over a portion of the bilayer was bleached using 594-nm laser light at 100% laser power for 50 iterations. Images were taken every 780 ms before and after bleaching. Images were analyzed using ImageJ software. The plot profile function in Fiji was used to measure the signal intensity of TexasRed-DHPE in the bleached ROI and the opposite (unbleached) side of the bilayer. FRAP data were normalized to the highest and lowest mean values in the prebleach condition.

3.4.6.3 CLEM

Supported lipid bilayers were generated on polystyrene microbeads and incubated with 500 nM scWASP and cytosolic extract, as described above. Reactions were fixed in 4% paraformaldehyde, 0.05% glutaraldehyde for at least 30 min at 4 °C. Beads were deposited on poly-L-lysine-coated 35-mm gridded glass-bottom dishes (MatTek). After washing, adherent beads were embedded in 2% low melting point agarose (Electron Microscopy Sciences) and submerged in 1× TBS for microscopy. Regions of interest were identified by Atto647-DOPE and Sac6-GFP fluorescence signal, and then mapped to spatial coordinates on the gridded coverslip by brightfield imaging. Samples were then washed in 1× PBS and stained with 1% osmium tetroxide and 1.6% potassium ferricyanide at 4 °C for 45 min. Following additional washes with PBS, and a quick exchange in water, samples were dehydrated with an ascending gradient of ethanol followed by pure ethanol before they were progressively infiltrated with resin and left overnight in unaccelerated Epon resin (Ted Pella). Epon resin with accelerant was exchanged onto the sample three times, then the dishes were incubated at 60 °C for 16 to 20 h for resin polymerization. Following polymerization, the glass coverslips were removed using ultra-thin Personna razor blades (EMS). CLEM was performed to visualize specific beads within regions of interest. Regions of interest, identified by the gridded alpha-numerical labeling on the plates were carefully removed, precisely trimmed to the area of interest, and mounted on a blank resin block with cyanoacrylate glue for sectioning. Serial thin sections (80 nm) were cut using a Leica UC6 ultramicrotome (Leica) from the surface of the block until approximately 4 to 5 microns in to ensure complete capture of the bead. Section-ribbons were then collected sequentially onto formvar-coated slots or 50 mesh grids. The grids were poststained with 2% uranyl acetate followed by Reynold's lead citrate, for 5 min each. The sections were imaged using a FEI Tecnai 12 120kV TEM (FEI) and data recorded using either a Gatan US1000 CCD with Digital Micrograph 3 or a Gatan Rio 16 CMOS

with Gatan Microscopy Suite software (Gatan Inc.). Images were adjusted for brightness and contrast in ImageJ (NIH), and rotated, but otherwise unaltered.

3.4.6.4 Image analysis

Images were processed using ImageJ software. Pixel intensity values were rescaled identically for all images from an experiment. To allow visualization of small structures, some pixels in some images were intentionally saturated. To quantify Sac6 accumulation on lipid bilayers of varying compositions, beads were manually counted in the DIC channel and then scored for presence or absence of Sac6 fluorescence.

Additional image processing of time-lapse spinning disc confocal fluorescence microscopy data was performed using ImageJ plugins following recommendations by Picco et al. (Picco and Kaksonen, 2017). First, background subtraction was applied to raw data from each channel using a rolling ball algorithm with 100 pixel radius. We then performed bleach correction with an exponential decay model on each individual channel except when imaging Sac6-RFP, because for this marker there was no decay in fluorescence signal over the course of our time-lapses. Individual beads were then cropped and processed with a 3D drift correction algorithm so that positions of vesicles could later be measured relative to their source bead. The resulting multichannel volumetric time-lapse processed data were then rendered in 3D and assembled into montages using custom python scripts [available on GitHub (https://github.com/DrubinBarnes/Stoops_Ferrin_et_al_2023)].

To quantify vesiculation dynamics, we used the TrackMate plugin of ImageJ to manually track the position of vesicles in time-lapse data after the processing steps described in the previous paragraph. We measured the 3D displacement of each tracked vesicle from its starting position overtime, as well as the average fluorescence intensity of a 0.4-µm radius sphere around the center of each vesicle over time. To collectively analyze data for all tracked vesicles, we first aligned each individual trajectory in time by the inflection point of the displacement curve (adapted from (Sun et al., 2019)). The inflection point was defined as the time point at which the vesicle displacement was the maximum negative difference from a linear regression fit to each vesiculation event trace, out of all the time points before the point of the maximum positive difference. Aligned fluorescence intensity curves were normalized to the maximum value for each vesicle before calculating the average and SD for all tracked vesicles.

Chapter Four
Final conclusions and outlook

Taken together, my thesis research advances our understanding of the functional capacity of actin networks. A rich collection of past mechanistic studies have revealed a variety of emergent mechanical properties of actin networks that depend on the cellular context and participation of different actin-binding proteins. For instance, the identity of the dominant actin nucleation factor initiating a given actin network is a major determinant of the network's architecture and function (Chhabra and Higgs, 2007; Michelot and Drubin, 2011; Antkowiak *et al.*, 2019), allowing numerous distinct actin networks to simultaneously exist in the same cell. Other lines of research have connected filament-binding proteins to their network-level mechanical roles, such as the catch-bond activity of the focal adhesion actin crosslinker α-actinin-4 lending overall strength to the network (Mulla *et al.*, 2022), or the presence of the endocytic actin crosslinkers Sac6 providing stiffness to the network, which increases the efficiency of endocytosis (Planade *et al.*, 2019).

In this work, I extend that line of investigation to demonstrate the ability of branched actin nucleators to template mechanically effective actin networks during CME. I used theoretical modeling to mechanistically describe how the localization of coat-actin linkers and branched actin nucleators can direct adaptive actin self-organization during mammalian CME. Then I experimentally reconstituted the budding yeast endocytic actin network to show that a membrane-pulling actin network can self-organize from soluble cytoplasmic components under the sole direction of actin nucleators on the membrane. While these two approaches address the same broad question of endocytic actin force generation, several gaps between them still remain that must be bridged before they can be integrated into a truly complementary emergent mechanics investigation.

4.1 Open questions in agent-based modeling of endocytic actin

While a major strength of the work described in Chapter 2 is the minimal list of components in the agent-based model in order to illustrate the self-organizing capacity of those components alone, it is at the same time a major caveat in making biological interpretations of the model predictions. The model includes activities from 5 different proteins, whereas several dozen different protein species are actually present during CME. Each of these additional components undoubtedly influences the actin network's architecture and mechanics in ways that the current model cannot predict. The actin-regulatory activities conspicuously missing from the model include actin crosslinking by fimbrin (Adams, Botstein and Drubin, 1991; Skau *et al.*, 2011), actin turnover via ATP hydrolysis "aging" of monomers leading to branch dissociation and filament severing by cofilin (Lappalainen and Drubin, 1997; Rodal *et al.*, 1999; Chen

and Pollard, 2013; Bibeau, Gray and De La Cruz, 2021; Chung, Goode and Gelles, 2022), and myosin motor activity (Sun, Martin and Drubin, 2006; Cheng, Grassart and Drubin, 2012). Implementing each additional layer of complexity will reveal additional network properties and increase the possibilities for making experimentally testable predictions. Absence of these additional components may also explain why the maximum internalization of the current minimal model often does not reach the expected threshold for vesicle scission at higher membrane tension values.

Since publication of this work, I have added type I myosins to the model and have investigated their impact on the collective mechanics of the endocytic actin network. Type I myosin is a single-headed molecular motor that binds to actin filaments with its head domain and binds to the plasma membrane with its tail domain (McIntosh and Ostap, 2016). The head domain proceeds through a mechanochemical ATPase cycle in which ATP hydrolysis is coupled to a mechanical power stroke that can exert force on the bound actin filament (Greenberg and Ostap, 2013). Type I myosins localize to the base of endocytic pits concurrent with actin polymerization (Sun, Martin and Drubin, 2006; Mund *et al.*, 2018) and produce a dose-dependent response on CME efficiency (Cheng, Grassart and Drubin, 2012; Manenschijn *et al.*, 2019). A fascinating aspect of this class of myosins is the diversity in force sensitivity of actin binding kinetics. Some are relatively insensitive to force, while others behave more like catch bonds, meaning the actin-myosin dissociation rate decreases as the force on the bond increases (Figure 4.1A) (Laakso *et al.*, 2010; Pedersen *et al.*, 2023). This degree of force sensitivity was only very recently measured for the first endocytic myosin, which turns out to fall into the relatively force-insensitive category (Pedersen *et al.*, 2023). This same myosin was shown to faciliate an increase the size of endocytic actin networks through enhanced actin assembly *in vivo* (Manenschijn *et al.*, 2019), but we still lack mechanistic explanations for how the activity of individual type I myosins collectively change the actin architecture and improve the robustness of vesicle internalization. My agent-based CME modeling approach is excellently poised to address such detailed mechanistic questions.
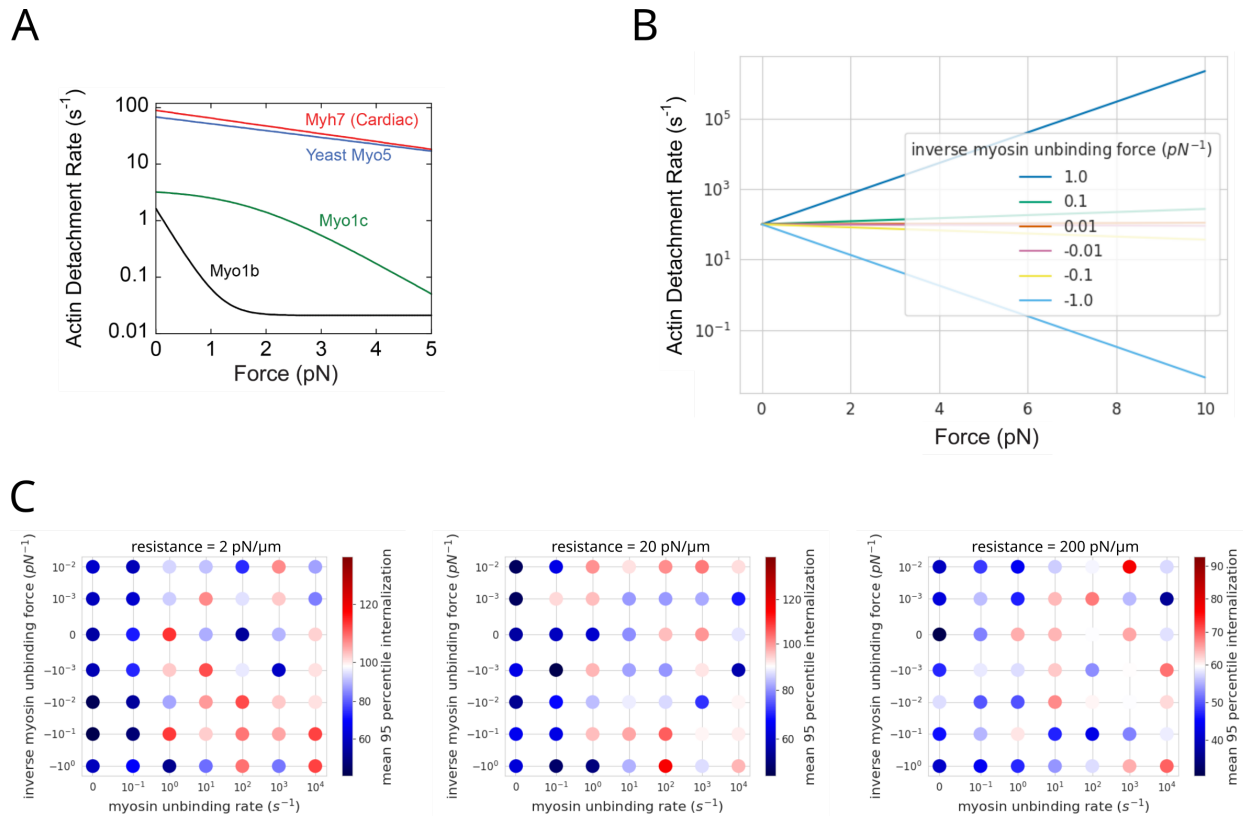
Figure 4.1 Type I myosins with weak catch bond activity can assist simulated CME internalization. (A) Diversity of catch bond activities among measured myosins. A stronger catch bond is defined as a more negative slope of actin detachment rate over increasing applied force. Yeast Myo5 (blue) participates in CME. Figure adapted from (Pedersen *et al.*, 2023). (B) Theoretical parameter range of slip bond and catch bond activities that can be simulated for model myosins. The inverse myosin unbinding force is the control parameter for this activity: a more positive value results in higher actin detachment rate with increasing force (slip bond), and a more negative value results in lower actin detachment rate with increasing force (catch bond). (C) Preliminary analyses of CME simulations over a range of model type I myosin kinetic parameters and resistance to internalization (analogous to membrane tension). For each resistance value (separate plots) and combination of myosin unloaded actin unbinding rate (x-axis) and inverse unbinding force (y-axis), the mean 95th percentile of internalization of 4 simulations is represented as the color corresponding to each plot's color bar. An inverse myosin unbinding force of 0 is characteristic of a force-insensitive myosin, a more positive value is characteristic of a slip bond, and a more negative value is characteristic of a catch bond (see panel B). White coloration is the mean 95th percentile of internalization in simulations with 0 myosins, redder colors indicate further internalization due to the presence of the myosins, and bluer colors indicate less internalization due to myosins.

I am now in the process of analyzing CME simulations incorporating type I myosins with properties constrained by single-molecule biochemistry and live-cell microscopy. While further parameter space is yet to be explored, preliminary results show regimes in which the addition of myosins increases internalization distance (Figure 4.1C). At low resistance to internalization, the myosin is assistive over a very wide range of catch bond parameters (Figure 4.1C, left). As simulated resistance increases, efficient CME favors increasing unbinding rate and possibly stronger catch bond activity (Figure 4.1C, middle and right). More rigorous parameter sweeps and CME efficiency analyses will predict the optimal type I myosin properties for a range of

mechanical loads, potentially revealing a pattern of which parameter combination is the most robust to changing mechanical conditions that the cell might experience in its native environment. Further, detailed analyses of simulated actin organization in the most robust myosin conditions will address a major open question concerning the mechanism of myosin-mediated actin reorganization during CME: does myosin activity influence actin architecture by modulating individual filament elongation rates, modulating branched actin nucleation rates, anchoring filaments to the plasma membrane, direct displacement of the network by the motor power stroke, or by some combination of these mechanisms (Manenschijn *et al.*, 2019; Pedersen and Drubin, 2019; Pedersen *et al.*, 2023)?

4.2 Open questions in reconstitution of endocytic actin networks

Just as I view my work on the minimal agent-based model in Chapter 2 as the establishment of a platform for future elaboration with one component at a time to understand its emergent effects on CME mechanics, the reconstitution system described in Chapter 3 is another new platform for addressing the same questions from an experimental approach. I believe that the richness of tweakable parameters in the system, from the control of defined components such as lipid composition and purified proteins, to the power of yeast genetics to manipulate the composition of the cytoplasmic extract, means we have barely scratched the surface of investigations that are possible with this reconstitution system.

The first mystery arising from the results presented thus far is the discrepancy in timescales between reconstituted membrane budding (minutes) and native CME (seconds) (Lu, Drubin and Sun, 2016; Kaksonen and Roux, 2018). While longer timescales are not unusual in biochemical reconstitution systems (Baker *et al.*, 1988), it will nonetheless be information to identify the source of this delay. Possible explanations may include dilution of the cytoplasm during sample processing, surface concentration of actin nucleators on the SLB, lack of recruitment of coat proteins to the SLB, or loss of important cytoplasmic components during ultracentrifugation.

An exciting future avenue for this system is stepping further upstream of the actin module in the native progression of CME to investigate the self-organizing capacity of earlier coat proteins and cargo molecules. Preliminary unpublished experiments by my collaborator Emily Stoops showed that bead SLBs coated with CME initiator protein Ede1 were competent to recruit more Ede1 from cytoplasmic extracts, as well as another early protein Syp1 and the actin crosslinker Sac6 (data not shown). This system is poised for future investigators to compare the actin reconstitution and membrane deformation dynamics between scWASP-coated beads and Ede1-coated beads in order to determine what additional degree of regulation is made possible by the presence of earlier CME proteins. Further, recent *in vivo* evidence has pointed to endocytic cargo as a potential signal regulating the progression from early protein assembly to late membrane-bending phases of CME (Pedersen *et al.*,

2020). The development of a method to tether a model endocytic cargo to bead SLBs in extracts would produce a major advance in our ability to test the cargo-based signal hypothesis.

To approach the reconstitution system from a different angle, future studies could investigate the role of specific components or even specific biochemical activities on the whole network by using cytoplasmic extracts generated from yeast mutants. Inspired by experiments in other actin reconstitution systems (Planade *et al.*, 2019), deletion or mutation of certain genes encoding actin-binding proteins can result in reconstituted actin networks with different properties, thus suggesting how the wild-type proteins influence the network when present. I would be particularly interested to observe any changes in actin network dynamics and membrane deformation in extracts lacking type I myosin, as my preliminary modeling results would predict that the force-generating capacity of the network would be diminished in such a mutant cytoplasm.

Beyond the protein components, plasma membrane lipid composition is known to play an important role in regulating CME progression (Sun and Drubin, 2012; Garcia-Alai *et al.*, 2018; Kaksonen and Roux, 2018; Yamamoto *et al.*, 2018). This presents a facet of this experimental system that is waiting to be comprehensively explored. The lipid compositions used in the results described here were chosen empirically by selecting for the most robust actin assembly. Rigorous investigation of the influence of SLB lipid composition on recruitment of other CME proteins from the cytoplasmic extract may reveal regimes where the lipids have a dominant organizing role in downstream protein assembly, as previously shown *in vivo* (Sun and Drubin, 2012).

Finally, this system has the potential to complement results and test predictions from CME simulations if more rigorous quantitative measurements can be produced. One major factor limiting quantitative analysis of these reconstitution experiments is the dynamics of protein assembly and membrane deformation. While the order of events described earlier was highly reproducible qualitatively, the actual timing was unpredictable. This variability meant that events of interest (initiation of each protein's assembly and membrane bending) occurred rarely, and these studies were therefore very time and labor intensive making capturing events by time lapse fluorescence microscopy or fixed electron microscopy very challenging. I hope that future systematic exploration of experimental parameters like yeast culture harvesting conditions, cytoplasmic extract preparation, reaction temperature, aging of reaction components, and lipid composition can improve the reproducibility of event timing so that enough data can be generated for quantitative comparisons between experimental conditions. The other side of the workflow for making quantitative comparisons is unbiased, automated analysis methods. Most data quantifications shown here (3D vesicle tracking, scoring actin accumulation, and identifying membrane deformation events) were performed manually, meaning that only the most obvious events were measured. I would hope that future work building on this system will incorporate automated image

analysis techniques like segmentation of fluorescent membrane/protein signal and particle tracking of budded vesicles in order to remove the risk of bias from visual classification, making possible detection and measurement of more subtle events. With these experimental and analytical improvements in place, I could imagine the reconstitution system having the ability to produce measurements that can be compared against predictions from simulation readouts. I envision an integrated investigation, wherein simulations predict changes to outputs such as membrane internalization velocity and actin assembly rate due to modeled deletion or mutation of specific components, which can be directly tested by performing the same measurements in appropriate mutant cytoplasmic extract reconstitution experiments.

References

Abercrombie, M. (1980) 'The Croonian Lecture, 1978: The Crawling Movement of Metazoan Cells', *Proceedings of the Royal Society of London. Series B, Biological Sciences*, 207(1167), pp. 129–147.

Adams, A.E.M., Botstein, D. and Drubin, D.G. (1991) 'Requirement of yeast fimbrin for actin organization and morphogenesis in vivo', *Nature*, 354(6352), pp. 404–408. Available at: https://doi.org/10.1038/354404a0.

Akamatsu, M. *et al.* (2020) 'Principles of self-organization and load adaptation by the actin cytoskeleton during clathrin-mediated endocytosis', *eLife*. Edited by P. Bassereau et al., 9, p. e49840. Available at: https://doi.org/10.7554/eLife.49840.

Akin, O. and Mullins, R.D. (2008) 'Capping Protein Increases the Rate of Actin-Based Motility by Promoting Filament Nucleation by the Arp2/3 Complex', *Cell*, 133(5), pp. 841–851. Available at: https://doi.org/10.1016/j.cell.2008.04.011.

Alimohamadi, H. *et al.* (2018) 'The role of traction in membrane curvature generation', *Molecular Biology of the Cell*, 29(16), pp. 2024–2035. Available at: https://doi.org/10.1091/mbc.E18-02-0087.

Almeida-Souza, L. *et al.* (2018) 'A Flat BAR Protein Promotes Actin Polymerization at the Base of Clathrin-Coated Pits', *Cell* [Preprint]. Available at: https://doi.org/10.1016/j.cell.2018.05.020.

Amann, K.J. and Pollard, T.D. (2001) 'The Arp2/3 complex nucleates actin filament branches from the sides of pre-existing filaments', *Nature Cell Biology*, 3(3), pp. 306–310. Available at: https://doi.org/10.1038/35060104.

Antkowiak, A. *et al.* (2019) 'Sizes of actin networks sharing a common environment are determined by the relative rates of assembly', *PLOS Biology*, 17(6), p. e3000317. Available at: https://doi.org/10.1371/journal.pbio.3000317.

Arasada, R. *et al.* (2018) 'High-speed superresolution imaging of the proteins in fission yeast clathrin-mediated endocytic actin patches', *Molecular Biology of the Cell*, 29(3), pp. 295–303. Available at: https://doi.org/10.1091/mbc.e17-06-0415.

Avinoam, O. *et al.* (2015) 'Endocytic sites mature by continuous bending and remodeling of the clathrin coat', *Science*, 348(6241), pp. 1369–1372. Available at: https://doi.org/10.1126/science.aaa9555.

Baker, D. *et al.* (1988) 'Reconstitution of SEC gene product-dependent intercompartmental protein transport', *Cell*, 54(3), pp. 335–344. Available at: https://doi.org/10.1016/0092-8674(88)90196-1.

Balzer, C.J. *et al.* (2018) 'Dip1 Co-opts Features of Branching Nucleation to Create Linear Actin Filaments that Activate WASP-Bound Arp2/3 Complex', *Current Biology*, 28(23), pp. 3886-3891.e4. Available at: https://doi.org/10.1016/j.cub.2018.10.045.

Basu, R. and Chang, F. (2011) 'Characterization of Dip1p Reveals a Switch in Arp2/3-Dependent Actin Assembly for Fission Yeast Endocytosis', *Current Biology*, 21(11), pp. 905–916. Available at: https://doi.org/10.1016/j.cub.2011.04.047.

Beltzner, C.C. and Pollard, T.D. (2008) 'Pathway of Actin Filament Branch Formation by

Arp2/3 Complex*', *Journal of Biological Chemistry*, 283(11), pp. 7135–7144. Available at: https://doi.org/10.1074/jbc.M705894200.

Berro, J. *et al.* (2010) 'Mathematical Modeling of Endocytic Actin Patch Kinetics in Fission Yeast: Disassembly Requires Release of Actin Filament Fragments', *Molecular Biology of the Cell*, 21(16), pp. 2905–2915. Available at: https://doi.org/10.1091/mbc.e10-06-0494.

Berro, J. and Pollard, T.D. (2014) 'Synergies between Aip1p and capping protein subunits (Acp1p and Acp2p) in clathrin-mediated endocytosis and cell polarization in fission yeast', *Molecular Biology of the Cell*, 25(22), pp. 3515–3527. Available at: https://doi.org/10.1091/mbc.e13-01-0005.

Bhave, M. *et al.* (2020) 'Functional characterization of 67 endocytic accessory proteins using multiparametric quantitative analysis of CCP dynamics', *Proceedings of the National Academy of Sciences*, 117(50), pp. 31591–31602. Available at: https://doi.org/10.1073/pnas.2020346117.

Bibeau, J.P., Gray, S. and De La Cruz, E.M. (2021) 'Clusters of a few bound cofilins sever actin filaments', *Journal of Molecular Biology*, p. 166833. Available at: https://doi.org/10.1016/j.jmb.2021.166833.

Bieling, P. *et al.* (2016) 'Force Feedback Controls Motor Activity and Mechanical Properties of Self-Assembling Branched Actin Networks', *Cell*, 164(1–2), pp. 115–127. Available at: https://doi.org/10.1016/j.cell.2015.11.057.

Bieling, P. *et al.* (2018) 'WH2 and proline-rich domains of WASP-family proteins collaborate to accelerate actin filament elongation', *The EMBO Journal*, 37(1), pp. 102–121. Available at: https://doi.org/10.15252/embj.201797039.

Blanchoin, L. *et al.* (2000) 'Direct observation of dendritic actin filament networks nucleated by Arp2/3 complex and WASP/Scar proteins', *Nature*, 404(6781), pp. 1007–1011. Available at: https://doi.org/10.1038/35010008.

Boulant, S. *et al.* (2011) 'Actin dynamics counteract membrane tension during clathrin-mediated endocytosis', *Nature Cell Biology*, 13(9), pp. 1124–1131. Available at: https://doi.org/10.1038/ncb2307.

Brach, T. *et al.* (2014) 'The Initiation of Clathrin-Mediated Endocytosis Is Mechanistically Highly Flexible', *Current Biology*, 24(5), pp. 548–554. Available at: https://doi.org/10.1016/j.cub.2014.01.048.

Brady, R.J. *et al.* (2010) 'Regulation of Hip1r by epsin controls the temporal and spatial coupling of actin filaments to clathrin-coated pits', *Journal of Cell Science*, 123(21), pp. 3652–3661. Available at: https://doi.org/10.1242/jcs.066852.

Brett, T.J. *et al.* (2006) 'Structural definition of the F-actin–binding THATCH domain from HIP1R', *Nature Structural & Molecular Biology*, 13(2), pp. 121–130. Available at: https://doi.org/10.1038/nsmb1043.

Brieher, W.M., Coughlin, M. and Mitchison, T.J. (2004) 'Fascin-mediated propulsion of Listeria monocytogenes independent of frequent nucleation by the Arp2/3 complex', *The Journal of Cell Biology*, 165(2), pp. 233–242. Available at: https://doi.org/10.1083/jcb.200311040.

Bucher, D. *et al.* (2018) 'Clathrin-adaptor ratio and membrane tension regulate the flat-to-curved transition of the clathrin coat during endocytosis', *Nature Communications*, 9(1), p. 1109. Available at: https://doi.org/10.1038/s41467-018-03533-0.

Buser, C. and Drubin, D.G. (2013) 'Ultrastructural Imaging of Endocytic Sites in Saccharomyces cerevisiae by Transmission Electron Microscopy and Immunolabeling', *Microscopy and Microanalysis*, 19(2), pp. 381–392. Available at: https://doi.org/10.1017/S1431927612014304.

Carlsson, A.E. (2001) 'Growth of Branched Actin Networks against Obstacles', *Biophysical Journal*, 81(4), pp. 1907–1923. Available at: https://doi.org/10.1016/S0006-3495(01)75842-0.

Carlsson, A.E. (2018) 'Membrane bending by actin polymerization', *Current Opinion in Cell Biology*, 50, pp. 1–7. Available at: https://doi.org/10.1016/j.ceb.2017.11.007.

Carlsson, A.E. and Bayly, P.V. (2014) 'Force Generation by Endocytic Actin Patches in Budding Yeast', *Biophysical Journal*, 106(8), pp. 1596–1606. Available at: https://doi.org/10.1016/j.bpj.2014.02.035.

Case, L.B. *et al.* (2019) 'Stoichiometry controls activity of phase-separated clusters of actin signaling proteins', *Science*, 363(6431), pp. 1093–1097. Available at: https://doi.org/10.1126/science.aau6313.

Chaudhuri, O., Parekh, S.H. and Fletcher, D.A. (2007) 'Reversible stress softening of actin networks', *Nature*, 445(7125), pp. 295–298. Available at: https://doi.org/10.1038/nature05459.

Chen, C.-Y. and Brodsky, F.M. (2005) 'Huntingtin-interacting Protein 1 (Hip1) and Hip1-related Protein (Hip1R) Bind the Conserved Sequence of Clathrin Light Chains and Thereby Influence Clathrin Assembly in Vitro and Actin Distribution in Vivo*', *Journal of Biological Chemistry*, 280(7), pp. 6109–6117. Available at: https://doi.org/10.1074/jbc.M408454200.

Chen, H. *et al.* (1998) 'Epsin is an EH-domain-binding protein implicated in clathrin-mediated endocytosis', *Nature*, 394(6695), pp. 793–797. Available at: https://doi.org/10.1038/29555.

Chen, Q. and Pollard, T.D. (2013) 'Actin Filament Severing by Cofilin Dismantles Actin Patches and Produces Mother Filaments for New Patches', *Current Biology*, 23(13), pp. 1154–1162. Available at: https://doi.org/10.1016/j.cub.2013.05.005.

Cheng, J., Grassart, A. and Drubin, D.G. (2012) 'Myosin 1E coordinates actin assembly and cargo trafficking during clathrin-mediated endocytosis', *Molecular Biology of the Cell*, 23(15), pp. 2891–2904. Available at: https://doi.org/10.1091/mbc.E11-04-0383.

Chhabra, E.S. and Higgs, H.N. (2007) 'The many faces of actin: matching assembly factors with cellular structures', *Nature Cell Biology*, 9(10), pp. 1110–1121. Available at: https://doi.org/10.1038/ncb1007-1110.

Chu, D.S., Pishvaee, B. and Payne, G.S. (1996) 'The Light Chain Subunit Is Required for Clathrin Function in Saccharomyces cerevisiae*', *Journal of Biological Chemistry*, 271(51), pp. 33123–33130. Available at: https://doi.org/10.1074/jbc.271.51.33123.

Chung, J., Goode, B.L. and Gelles, J. (2022) 'Single-molecule analysis of actin filament debranching by cofilin and GMF', *Proceedings of the National Academy of Sciences*, 119(29), p. e2115129119. Available at: https://doi.org/10.1073/pnas.2115129119.

Clarke, N.I. and Royle, S.J. (2018) 'FerriTag is a new genetically-encoded inducible tag for correlative light-electron microscopy', *Nature Communications*, 9(1), p. 2604. Available at: https://doi.org/10.1038/s41467-018-04993-0.

Collins, A. *et al.* (2011) 'Structural Organization of the Actin Cytoskeleton at Sites of Clathrin-Mediated Endocytosis', *Current Biology*, 21(14), pp. 1167–1175. Available at: https://doi.org/10.1016/j.cub.2011.05.048.

Daste, F. *et al.* (2017) 'Control of actin polymerization via the coincidence of phosphoinositides and high membrane curvature', *Journal of Cell Biology*, 216(11), pp. 3745–3765. Available at: https://doi.org/10.1083/jcb.201704061.

David, C. *et al.* (1996) 'A role of amphiphysin in synaptic vesicle endocytosis suggested by its binding to dynamin in nerve terminals.', *Proceedings of the National Academy of Sciences*, 93(1), pp. 331–335. Available at: https://doi.org/10.1073/pnas.93.1.331.

Day, K.J. *et al.* (2021) 'Liquid-like protein interactions catalyse assembly of endocytic vesicles', *Nature Cell Biology*, 23(4), pp. 366–376. Available at: https://doi.org/10.1038/s41556-021-00646-5.

De La Cruz, E.M. and Gardel, M.L. (2015) 'Actin Mechanics and Fragmentation*', *Journal of Biological Chemistry*, 290(28), pp. 17137–17144. Available at: https://doi.org/10.1074/jbc.R115.636472.

De La Cruz, E.M., Martiel, J.-L. and Blanchoin, L. (2015) 'Mechanical Heterogeneity Favors Fragmentation of Strained Actin Filaments', *Biophysical Journal*, 108(9), pp. 2270–2281. Available at: https://doi.org/10.1016/j.bpj.2015.03.058.

Dimova, R. (2014) 'Recent developments in the field of bending rigidity measurements on membranes', *Advances in Colloid and Interface Science*, 208, pp. 225–234. Available at: https://doi.org/10.1016/j.cis.2014.03.003.

Ditlev, J.A. *et al.* (2012) 'Stoichiometry of Nck-dependent actin polymerization in living cells', *J Cell Biol*, 197(5), pp. 643–658. Available at: https://doi.org/10.1083/jcb.201111113.

Diz-Muñoz, A. *et al.* (2016) 'Membrane Tension Acts Through PLD2 and mTORC2 to Limit Actin Network Assembly During Neutrophil Migration', *PLOS Biology*, 14(6), p. e1002474. Available at: https://doi.org/10.1371/journal.pbio.1002474.

Dmitrieff, S. and Nédélec, F. (2015) 'Membrane Mechanics of Endocytosis in Cells with Turgor', *PLoS Computational Biology*, 11(10). Available at: https://doi.org/10.1371/journal.pcbi.1004538.

Dmitrieff, S. and Nédélec, F. (2016) 'Amplification of actin polymerization forces', *Journal of Cell Biology*, 212(7), pp. 763–766. Available at: https://doi.org/10.1083/jcb.201512019.

Dobzhansky, T. (1973) 'Nothing in Biology Makes Sense except in the Light of Evolution', *The American Biology Teacher*, 35(3), pp. 125–129. Available at: https://doi.org/10.2307/4444260.

Dumont, S. and Prakash, M. (2014) 'Emergent mechanics of biological structures', *Molecular Biology of the Cell*, 25(22), pp. 3461–3465. Available at: https://doi.org/10.1091/mbc.e14-03-0784.

Engqvist-Goldstein, Å.E.Y. *et al.* (1999) 'An Actin-Binding Protein of the Sla2/Huntingtin Interacting Protein 1 Family Is a Novel Component of Clathrin-Coated Pits and Vesicles', *Journal of Cell Biology*, 147(7), pp. 1503–1518. Available at: https://doi.org/10.1083/jcb.147.7.1503.

Engqvist-Goldstein, Å.E.Y. *et al.* (2001) 'The actin-binding protein Hip1R associates with clathrin during early stages of endocytosis and promotes clathrin assembly in vitro', *Journal of Cell Biology*, 154(6), pp. 1209–1224. Available at: https://doi.org/10.1083/jcb.200106089.

Engqvist-Goldstein, Å.E.Y. *et al.* (2004) 'RNAi-mediated Hip1R Silencing Results in Stable Association between the Endocytic Machinery and the Actin Assembly Machinery', *Molecular Biology of the Cell*, 15(4), pp. 1666–1679. Available at: https://doi.org/10.1091/mbc.e03-09-0639.

Engqvist-Goldstein, Å.E.Y. and Drubin, D.G. (2003) 'Actin Assembly and Endocytosis: From Yeast to Mammals', *Annual Review of Cell and Developmental Biology*, 19(1), pp. 287–332. Available at: https://doi.org/10.1146/annurev.cellbio.19.111401.093127.

Fernández, P., Pullarkat, P.A. and Ott, A. (2006) 'A Master Relation Defines the Nonlinear Viscoelasticity of Single Fibroblasts', *Biophysical Journal*, 90(10), pp. 3796–3805. Available at: https://doi.org/10.1529/biophysj.105.072215.

Footer, M.J. *et al.* (2007) 'Direct measurement of force generation by actin filament polymerization using an optical trap', *Proceedings of the National Academy of Sciences*, 104(7), pp. 2181–2186. Available at: https://doi.org/10.1073/pnas.0607052104.

Foret, L. (2014) 'Shape and energy of a membrane bud induced by protein coats or viral protein assembly', *The European Physical Journal E*, 37(5), p. 42. Available at: https://doi.org/10.1140/epje/i2014-14042-1.

Gaetz, J. *et al.* (2006) 'Examining how the spatial organization of chromatin signals influences metaphase spindle assembly', *Nature Cell Biology*, 8(9), pp. 924–932. Available at: https://doi.org/10.1038/ncb1455.

Garcia-Alai, M.M. *et al.* (2018) 'Epsin and Sla2 form assemblies through phospholipid interfaces', *Nature Communications*, 9(1), pp. 1–13. Available at: https://doi.org/10.1038/s41467-017-02443-x.

Garner, R.M. and Theriot, J.A. (2022) 'Leading edge maintenance in migrating cells is an emergent property of branched actin network growth', *eLife*. Edited by A. Michelot, A. Akhmanova, and A. Michelot, 11, p. e74389. Available at: https://doi.org/10.7554/eLife.74389.

Geli, M.I. and Riezman, H. (1996) 'Role of Type I Myosins in Receptor-Mediated Endocytosis in Yeast', *Science*, 272(5261), pp. 533–535. Available at: https://doi.org/10.1126/science.272.5261.533.

Gittes, F. *et al.* (1993) 'Flexural rigidity of microtubules and actin filaments measured

from thermal fluctuations in shape.', *Journal of Cell Biology*, 120(4), pp. 923–934. Available at: https://doi.org/10.1083/jcb.120.4.923.

Goodson, H.V. *et al.* (1996) 'Synthetic lethality screen identifies a novel yeast myosin I gene (MYO5): myosin I proteins are required for polarization of the actin cytoskeleton.', *Journal of Cell Biology*, 133(6), pp. 1277–1291. Available at: https://doi.org/10.1083/jcb.133.6.1277.

Grassart, A. *et al.* (2014) 'Actin and dynamin2 dynamics and interplay during clathrin-mediated endocytosis', *Journal of Cell Biology*, 205(5), pp. 721–735. Available at: https://doi.org/10.1083/jcb.201403041.

Greenberg, M.J. and Ostap, E.M. (2013) 'Regulation and control of myosin-I by the motor and light chain-binding domains', *Trends in Cell Biology*, 23(2), pp. 81–89. Available at: https://doi.org/10.1016/j.tcb.2012.10.008.

Hassinger, J.E. *et al.* (2017) 'Design principles for robust vesiculation in clathrin-mediated endocytosis', *Proceedings of the National Academy of Sciences*, p. 201617705. Available at: https://doi.org/10.1073/pnas.1617705114.

Haugwitz, M. *et al.* (1994) 'Dictyostelium amoebae that lack G-actin-sequestering profilins show defects in F-actin content, cytokinesis, and development', *Cell*, 79(2), pp. 303–314. Available at: https://doi.org/10.1016/0092-8674(94)90199-6.

Heald, R. *et al.* (1996) 'Self-organization of microtubules into bipolar spindles around artificial chromosomes in Xenopus egg extracts', *Nature*, 382(6590), pp. 420–425. Available at: https://doi.org/10.1038/382420a0.

Idrissi, F.-Z. *et al.* (2008) 'Distinct acto/myosin-I structures associate with endocytic profiles at the plasma membrane', *Journal of Cell Biology*, 180(6), pp. 1219–1232. Available at: https://doi.org/10.1083/jcb.200708060.

Idrissi, F.-Z. *et al.* (2012) 'Ultrastructural dynamics of proteins involved in endocytic budding', *Proceedings of the National Academy of Sciences*, 109(39), pp. E2587–E2594. Available at: https://doi.org/10.1073/pnas.1202789109.

Isambert, H. *et al.* (1995) 'Flexibility of Actin Filaments Derived from Thermal Fluctuations: EFFECT OF BOUND NUCLEOTIDE, PHALLOIDIN, AND MUSCLE REGULATORY PROTEINS*', *Journal of Biological Chemistry*, 270(19), pp. 11437–11444. Available at: https://doi.org/10.1074/jbc.270.19.11437.

Jonsdottir, G.A. and Li, R. (2004) 'Dynamics of Yeast Myosin I: Evidence for a Possible Role in Scission of Endocytic Vesicles', *Current Biology*, 14(17), pp. 1604–1609. Available at: https://doi.org/10.1016/j.cub.2004.08.055.

Kaksonen, M. and Roux, A. (2018) 'Mechanisms of clathrin-mediated endocytosis', *Nature Reviews Molecular Cell Biology* [Preprint]. Available at: https://doi.org/10.1038/nrm.2017.132.

Kaksonen, M., Sun, Y. and Drubin, D.G. (2003) 'A Pathway for Association of Receptors, Adaptors, and Actin during Endocytic Internalization', *Cell*, 115(4), pp. 475–487. Available at: https://doi.org/10.1016/S0092-8674(03)00883-3.

Kaksonen, M., Toret, C.P. and Drubin, D.G. (2005) 'A Modular Design for the Clathrin- and Actin-Mediated Endocytosis Machinery', *Cell*, 123(2), pp. 305–320. Available at:

https://doi.org/10.1016/j.cell.2005.09.024.

Kaksonen, M., Toret, C.P. and Drubin, D.G. (2006) 'Harnessing actin dynamics for clathrin-mediated endocytosis', *Nature Reviews Molecular Cell Biology*, 7(6), pp. 404–414. Available at: https://doi.org/10.1038/nrm1940.

Kaplan, C. *et al.* (2022) 'Load adaptation by endocytic actin networks', *Molecular Biology of the Cell*, 33(6), p. ar50. Available at: https://doi.org/10.1091/mbc.E21-11-0589.

Karsenti, E. (2008) 'Self-organization in cell biology: a brief history', *Nature Reviews Molecular Cell Biology*, 9(3), pp. 255–262. Available at: https://doi.org/10.1038/nrm2357.

Keren, K. *et al.* (2008) 'Mechanism of shape determination in motile cells', *Nature*, 453(7194), pp. 475–480. Available at: https://doi.org/10.1038/nature06952.

Kirschner, M., Gerhart, J. and Mitchison, T. (2000) 'Molecular "Vitalism"', *Cell*, 100(1), pp. 79–88. Available at: https://doi.org/10.1016/S0092-8674(00)81685-2.

Kishimoto, T. *et al.* (2011) 'Determinants of endocytic membrane geometry, stability, and scission', *Proceedings of the National Academy of Sciences of the United States of America*, 108(44), pp. E979–E988. Available at: https://doi.org/10.1073/pnas.1113413108.

Kukulski, W. *et al.* (2012) 'Plasma Membrane Reshaping during Endocytosis Is Revealed by Time-Resolved Electron Tomography', *Cell*, 150(3), pp. 508–520. Available at: https://doi.org/10.1016/j.cell.2012.05.046.

Laakso, J.M. *et al.* (2010) 'Control of myosin-I force sensing by alternative splicing', *Proceedings of the National Academy of Sciences*, 107(2), pp. 698–702. Available at: https://doi.org/10.1073/pnas.0911426107.

Lacayo, C.I. *et al.* (2007) 'Emergence of Large-Scale Cell Morphology and Movement from Local Actin Filament Growth Dynamics', *PLOS Biology*, 5(9), p. e233. Available at: https://doi.org/10.1371/journal.pbio.0050233.

Lappalainen, P. and Drubin, D.G. (1997) 'Cofilin promotes rapid actin filament turnover in vivo', *Nature*, 388(6637), pp. 78–82. Available at: https://doi.org/10.1038/40418.

Lee, K. *et al.* (2010) 'Self-Assembly of Filopodia-Like Structures on Supported Lipid Bilayers', *Science*, 329(5997), pp. 1341–1345. Available at: https://doi.org/10.1126/science.1191710.

Lewellyn, E.B. *et al.* (2015) 'An Engineered Minimal WASP-Myosin Fusion Protein Reveals Essential Functions for Endocytosis', *Developmental Cell*, 35(3), pp. 281–294. Available at: https://doi.org/10.1016/j.devcel.2015.10.007.

Li, T.-D. *et al.* (2022) 'The molecular mechanism of load adaptation by branched actin networks', *eLife*. Edited by A. Michelot, 11, p. e73145. Available at: https://doi.org/10.7554/eLife.73145.

Liu, A.P. *et al.* (2008) 'Membrane-induced bundling of actin filaments', *Nature Physics*, 4(10), pp. 789–793. Available at: https://doi.org/10.1038/nphys1071.

Liu, A.P. and Fletcher, D.A. (2006) 'Actin Polymerization Serves as a Membrane Domain Switch in Model Lipid Bilayers', *Biophysical Journal*, 91(11), pp. 4064–4070. Available

at: https://doi.org/10.1529/biophysj.106.090852.

Liu, A.P. and Fletcher, D.A. (2009) 'Biology under construction: in vitro reconstitution of cellular function', *Nature Reviews Molecular Cell Biology*, 10(9), pp. 644–650. Available at: https://doi.org/10.1038/nrm2746.

Liu, J. *et al.* (2009) 'The Mechanochemistry of Endocytosis', *PLoS Biology*. Edited by F. Hughson, 7(9), p. e1000204. Available at: https://doi.org/10.1371/journal.pbio.1000204.

Loisel, T.P. *et al.* (1999) 'Reconstitution of actin-based motility of *Listeria* and *Shigella* using pure proteins', *Nature*, 401(6753), pp. 613–616. Available at: https://doi.org/10.1038/44183.

Longtine, M.S. *et al.* (1998) 'Additional modules for versatile and economical PCR-based gene deletion and modification in Saccharomyces cerevisiae', *Yeast*, 14(10), pp. 953–961. Available at: https://doi.org/10.1002/(SICI)1097-0061(199807)14:10<953::AID-YEA293>3.0.CO;2-U.

Lu, R., Drubin, D.G. and Sun, Y. (2016) 'Clathrin-mediated endocytosis in budding yeast at a glance', *J Cell Sci*, 129(8), pp. 1531–1536. Available at: https://doi.org/10.1242/jcs.182303.

Ma, R. and Berro, J. (2018) 'Structural organization and energy storage in crosslinked actin assemblies', *PLOS Computational Biology*, 14(5), p. e1006150. Available at: https://doi.org/10.1371/journal.pcbi.1006150.

Maly, I.V. and Borisy, G.G. (2001) 'Self-organization of a propulsive actin network as an evolutionary process', *Proceedings of the National Academy of Sciences*, 98(20), pp. 11324–11329. Available at: https://doi.org/10.1073/pnas.181338798.

Manenschijn, H.E. *et al.* (2019) 'Type-I myosins promote actin polymerization to drive membrane bending in endocytosis', *eLife*. Edited by C.G. Burd, A. Akhmanova, and C.G. Burd, 8, p. e44215. Available at: https://doi.org/10.7554/eLife.44215.

Martin, A.C., Welch, M.D. and Drubin, D.G. (2006) 'Arp2/3 ATP hydrolysis-catalysed branch dissociation is critical for endocytic force generation', *Nature Cell Biology*, 8(8), pp. 826–833. Available at: https://doi.org/10.1038/ncb1443.

Mayor, S. and Pagano, R.E. (2007) 'Pathways of clathrin-independent endocytosis', *Nature Reviews Molecular Cell Biology*, 8(8), pp. 603–612. Available at: https://doi.org/10.1038/nrm2216.

McCullough, B.R. *et al.* (2008) 'Cofilin Increases the Bending Flexibility of Actin Filaments: Implications for Severing and Cell Mechanics', *Journal of molecular biology*, 381(3), pp. 550–558. Available at: https://doi.org/10.1016/j.jmb.2008.05.055.

McIntosh, B.B. and Ostap, E.M. (2016) 'Myosin-I molecular motors at a glance', *J Cell Sci*, 129(14), pp. 2689–2695. Available at: https://doi.org/10.1242/jcs.186403.

Merrifield, C.J. and Kaksonen, M. (2014) 'Endocytic Accessory Factors and Regulation of Clathrin-Mediated Endocytosis', *Cold Spring Harbor Perspectives in Biology*, 6(11), p. a016733. Available at: https://doi.org/10.1101/cshperspect.a016733.

Messa, M. *et al.* (2014) 'Epsin deficiency impairs endocytosis by stalling the actin-dependent invagination of endocytic clathrin-coated pits', *eLife*. Edited by S.R. Pfeffer, 3, p. e03311. Available at: https://doi.org/10.7554/eLife.03311.

Miao, Y. *et al.* (2013) 'Cell-cycle regulation of formin-mediated actin cable assembly', *Proceedings of the National Academy of Sciences*, 110(47), pp. E4446–E4455. Available at: https://doi.org/10.1073/pnas.1314000110.

Michelot, A. *et al.* (2010) 'Reconstitution and Protein Composition Analysis of Endocytic Actin Patches', *Current Biology*, 20(21), pp. 1890–1899. Available at: https://doi.org/10.1016/j.cub.2010.10.016.

Michelot, A. and Drubin, D.G. (2011) 'Building Distinct Actin Filament Networks in a Common Cytoplasm', *Current Biology*, 21(14), pp. R560–R569. Available at: https://doi.org/10.1016/j.cub.2011.06.019.

Mogilner, A. and Edelstein-Keshet, L. (2002) 'Regulation of Actin Dynamics in Rapidly Moving Cells:A Quantitative Analysis', *Biophysical Journal*, 83(3), pp. 1237–1258. Available at: https://doi.org/10.1016/S0006-3495(02)73897-6.

Mogilner, A. and Oster, G. (1996) 'Cell motility driven by actin polymerization', *Biophysical Journal*, 71(6), pp. 3030–3045. Available at: https://doi.org/10.1016/S0006-3495(96)79496-1.

Mueller, J. *et al.* (2017) 'Load Adaptation of Lamellipodial Actin Networks', *Cell*, 171(1), pp. 188-200.e16. Available at: https://doi.org/10.1016/j.cell.2017.07.051.

Mulla, Y. *et al.* (2022) 'Weak catch bonds make strong networks', *Nature Materials*, pp. 1–5. Available at: https://doi.org/10.1038/s41563-022-01288-0.

Mullins, R.D., Stafford, W.F. and Pollard, T.D. (1997) 'Structure, Subunit Topology, and Actin-binding Activity of the Arp2/3 Complex from Acanthamoeba', *Journal of Cell Biology*, 136(2), pp. 331–343. Available at: https://doi.org/10.1083/jcb.136.2.331.

Mund, M. *et al.* (2018) 'Systematic Nanoscale Analysis of Endocytosis Links Efficient Vesicle Formation to Patterned Actin Nucleation', *Cell*, 0(0). Available at: https://doi.org/10.1016/j.cell.2018.06.032.

Nedelec, F. and Foethke, D. (2007) 'Collective Langevin dynamics of flexible cytoskeletal fibers', *New Journal of Physics*, 9(11), p. 427. Available at: https://doi.org/10.1088/1367-2630/9/11/427.

Newpher, T.M. and Lemmon, S.K. (2006) 'Clathrin is Important for Normal Actin Dynamics and Progression of Sla2p-Containing Patches During Endocytosis in Yeast', *Traffic*, 7(5), pp. 574–588. Available at: https://doi.org/10.1111/j.1600-0854.2006.00410.x.

Nicholson, D.J. (2019) 'Is the cell really a machine?', *Journal of Theoretical Biology*, 477, pp. 108–126. Available at: https://doi.org/10.1016/j.jtbi.2019.06.002.

Niu, Q. and Ybe, J.A. (2008) 'Crystal Structure at 2.8 Å of Huntingtin-Interacting Protein 1 (HIP1) Coiled-Coil Domain Reveals a Charged Surface Suitable for HIP1 Protein Interactor (HIPPI)', *Journal of Molecular Biology*, 375(5), pp. 1197–1205. Available at: https://doi.org/10.1016/j.jmb.2007.11.036.

Parekh, S.H. *et al.* (2005) 'Loading history determines the velocity of actin-network growth', *Nature Cell Biology*, 7(12), pp. 1219–1223. Available at: https://doi.org/10.1038/ncb1336.

Payne, G.S. and Schekman, R. (1985) 'A Test of Clathrin Function in Protein Secretion

and Cell Growth', *Science*, 230(4729), pp. 1009–1014. Available at: https://doi.org/10.1126/science.2865811.

Pearse, B.M. (1976) 'Clathrin: a unique protein associated with intracellular transfer of membrane by coated vesicles.', *Proceedings of the National Academy of Sciences*, 73(4), pp. 1255–1259. Available at: https://doi.org/10.1073/pnas.73.4.1255.

Pedersen, R.T. *et al.* (2023) 'An endocytic myosin essential for plasma membrane invagination powers motility against resistance'. bioRxiv, p. 2023.03.21.533689. Available at: https://doi.org/10.1101/2023.03.21.533689.

Pedersen, R.T.A. *et al.* (2020) 'Spatial regulation of clathrin-mediated endocytosis through position-dependent site maturation', *Journal of Cell Biology*, 219(11). Available at: https://doi.org/10.1083/jcb.202002160.

Pedersen, R.T.A. and Drubin, D.G. (2019) 'Type I myosins anchor actin assembly to the plasma membrane during clathrin-mediated endocytosis', *J Cell Biol*, p. jcb.201810005. Available at: https://doi.org/10.1083/jcb.201810005.

Peskin, C.S., Odell, G.M. and Oster, G.F. (1993) 'Cellular motions and thermal fluctuations: the Brownian ratchet', *Biophysical Journal*, 65(1), pp. 316–324. Available at: https://doi.org/10.1016/S0006-3495(93)81035-X.

Pfaendtner, J. *et al.* (2010) 'Structure and Dynamics of the Actin Filament', *Journal of Molecular Biology*, 396(2), pp. 252–263. Available at: https://doi.org/10.1016/j.jmb.2009.11.034.

Picco, A. *et al.* (2015) 'Visualizing the functional architecture of the endocytic machinery', *eLife*, 4, p. e04535. Available at: https://doi.org/10.7554/eLife.04535.

Picco, A. *et al.* (2018) 'The contributions of the actin machinery to endocytic membrane bending and vesicle formation', *Molecular Biology of the Cell*, 29(11), pp. 1346–1358. Available at: https://doi.org/10.1091/mbc.E17-11-0688.

Picco, A. and Kaksonen, M. (2017) 'Chapter 3 - Precise tracking of the dynamics of multiple proteins in endocytic events', in T. Lecuit (ed.) *Methods in Cell Biology*. Academic Press (Cell Polarity and Morphogenesis), pp. 51–68. Available at: https://doi.org/10.1016/bs.mcb.2016.11.002.

Planade, J. *et al.* (2019) 'Mechanical stiffness of reconstituted actin patches correlates tightly with endocytosis efficiency', *PLOS Biology*, 17(10), p. e3000500. Available at: https://doi.org/10.1371/journal.pbio.3000500.

Pollard, T.D. (1986) 'Rate constants for the reactions of ATP- and ADP-actin with the ends of actin filaments.', *Journal of Cell Biology*, 103(6), pp. 2747–2754. Available at: https://doi.org/10.1083/jcb.103.6.2747.

Pollard, T.D. (2010) 'A Guide to Simple and Informative Binding Assays', *Molecular Biology of the Cell*, 21(23), pp. 4061–4067. Available at: https://doi.org/10.1091/mbc.e10-08-0683.

Pollard, T.D. (2016a) 'Actin and Actin-Binding Proteins', *Cold Spring Harbor Perspectives in Biology*, 8(8), p. a018226. Available at: https://doi.org/10.1101/cshperspect.a018226.

Pollard, T.D. (2016b) 'Theory from the Oster Laboratory Leaps Ahead of Experiment in

Understanding Actin-Based Cellular Motility', *Biophysical Journal*, 111(8), pp. 1589–1592. Available at: https://doi.org/10.1016/j.bpj.2016.08.044.

Pollard, T.D., Blanchoin, L. and Mullins, R.D. (2001) 'Actin dynamics', *Journal of Cell Science*, 114(1), p. 3.

Pollard, T.D. and Borisy, G.G. (2003) 'Cellular Motility Driven by Assembly and Disassembly of Actin Filaments', *Cell*, 112(4), pp. 453–465. Available at: https://doi.org/10.1016/S0092-8674(03)00120-X.

Pucadyil, T.J. and Schmid, S.L. (2008) 'Real-Time Visualization of Dynamin-Catalyzed Membrane Fission and Vesicle Release', *Cell*, 135(7), pp. 1263–1275. Available at: https://doi.org/10.1016/j.cell.2008.11.020.

Rangamani, P. *et al.* (2011) 'Signaling Network Triggers and Membrane Physical Properties Control the Actin Cytoskeleton-Driven Isotropic Phase of Cell Spreading', *Biophysical Journal*, 100(4), pp. 845–857. Available at: https://doi.org/10.1016/j.bpj.2010.12.3732.

Rangamani, P., Mandadap, K.K. and Oster, G. (2014) 'Protein-Induced Membrane Curvature Alters Local Membrane Tension', *Biophysical Journal*, 107(3), pp. 751–762. Available at: https://doi.org/10.1016/j.bpj.2014.06.010.

Raz-Ben Aroush, D. *et al.* (2017) 'Actin Turnover in Lamellipodial Fragments', *Current Biology*, 27(19), pp. 2963-2973.e14. Available at: https://doi.org/10.1016/j.cub.2017.08.066.

Risca, V.I. *et al.* (2012) 'Actin filament curvature biases branching direction', *Proceedings of the National Academy of Sciences*, 109(8), pp. 2913–2918. Available at: https://doi.org/10.1073/pnas.1114292109.

Rodal, A.A. *et al.* (1999) 'Aip1p Interacts with Cofilin to Disassemble Actin Filaments', *The Journal of Cell Biology*, 145(6), pp. 1251–1264. Available at: https://doi.org/10.1083/jcb.145.6.1251.

Rodal, A.A. *et al.* (2003) 'Negative Regulation of Yeast WASp by Two SH3 Domain-Containing Proteins', *Current Biology*, 13(12), pp. 1000–1008. Available at: https://doi.org/10.1016/S0960-9822(03)00383-X.

Rohatgi, R., Ho, H.H. and Kirschner, M.W. (2000) 'Mechanism of N-Wasp Activation by Cdc42 and Phosphatidylinositol 4,5-Bisphosphate', *Journal of Cell Biology*, 150(6), pp. 1299–1310. Available at: https://doi.org/10.1083/jcb.150.6.1299.

Rottner, K. *et al.* (2017) 'Actin assembly mechanisms at a glance', *J Cell Sci*, 130(20), pp. 3427–3435. Available at: https://doi.org/10.1242/jcs.206433.

Rotty, J.D., Wu, C. and Bear, J.E. (2013) 'New insights into the regulation and cellular functions of the ARP2/3 complex', *Nature Reviews Molecular Cell Biology*, 14(1), pp. 7–12. Available at: https://doi.org/10.1038/nrm3492.

Sandvig, K., Kavaliauskiene, S. and Skotland, T. (2018) 'Clathrin-independent endocytosis: an increasing degree of complexity', *Histochemistry and Cell Biology*, 150(2), pp. 107–118. Available at: https://doi.org/10.1007/s00418-018-1678-5.

Schaus, T.E., Taylor, E.W. and Borisy, G.G. (2007) 'Self-organization of actin filament orientation in the dendritic-nucleation/array-treadmilling model', *Proceedings of the*

National Academy of Sciences, 104(17), pp. 7086–7091. Available at: https://doi.org/10.1073/pnas.0701943104.

Schroer, C.F.E. *et al.* (2020) 'Charge-dependent interactions of monomeric and filamentous actin with lipid bilayers', *Proceedings of the National Academy of Sciences*, 117(11), pp. 5861–5872. Available at: https://doi.org/10.1073/pnas.1914884117.

Scott, B.L. *et al.* (2018) 'Membrane bending occurs at all stages of clathrin-coat assembly and defines endocytic dynamics', *Nature Communications*, 9(1), p. 419. Available at: https://doi.org/10.1038/s41467-018-02818-8.

Senetar, M.A., Foster, S.J. and McCann, R.O. (2004) 'Intrasteric Inhibition Mediates the Interaction of the I/LWEQ Module Proteins Talin1, Talin2, Hip1, and Hip12 with Actin', *Biochemistry*, 43(49), pp. 15418–15428. Available at: https://doi.org/10.1021/bi0487239.

Shi, Z. *et al.* (2018) 'Cell Membranes Resist Flow', *Cell*, 175(7), pp. 1769-1779.e13. Available at: https://doi.org/10.1016/j.cell.2018.09.054.

Simunovic, M. *et al.* (2017) 'Friction Mediates Scission of Tubular Membranes Scaffolded by BAR Proteins', *Cell*, 170(1), pp. 172-184.e11. Available at: https://doi.org/10.1016/j.cell.2017.05.047.

Sirotkin, V. *et al.* (2010) 'Quantitative Analysis of the Mechanism of Endocytic Actin Patch Assembly and Disassembly in Fission Yeast', *Molecular Biology of the Cell*, 21(16), pp. 2894–2904. Available at: https://doi.org/10.1091/mbc.e10-02-0157.

Skau, C.T. *et al.* (2011) 'Actin Filament Bundling by Fimbrin Is Important for Endocytosis, Cytokinesis, and Polarization in Fission Yeast', *Journal of Biological Chemistry*, 286(30), pp. 26964–26977. Available at: https://doi.org/10.1074/jbc.M111.239004.

Skruzny, M. *et al.* (2012) 'Molecular basis for coupling the plasma membrane to the actin cytoskeleton during clathrin-mediated endocytosis', *Proceedings of the National Academy of Sciences*, 109(38), pp. E2533–E2542. Available at: https://doi.org/10.1073/pnas.1207011109.

Skruzny, M. *et al.* (2015) 'An Organized Co-assembly of Clathrin Adaptors Is Essential for Endocytosis', *Developmental Cell*, 33(2), pp. 150–162. Available at: https://doi.org/10.1016/j.devcel.2015.02.023.

Sochacki, K.A. *et al.* (2017) 'Endocytic proteins are partitioned at the edge of the clathrin lattice in mammalian cells', *Nature Cell Biology*, 19(4), pp. 352–361. Available at: https://doi.org/10.1038/ncb3498.

Sochacki, K.A. and Taraska, J.W. (2018) 'From Flat to Curved Clathrin: Controlling a Plastic Ratchet', *Trends in Cell Biology* [Preprint]. Available at: https://doi.org/10.1016/j.tcb.2018.12.002.

Soheil Aghamohammadzadeh and Ayscough, K.R. (2009) 'Differential requirements for actin during yeast and mammalian endocytosis', *Nature Cell Biology*, 11(8), pp. 1039–1042. Available at: https://doi.org/10.1038/ncb1918.

Soulard, A. *et al.* (2002) 'Saccharomyces cerevisiae Bzz1p Is Implicated with Type I Myosins in Actin Patch Polarization and Is Able To Recruit Actin-Polymerizing

Machinery In Vitro', *Molecular and Cellular Biology*, 22(22), pp. 7889–7906. Available at: https://doi.org/10.1128/MCB.22.22.7889-7906.2002.

Spang, A. and Schekman, R. (1998) 'Reconstitution of Retrograde Transport from the Golgi to the ER In Vitro', *Journal of Cell Biology*, 143(3), pp. 589–599. Available at: https://doi.org/10.1083/jcb.143.3.589.

Stachowiak, J.C. *et al.* (2012) 'Membrane bending by protein–protein crowding', *Nature Cell Biology*, 14(9), pp. 944–949. Available at: https://doi.org/10.1038/ncb2561.

Stevens, J.M., Galyov, E.E. and Stevens, M.P. (2006) 'Actin-dependent movement of bacterial pathogens', *Nature Reviews Microbiology*, 4(2), pp. 91–101. Available at: https://doi.org/10.1038/nrmicro1320.

Stoops, E.H. *et al.* (2023) 'Self-organizing actin networks drive sequential endocytic protein recruitment and vesicle release on synthetic lipid bilayers', *Proceedings of the National Academy of Sciences*, 120(22), p. e2302622120. Available at: https://doi.org/10.1073/pnas.2302622120.

St-Pierre, J. *et al.* (2009) 'Polo Kinase Regulates Mitotic Chromosome Condensation by Hyperactivation of Condensin DNA Supercoiling Activity', *Molecular Cell*, 34(4), pp. 416–426. Available at: https://doi.org/10.1016/j.molcel.2009.04.013.

Sun, Y. *et al.* (2017) 'Switch-like Arp2/3 activation upon WASP and WIP recruitment to an apparent threshold level by multivalent linker proteins in vivo', *eLife*, 6, p. e29140. Available at: https://doi.org/10.7554/eLife.29140.

Sun, Y. *et al.* (2019) 'Direct comparison of clathrin-mediated endocytosis in budding and fission yeast reveals conserved and evolvable features', *eLife*. Edited by S.R. Pfeffer and V. Sirotkin, 8, p. e50749. Available at: https://doi.org/10.7554/eLife.50749.

Sun, Y. and Drubin, D.G. (2012) 'The functions of anionic phospholipids during clathrin-mediated endocytosis site initiation and vesicle formation', *Journal of Cell Science*, 125(24), pp. 6157–6165. Available at: https://doi.org/10.1242/jcs.115741.

Sun, Y., Martin, A.C. and Drubin, D.G. (2006) 'Endocytic Internalization in Budding Yeast Requires Coordinated Actin Nucleation and Myosin Motor Activity', *Developmental Cell*, 11(1), pp. 33–46. Available at: https://doi.org/10.1016/j.devcel.2006.05.008.

Svitkina, T.M. and Borisy, G.G. (1999) 'Arp2/3 Complex and Actin Depolymerizing Factor/Cofilin in Dendritic Organization and Treadmilling of Actin Filament Array in Lamellipodia', *The Journal of Cell Biology*, 145(5), pp. 1009–1026. Available at: https://doi.org/10.1083/jcb.145.5.1009.

Taylor, M.J., Perrais, D. and Merrifield, C.J. (2011) 'A High Precision Survey of the Molecular Dynamics of Mammalian Clathrin-Mediated Endocytosis', *PLOS Biology*, 9(3), p. e1000604. Available at: https://doi.org/10.1371/journal.pbio.1000604.

Vinzenz, M. *et al.* (2012) 'Actin branching in the initiation and maintenance of lamellipodia', *Journal of Cell Science*, 125(11), pp. 2775–2785. Available at: https://doi.org/10.1242/jcs.107623.

Wagner, A.R. *et al.* (2013) 'Dip1 Defines a Class of Arp2/3 Complex Activators that Function without Preformed Actin Filaments', *Current Biology*, 23(20), pp. 1990–1998.

Available at: https://doi.org/10.1016/j.cub.2013.08.029.

Wang, X. *et al.* (2016) 'Actin-Regulator Feedback Interactions during Endocytosis', *Biophysical Journal*, 110(6), pp. 1430–1443. Available at: https://doi.org/10.1016/j.bpj.2016.02.018.

Wang, X. and Carlsson, A.E. (2017) 'A master equation approach to actin polymerization applied to endocytosis in yeast', *PLOS Computational Biology*, 13(12), p. e1005901. Available at: https://doi.org/10.1371/journal.pcbi.1005901.

Weber, T. *et al.* (1998) 'SNAREpins: Minimal Machinery for Membrane Fusion', *Cell*, 92(6), pp. 759–772. Available at: https://doi.org/10.1016/S0092-8674(00)81404-X.

Wedlich-Söldner, R. and Betz, T. (2018) 'Self-organization: the fundament of cell biology', *Phil. Trans. R. Soc. B*, 373(1747), p. 20170103. Available at: https://doi.org/10.1098/rstb.2017.0103.

Wu, J.-Q. and Pollard, T.D. (2005) 'Counting Cytokinesis Proteins Globally and Locally in Fission Yeast', *Science*, 310(5746), pp. 310–314. Available at: https://doi.org/10.1126/science.1113230.

Wu, M. *et al.* (2010) 'Coupling between clathrin-dependent endocytic budding and F-BAR-dependent tubulation in a cell-free system', *Nature Cell Biology*, 12(9), pp. 902–908. Available at: https://doi.org/10.1038/ncb2094.

Xiong, Y. *et al.* (2010) 'Mechanisms Controlling Cell Size and Shape during Isotropic Cell Spreading', *Biophysical Journal*, 98(10), pp. 2136–2146. Available at: https://doi.org/10.1016/j.bpj.2010.01.059.

Yamamoto, W. *et al.* (2018) 'Distinct roles for plasma membrane PtdIns(4)P and PtdIns(4,5)P2 during receptor-mediated endocytosis in yeast', *Journal of Cell Science*, 131(1), p. jcs207696. Available at: https://doi.org/10.1242/jcs.207696.

Yarar, D., Waterman-Storer, C.M. and Schmid, S.L. (2004) 'A Dynamic Actin Cytoskeleton Functions at Multiple Stages of Clathrin-mediated Endocytosis', *Molecular Biology of the Cell*, 16(2), pp. 964–975. Available at: https://doi.org/10.1091/mbc.e04-09-0774.

Yoshida, A. *et al.* (2018) 'Morphological changes of plasma membrane and protein assembly during clathrin-mediated endocytosis', *PLOS Biology*, 16(5), p. e2004786. Available at: https://doi.org/10.1371/journal.pbio.2004786.

Youn, J.-Y. *et al.* (2010) 'Dissecting BAR Domain Function in the Yeast Amphiphysins Rvs161 and Rvs167 during Endocytosis', *Molecular Biology of the Cell*, 21(17), pp. 3054–3069. Available at: https://doi.org/10.1091/mbc.e10-03-0181.

Zhao, H. *et al.* (2013) 'Membrane-Sculpting BAR Domains Generate Stable Lipid Microdomains', *Cell Reports*, 4(6), pp. 1213–1223. Available at: https://doi.org/10.1016/j.celrep.2013.08.024.